WHOI-97-17

Woods Hole Oceanographic Institution

Biweekly maps of wind stress for the North Pacific from the ERS-1 scatterometer 1992 – 1995

by

Michael J. Caruso and Kathryn A. Kelly

November 1997

Technical Report

Funding was provided by the Office of Naval Research through contracts No. N00014-92-J-1486 and N00014-92-J-1656 and by the National Aeronautics and Space Administration under Contract No. 957652.

WHOI-97-17

Biweekly maps of wind stress for the North Pacific from the ERS-1 scatterometer 1992 – 1995

by

Michael J. Caruso and Kathryn A. Kelly

Woods Hole Oceanographic Institution
Woods Hole, Massachusetts 02543

November 1997

Technical Report

Funding was provided by the Office of Naval Research through contracts No. N00014-92-J-1486
and N00014-92-J-1656 and by the National Aeronautics and Space Administration under Contract No. 957652.

Approved for public release; distribution unlimited.

Approved for Distribution:

Philip L. Richardson

Philip L. Richardson, Chair

Department of Physical Oceanography

Contents

List of Tables

1 Introduction

The European Remote-sensing Satellite (ERS-1) was launched in July 1991 and contained several instruments for observing the Earth's ocean including a wind scatterometer. The scatterometer measurements were processed by the European Space Agency (ESA) and the Jet Propulsion Laboratory (JPL). JPL reprocessed (Freilich and Dunbar, 1992) the ERS-1 backscatter measurements to produced a "value added" data set that contained the ESA wind vector as well as a set of up to four ambiguities. These ambiguities were further processed using a maximum-likelihood estimation (MLE) and a median filter to produce a "selected vector."

This report describes a technique developed to produce time-averaged wind field estimates with their expected errors using only scatterometer wind vectors. The processing described in this report involved extracting regions of interest from the data tapes, checking the quality and creating the wind field estimate . This analysis also includes the derivation of biweekly average wind vectors over the North Pacific Ocean at a resolution of $0.5° \times 0.5°$. This was done with an optimal average algorithm temporally and an over-determined biharmonic spline spatially. There have been other attempts at creating gridded wind files from ERS-1 winds, e.g., kriging techniques (Bentamy *et al.*, 1996) and successive corrections schemes (Tang and Liu, 1996).

There are several inherent problems with the ERS-1 scatterometer. Since this is a multidisciplinary mission, the satellite is flown in different orbits optimized for each phase of the mission. The scatterometer also shares several sub-systems with the Synthetic Aperture Radar (SAR) and cannot be operated while the SAR is in operation. The scatterometer is also a single-sided instrument and only measures backscatter along the right side of the satellite. The processing described here generates biweekly wind maps during the two year analysis period regardless of the satellite orbit or missing data.

Section 2 describes some of the ERS-1 satellite specifications, including orbital parameters, the scatterometer instrument precision and the "value added" data record provided by JPL. The analysis technique is described in detail in section 3 and data validation is discussed in section 4. Some results are discussed in section 5 and a summary of the results is given in section 6. Appendix A contains annual mean winds for 1992 through 1995. Appendix B contains seasonally averaged winds for winter, spring, summer and fall. Appendix C contains sample plots of the biweekly ERS-1 derived wind components, a complete series of monthly mean wind components in the North Pacific and monthly wind vector plots for the California Current region.

2 Satellite and sensor specifications

2.1 Scatterometer

The scatterometer is part of the Active Microwave Instrument (AMI) aboard ERS-1. The AMI has two separate radars, a SAR and a wind scatterometer (WNS). The SAR operates in "image mode" or "wave mode" while the WNS operates in "wind mode." Due to shared subsystems

designed to save mass and cost, the WNS cannot operate while the SAR is in "image mode." The WNS can operate while the SAR is in "wave mode"; this is known as the "wind/wave mode." Operation of the AMI in image or wave mode is not covered in this report.

The scatterometer is a C-Band (5.3GHz) radar with 3 separate antennas capable of measuring wind speed (4-24 ms^{-1}) and direction (0-360° ±20°) along a single swath to the right side of of the satellite[1]. The cell spacing is 25 km with a swath width of 500 km and a stand-off of 200 km from nadir (Vass and Battrick, 1992).

2.2 JPL Value-Added Data Record

JPL receives the scatterometer backscatter coefficients from ESA and recomputes the full set of wind vector ambiguities. These are combined with the single ESA computed wind vector to make the JPL value-added product. Each record contains information on all 19 cells between the inner and outer scatterometer swath. Table 1 summarizes the data record (from information supplied with JPL ERS-1 value-added product). The time variable has one value giving the mean time of the record. The latitude and longitude variables are each 19 element arrays specifying the location of the Wind Vector Cell (WVC). The ERS-1 speed and direction variables are also 19 element arrays and give the wind speed and direction determined by ESA. The ambiguities variable gives the number of ambiguities found by JPL in the least significant byte (LSB) and their selected ambiguity in the most significant byte (MSB). The MLE speed and direction variables are 4 by 19 element arrays containing all of the ambiguities found using the MLE value for each WVC. Note that directions are given in meteorological convention (where 0° indicates that the wind is flowing from the north) and ambiguity removal is only performed between 60° S and 60° N.

[1]Note that the NASA Scatterometer (NSCAT), launched in September 1996 produced 2 swaths and a more complete sampling pattern.

Variable	Contents	Size/Bytes	Units
Time	mean time of record	1/4	I*4 seconds from 1/1/87
Latitude	Wind vector latitude	19/38	I*2 0.01°
Longitude	Wind vector longitude	19/38	I*2 0.01°
ERS-1 Speed	ESA selected ambiguity	19/38	I*2 0.01 ms^{-1}
ERS-1 Direction	ESA selected ambiguity	19/38	I*2 0.01° [-180°, 180°]
Flag (See table 2)	Confidence flag	1/2	L*2
Ambiguities	Number of ambiguities (LSB) from MLE and JPL selected ambiguity (MSB)	19/38	I*2 [1–4]
MLE Speed	MLE wind speeds	(4,19)/152	I*2 ms^{-1}
MLE Direction	MLE ordered wind directions	(4,19)/152	I*2 0.01° [-180°, 180°]

Table 1: Wind Vector Cell (WVC) Record

Bits	Description [2]	Values
1	Summary PC factor	0 - Full processing
		1 - PCD bits set
2	Fore-beam flag	0 - Used
		1 - Not used
3	Mid-beam flag	0 - Used
		1 - Not used
4	Aft-beam flag	0 - Used
		1 - Not used
5	Fore-beam arcing flag	0 - No arc
		1 - Arcing
6	Mid-beam arcing flag	0 - No arc
		1 - Arcing
7	Aft-beam arcing flag	0 - No arc
		1 - Arcing
8	Limit of Kp value	0 - All beams < threshold
9	Land-Sea	0 - Sea
		1 - Land
10	Rank-1 solution	0 - Ambiguity removed
		1 Rank-1 solution given
11–13	Ambiguity removal method	0 - Auto ambiguity removal
		1 - Met. tables used after amb. removal
		1 - Meteorological data only
14	Frame checksum	0 - Checksum correct
15–16	Spare	

Table 2: Wind Vector Cell confidence flag

2.3 Orbit

The ERS-1 satellite was designed with multiple orbit capability. There are two 3-day repeat orbits, one 35-day repeat orbit and one 176-day repeat orbit that trade temporal resolution for spatial resolution. After the launch, the satellite was initially placed into a 3-day commissioning orbit and was used primarily for testing. It was then moved into a 3-day ice orbit for three months (Figure 1), followed by a 35-day orbit (Figure 2) for 21 months and then returned to the 3-day ice orbit for three months. The satellite was then moved into a 176-day geodetic orbit (not shown). The 3-day repeat orbit has good temporal resolution, but leaves coverage gaps at the mid- and lower latitudes. The 35-day and 176-day repeat orbits provide high resolution coverage, but leave large temporal gaps in the data. Table 3 lists the key orbital parameters for each orbit.

[2]From User's Manual included with JPL ERS-1 VALUE-ADDED product.

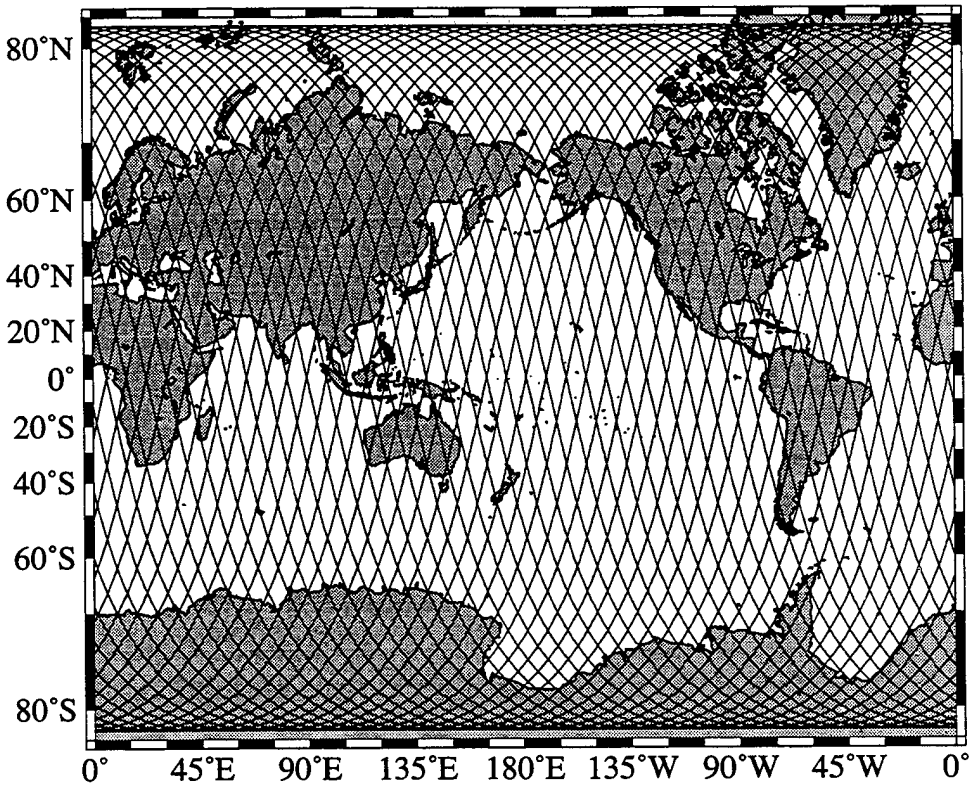

Figure 1: The ERS-1 3-day repeat orbit ground track used during the ice phase of the mission (January–March 1992 and January–March 1994).

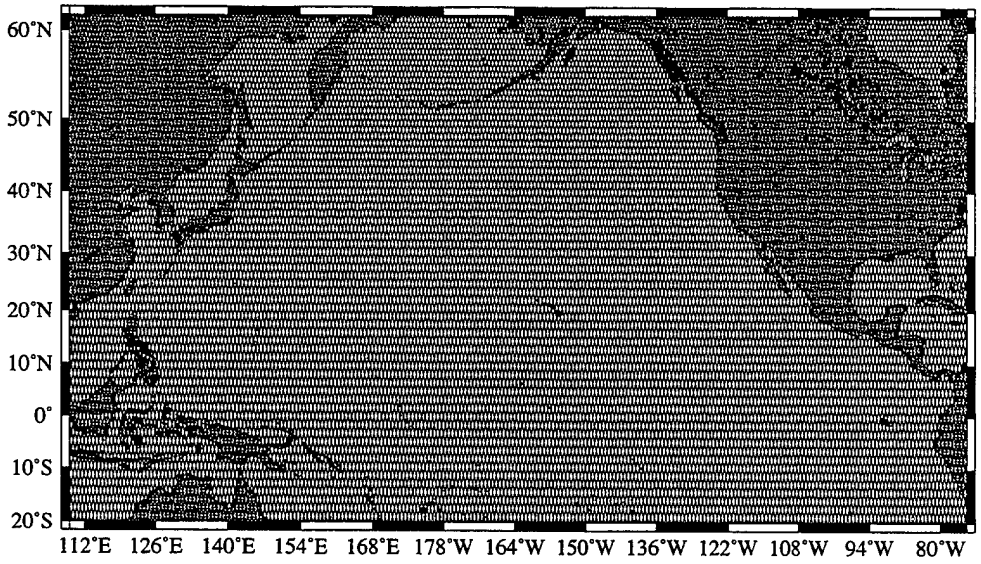

Figure 2: The ERS-1 35-day repeat orbit ground track used during the multidisciplinary phase (April 1992–December 1993) of the mission.

Description	Inc.	Alt.	Asc Node	Orbits	Period
Commissioning 3 days	98.516°	785 km	24.36°E	43	6020.8191 s
Ice 3 days	98.516°	785 km	128.2°W	43	6020.8191 s
Multidisciplinary 35 days	98.543°	782 km	20.96°E	501	6028.8482 s
Geodetic 176 days	98.529	780 km		2527	

Table 3: Orbit parameters

The ERS-1 satellite is maneuvered periodically to maintain or change its orbit. The orbit corrections are usually short and produce small gaps in coverage. The orbit changes generate much longer gaps in coverage and are summarized in Table 4.

Phase	Repeat (days)	Start	End
Commissioning	3	July, 25, 1991	December 10, 1991
Ice	3	December 28, 1991	March 30, 1992
Roll-Tilt	35	April 2, 1992	April 14, 1992
Multidisciplinary	35	April 14, 1992	December 31, 1993
Ice	3	January 1, 1994	March 31, 1994
Geodetic	176	April 1, 1994	Mission end

Table 4: Orbit maneuvers[3]

2.3.1 Numbering

The data records received from JPL are separated into individual segments for easier processing. Each segment is referred to by the revolution number specified in the User's Manual on the data tape. A revolution is defined as a segment of the orbit beginning at the southernmost position of the satellite, through the northernmost position and back to the next southernmost position. These numbers are incremented for each new revolution beginning from the satellite launch.

2.3.2 Coverage

The locations of the measured backscatter for a complete 3-day cycle during the ice phase is shown in Figure 3. The measured backscatter is used to produce a wind vector at each of these locations. In the JPL documentation and in this report, these locations will be referred to as Wind Vector Cells (WVCs). Unfortunately, due to instrument and environmental problems, a valid wind vector is not available for all WVCs. The WVCs with a "selected vector" from JPL from a 3-day period during the ice phase in March 1992 (Figure 4) show relatively good coverage. The WVCs with a valid wind vector supplied by ESA during the same 3-day period (Figure 5) are quite sparse. This is primarily because JPL will often provide a vector when the wind speeds are less than 4 ms^{-1}, while ESA does not. These figures also show the coverage problems encountered during the 3-day orbit phase. Figure 3 shows the characteristic missing data diamonds at approximately 38° N and 123° E, 132° E, 140° E, 148° E. These diamonds are stationary gaps in the 3-day orbit. The tops of other diamonds can be seen at 20° N. The combination of data loss during processing and missing data due to coverage can produce large spatial gaps in the data.

[3]From ERS-1 News produced by the ERS-1 Help Desk.

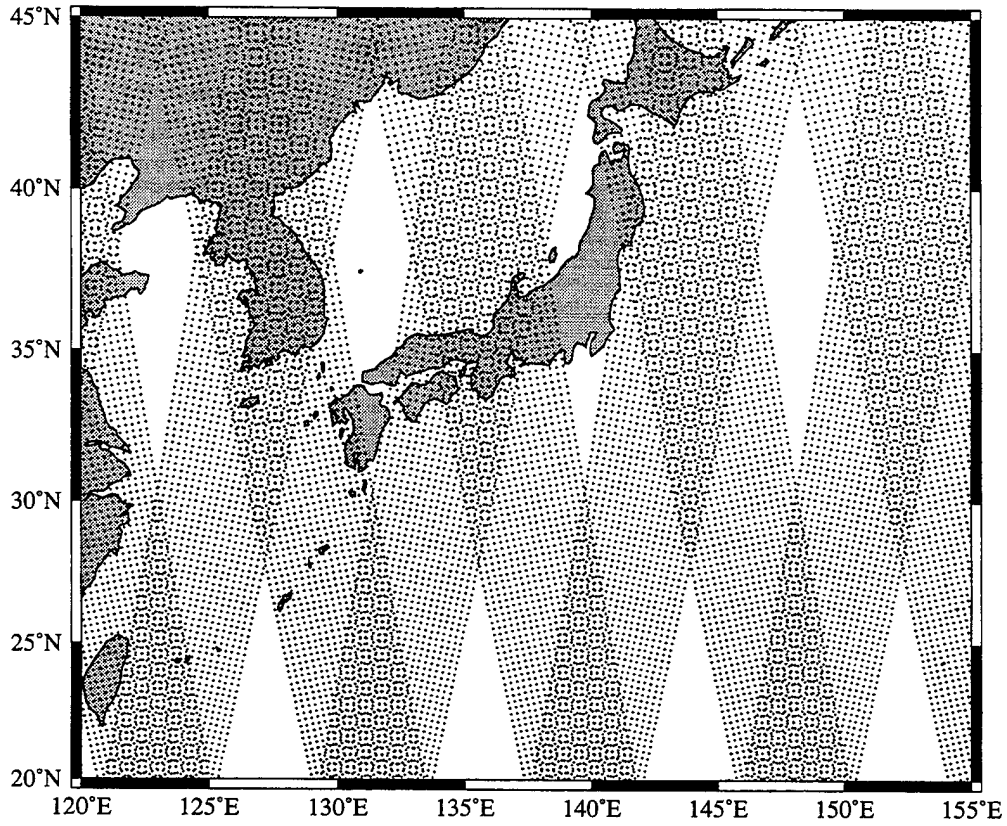

Figure 3: The locations of measured backscatter for one 3-day cycle.

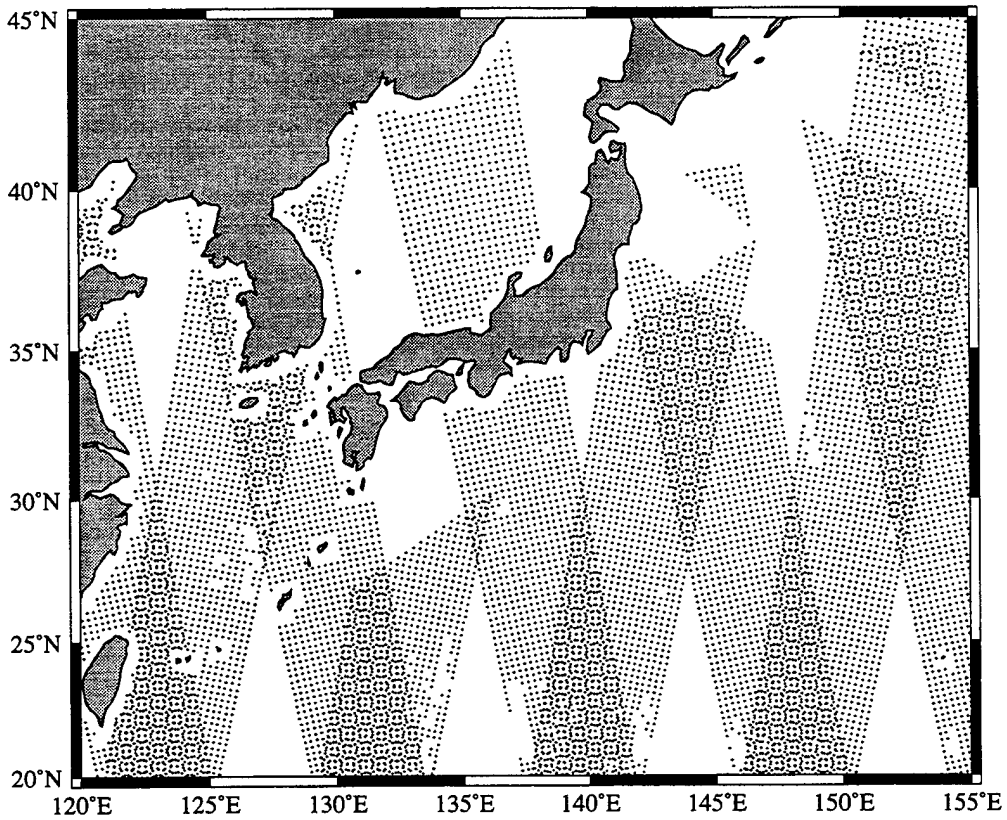

Figure 4: The ground coverage for one 3-day cycle of JPL selected vectors from March 1, 1992 to March 4, 1992.

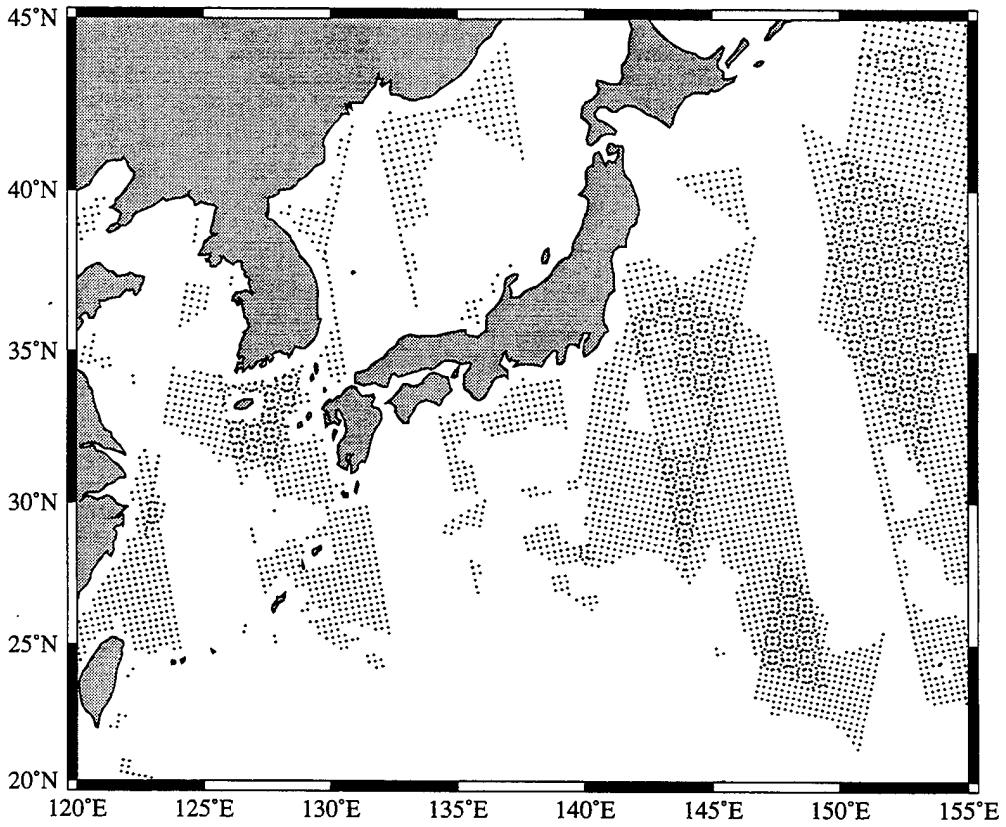

Figure 5: The ground coverage for one 3-day cycle of ESA selected vectors from March 1, 1992 to March 4, 1992.

Figure 6 shows coverage during the first week of September. The satellite is in the 35-day repeat orbit during this time. This figure shows that there are still missing data triangles, but they are not stationary as they are during the 3-day repeat orbit. This figure shows that successive tracks begin to fill in the missing data and some areas (40° N, 150° E) may have up to four separate measurements.

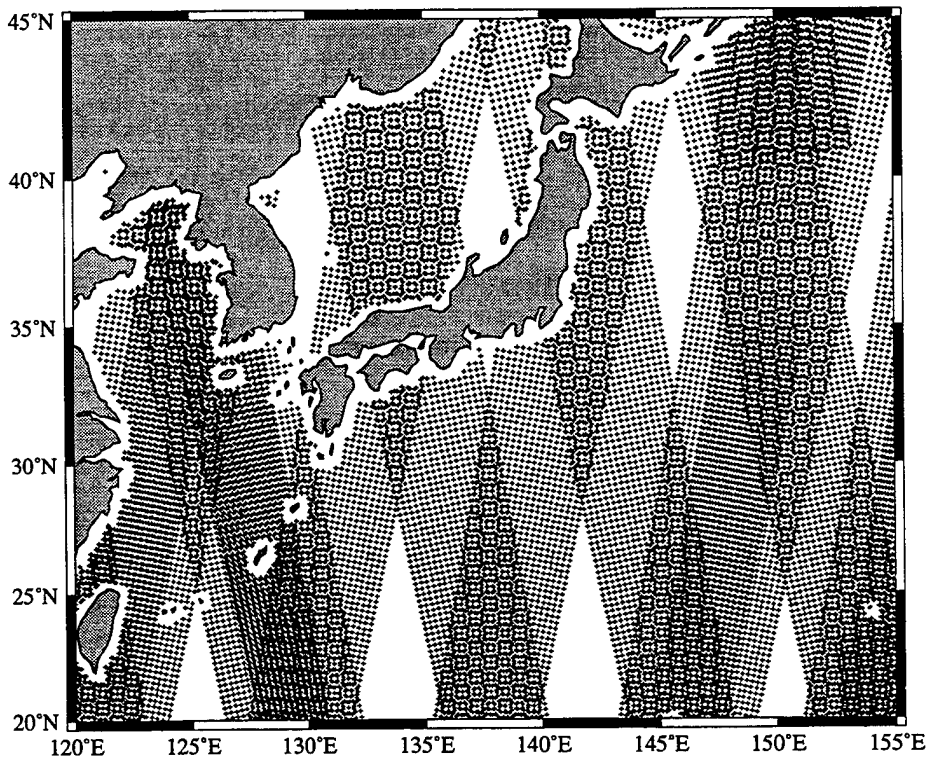

Figure 6: The ground coverage for one fifth of the 35-day cycle, September 1–7, 1993.

3 Scatterometer analysis

The analysis of the scatterometer winds was performed in several steps. Each step is described in detail in this section.

1. Extract data within the region of interest
2. Clean up data records
3. Bin data to 0.5°, 12 hour resolution
4. Perform suboptimal interpolation
5. Spatially interpolate using biharmonic spline
6. Calculate wind stress and curl

3.1 Extraction

Data records from 1992 were extracted for the region 20° S–62° N, 109° E–285° E. No data quality checks are done at this point of the process. Due to the space requirements for the interpolation of this data set, the North Pacific was split into 25 smaller regions (Figure 7). Each region was analyzed separately in steps 1–4 for the meridional and zonal wind components. Since this did not involve any spatial information, the size of each region was chosen to maximize computer resources. The entire North Pacific was reconstructed for steps 5 and 6.

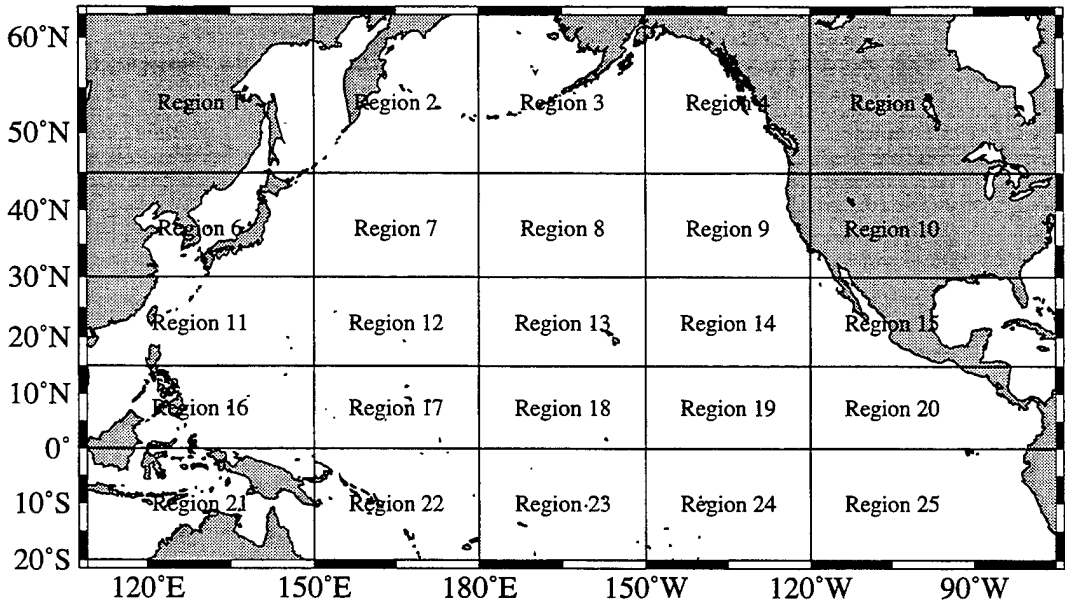

Figure 7: The segmentation of the North Pacific for regional analysis. The data was separated into 25 regions to facilitate handling the large amount of data.

3.2 Clean up

After the data for the desired region have been extracted from the ERS-1 data tapes, any obviously bad data records are flagged. All values greater than 40 ms^{-1} were replaced with a flag value of -99.0. Wind speeds less than 1 ms^{-1} were also replaced with this flag value. Values between 1 ms^{-1} and the ESA cutoff of 4 ms^{-1} were retained.

3.3 Binning

The data was gridded to $0.5° \times 0.5°$ bins in 12 hour intervals. If more than one datum fell in a bin, the mean of all the data was used as the binned value.

3.4 Suboptimal interpolation

The estimate of the mean value for each velocity component was obtained using a suboptimal estimation technique [Chelton and Schlax, 1991]. The estimate is calculated at each $0.5° \times 0.5°$ bin for each averaging period. This method provides a better estimate than simple composite averages and requires specification of the time-lagged covariance function. We used an e-folding time of 3.5 days and a signal to noise ratio of 0.06. In addition, this technique also produces an estimate for the error for each point. An analysis of the average estimated error for 3 months of data indicated that reasonable errors could be obtained with averaging periods of 7–30 days (Figure 8). For this study, we chose 14 days as the compromise between temporal resolution and estimated errors. The output files were numbered beginning with January 1, 1992 and the dates for each interval are shown in Table 5.

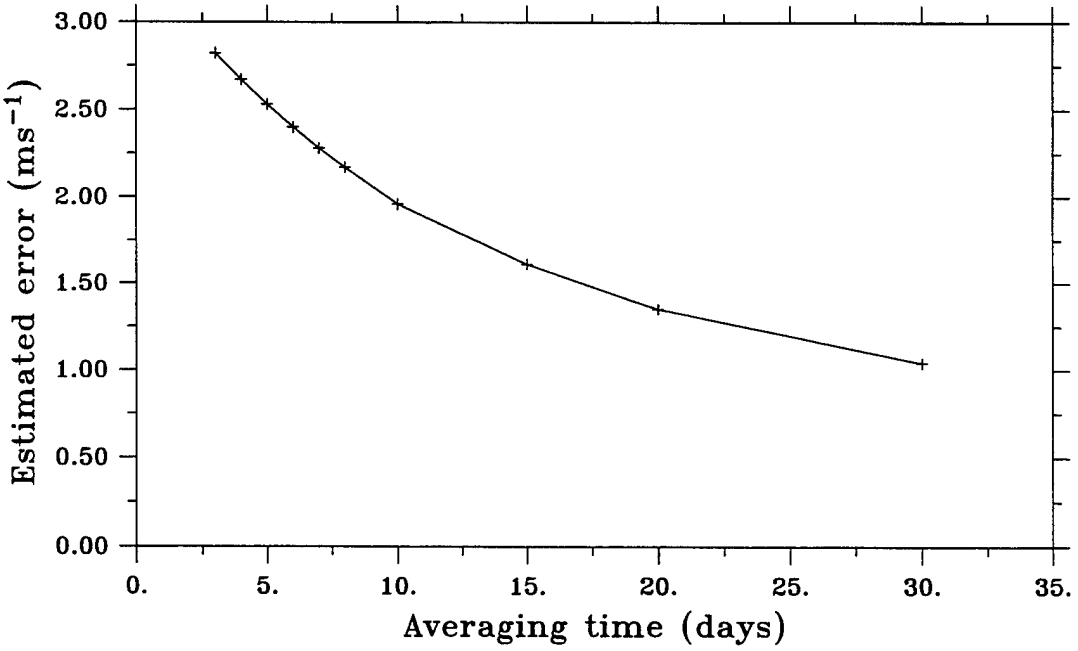

Figure 8: The average estimated errors for different averaging periods.

Biweek Number Of year/Total	Start Date	End Date	Season
00/00	Jan 1	Jan 14	winter
01/01	Jan 15	Jan 28	
02/02	Jan 29	Feb 11	
03/03	Feb 12	Feb 25	
04/04	Feb 26	Mar 10	
05/05	Mar 11	Mar 24	
06/06	Mar 25	Apr 7	
07/07	Apr 8	Apr 21	spring
08/08	Apr 22	May 5	
09/09	May 6	May 19	
10/10	May 20	Jun 2	
11/11	Jun 3	Jun 16	
12/12	Jun 17	Jun 30	
13/13	Jul 1	Jul 14	summer
14/14	Jul 15	Jul 28	
15/15	Jul 29	Aug 11	
16/16	Aug 12	Aug 25	
17/17	Aug 26	Sep 8	
18/18	Sep 9	Sep 22	
19/19	Sep 23	Oct 6	
20/20	Oct 7	Oct 20	fall
21/21	Oct 21	Nov 3	
22/22	Nov 4	Nov 17	
23/23	Nov 18	Dec 1	
24/24	Dec 2	Dec 15	
25/25	Dec 16	Dec 29	
00/26	Dec 30	Jan 12, 1993	winter
01/27	Jan 13	Jan 26	
02/28	Jan 27	Feb 9	
03/29	Feb 10	Feb 23	
04/30	Feb 24	Mar 9	
05/31	Mar 10	Mar 23	
06/32	Mar 24	Apr 6	
07/33	Apr 7	Apr 20	spring
08/34	Apr 21	May 4	
09/35	May 5	May 18	

continued on next page

continued from previous page

Biweek Number Of year/Total	Start Date	End Date	Season
10/36	May 19	Jun 1	
11/37	Jun 2	Jun 15	
12/38	Jun 16	Jun 29	
13/39	Jun 30	Jul 13	summer
14/40	Jul 14	Jul 27	
15/41	Jul 28	Aug 10	
16/42	Aug 11	Aug 24	
17/43	Aug 25	Sep 7	
18/44	Sep 8	Sep 21	
19/45	Sep 22	Oct 5	fall
20/46	Oct 6	Oct 19	
21/47	Oct 20	Nov 2	
22/48	Nov 3	Nov 16	
23/49	Nov 17	Nov 30	
24/50	Dec 1	Dec 14	
25/51	Dec 15	Dec 28	
00/52	Dec 29	Jan 11, 1994	winter
01/53	Jan 12	Jan 25	
02/54	Jan 26	Feb 8	
03/55	Feb 9	Feb 22	
04/56	Feb 23	Mar 8	
05/57	Mar 9	Mar 22	
06/58	Mar 23	Apr 5	
07/59	Apr 6	Apr 19	spring
08/60	Apr 20	May 3	
09/61	May 4	May 17	
10/62	May 18	May 31	
11/63	Jun 1	Jun 14	
12/64	Jun 15	Jun 28	
13/65	Jun 29	Jul 12	summer
14/66	Jul 13	Jul 26	
15/67	Jul 27	Aug 9	
16/68	Aug 10	Aug 23	
17/69	Aug 24	Sep 6	
18/70	Sep 7	Sep 20	

continued on next page

continued from previous page

Biweek Number Of year/Total	Start Date	End Date	Season
19/71	Sep 21	Oct 4	fall
20/72	Oct 5	Oct 18	
21/73	Oct 19	Nov 1	
22/74	Nov 2	Nov 15	
23/75	Nov 16	Nov 29	
24/76	Nov 30	Dec 13	
25/77	Dec 14	Dec 27	
00/78	Dec 28	Jan 10, 1995	winter
01/79	Jan 11	Jan 24	
02/80	Jan 25	Feb 7	
03/81	Feb 8	Feb 21	
04/82	Feb 22	Mar 7	
05/83	Mar 8	Mar 21	
06/84	Mar 22	Apr 4	
07/85	Apr 5	Apr 18	spring
08/86	Apr 19	May 2	
09/87	May 3	May 16	
10/88	May 17	May 30	
11/89	May 31	Jun 13	
12/90	Jun 14	Jun 27	
13/91	Jun 28	Jul 11	summer
14/92	Jul 12	Jul 25	
15/93	Jul 26	Aug 8	
16/94	Aug 9	Aug 22	
17/95	Aug 23	Sep 5	
18/96	Sep 6	Sep 19	
19/97	Sep 20	Oct 3	fall
20/98	Oct 4	Oct 17	
21/99	Oct 18	Oct 31	
22/100	Nov 1	Nov 14	
23/101	Nov 15	Nov 28	
24/102	Nov 29	Dec 12	
25/103	Dec 13	Dec 26	

Table 5: Periods of biweekly averages.

3.5 Biharmonic spline

After the sub-optimal interpolation, the biweekly averages for each of the 25 regions are concatenated together and are splined spatially using a modified biharmonic spline [Kelly and Caruso, 1990]. This spline does not change the winds where the estimated errors are low, only at locations where the estimated errors are high. It also minimizes divergence in regions of large errors to produce realistic wind fields.

3.6 Wind stress (τ) and wind stress curl ($\nabla \times \tau$)

Wind stress and wind stress curl are often more important to ocean dynamics than wind fields. Additionally, the curl and divergence of a wind field can help in the analysis of the wind fields. An abnormal value for either of these can indicate errors in the wind fields.

The general equation for wind stress, is a non-linear function of the wind:

$$\overline{\tau} = \rho c_D |\mathbf{U}| \mathbf{U} \tag{1}$$

To preserve the non-linearity of the wind stress in a biweekly wind vector average, the mean stress was calculated using the formula [Wright and Thompson, 1982]:

$$\overline{\tau} = \rho c_D(a) a \mathbf{U_0} \tag{2}$$

where

$$a = \left[U_0^2 + (2\sigma_u)^2\right]^{1/2} \tag{3}$$

Here, the coefficient of drag c_D is calculated using using the drag coefficient estimates from Large and Pond (1981). Although this technique is intended for averaging periods of greater that one month, a biweekly estimate would produce a low estimate due to the variability in the North Pacific. Since we did not have actual σ_u, we used the scatterometer sample standard deviation to calculate the biweekly wind stress estimates.

4 Data Validation

It is difficult at best to effectively compare surface wind fields to determine the true or correct wind. Comparison with buoys can be misleading due to differences in averaging periods, location, anemometer height or wave-shielding. Many surface wind products incorporate any available in-situ wind measurements. A more independent comparison may be done using the winds as input to a numerical ocean model (Cardone *et al.*, 1995). Cardone used a surface wave model to test 6 different wind fields and surmised that the location and amplitudes of cyclones and fronts are the most important characteristics of a wind field.

4.1 Ambiguity removal errors

An inherent problem with winds obtained from scatterometers is that the algorithms used may produce up to 4 ambiguities. Although there are many techniques such as the MLE algorithm used by JPL (§ 2.2), these algorithms still sometimes produce inconsistent winds. The MLE technique has a problem where it will occasionally have "patches" within a swath that are inconsistent. Figure 9 shows a sample of this problem between 30°–35° N, 125°–120° W. This figure also shows a storm centered about 40° N, 126° W. Visually, the problem is apparent, but it is difficult to automate the detection of these inconsistencies. Therefore, these "patches" were not removed for this analysis.

4.2 ECMWF model comparisons

A qualitative comparison of European Centre for Medium-Range Weather Forecasts (ECMWF) surface wind fields with the ERS-1 derived wind fields shows good large scale agreement. Some fields are very similar (Figure 10), while other fields have significant differences (e.g., 40°–45° N, 150°–135° W, Figure 11). Although, the two fields in Figure 10 look very similar, they display one of the major differences between most GCM wind fields: the centers of circulation are often displaced by several degrees. Most fields have many structures in common, however the ERS-1 winds tend to have more small scale structure (Figures 10–13). Figure 12 shows ERS-1 winds blowing in a more southeasterly direction offshore of California (130°–132° W) and more alongshore (122°–124° W) than the ECMWF winds. Although the bifurcation point may be about the same (40° N), the ERS-1 winds north of the bifurcation are blowing toward the northeast whereas the ECMWF winds blow toward the east. In the western Pacific (Figure 13), there are similar large-scale features. The ECMWF winds tend to be more uniform across the region than the ERS-1 winds which tend to show more spatial variability.

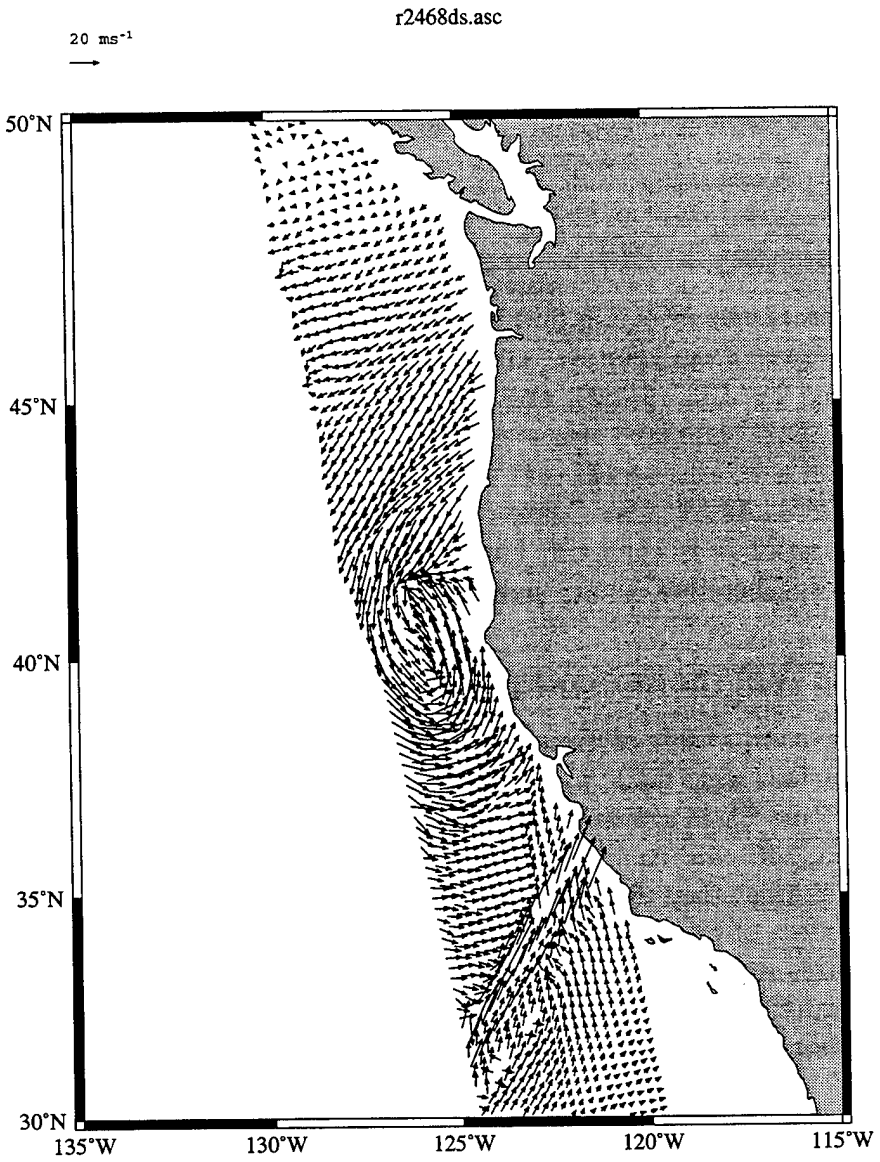

Figure 9: JPL selected ERS-1 wind vectors for a single swath from rev 2468. This figure shows a strong cyclone along with a near by region of incorrect vectors.

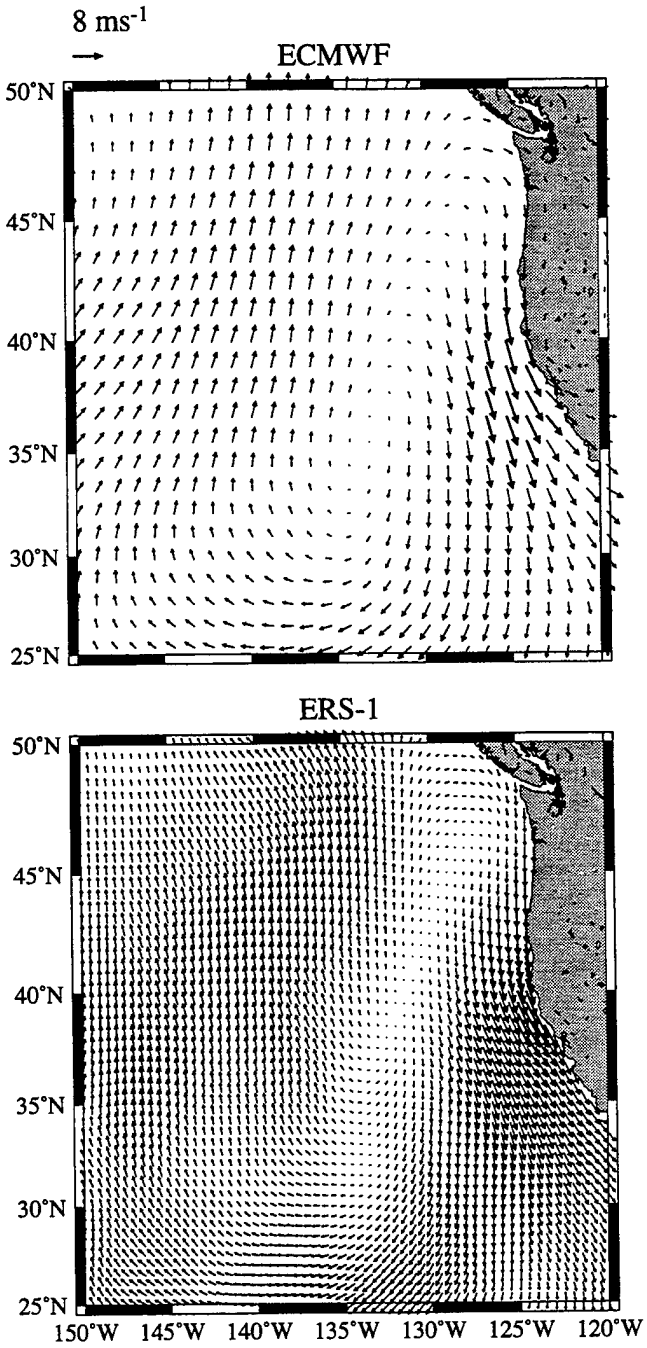

Figure 10: Comparison of ECWMF winds (top) and ERS-1 winds (bottom) for biweek 10: May 20–Jun 2, 1992.

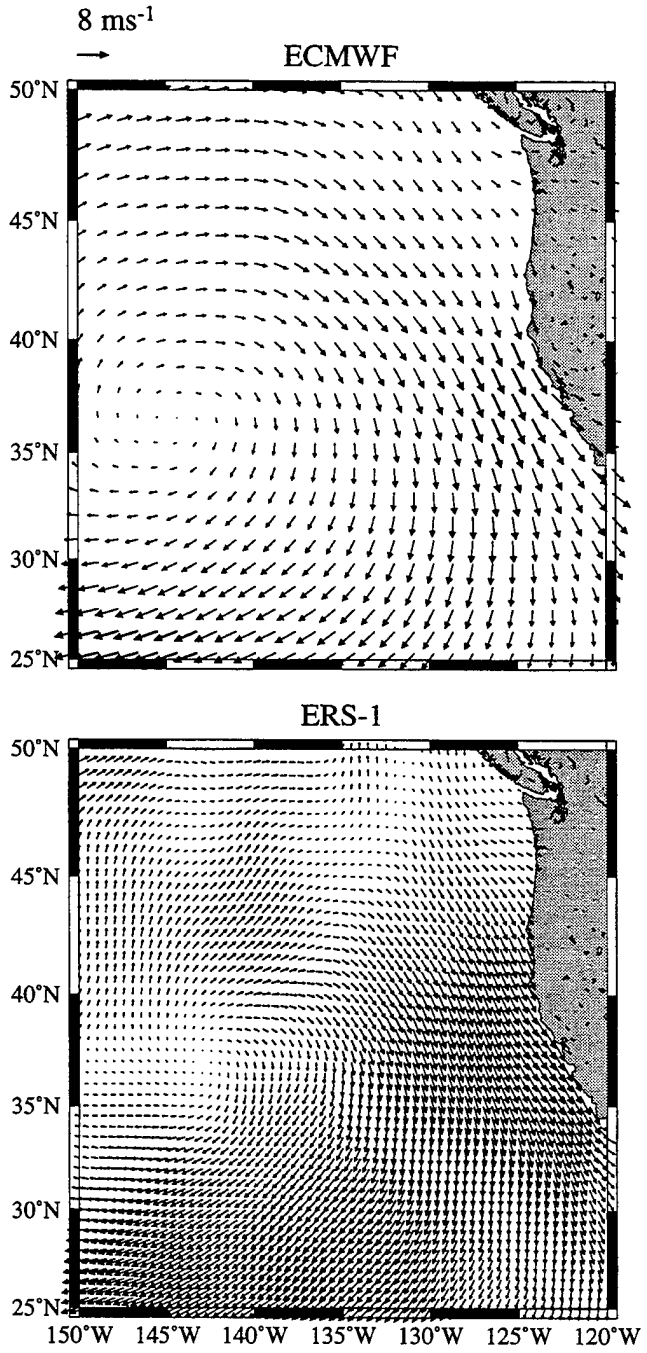

Figure 11: Comparison of ECWMF winds (top) and ERS-1 winds (bottom) for biweek 11: Jun 3–Jun 16, 1992.

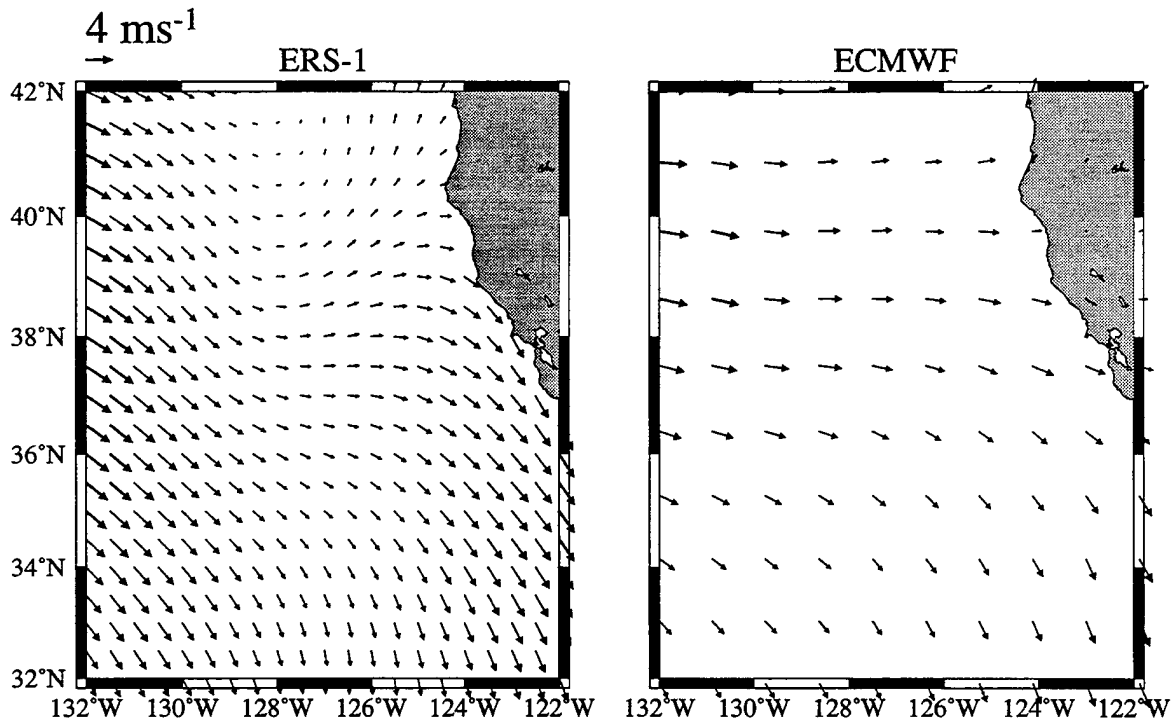

Figure 12: Comparison of ECWMF winds (top) and ERS-1 winds (bottom) for biweek 21: Oct 7–Oct 20, 1992.

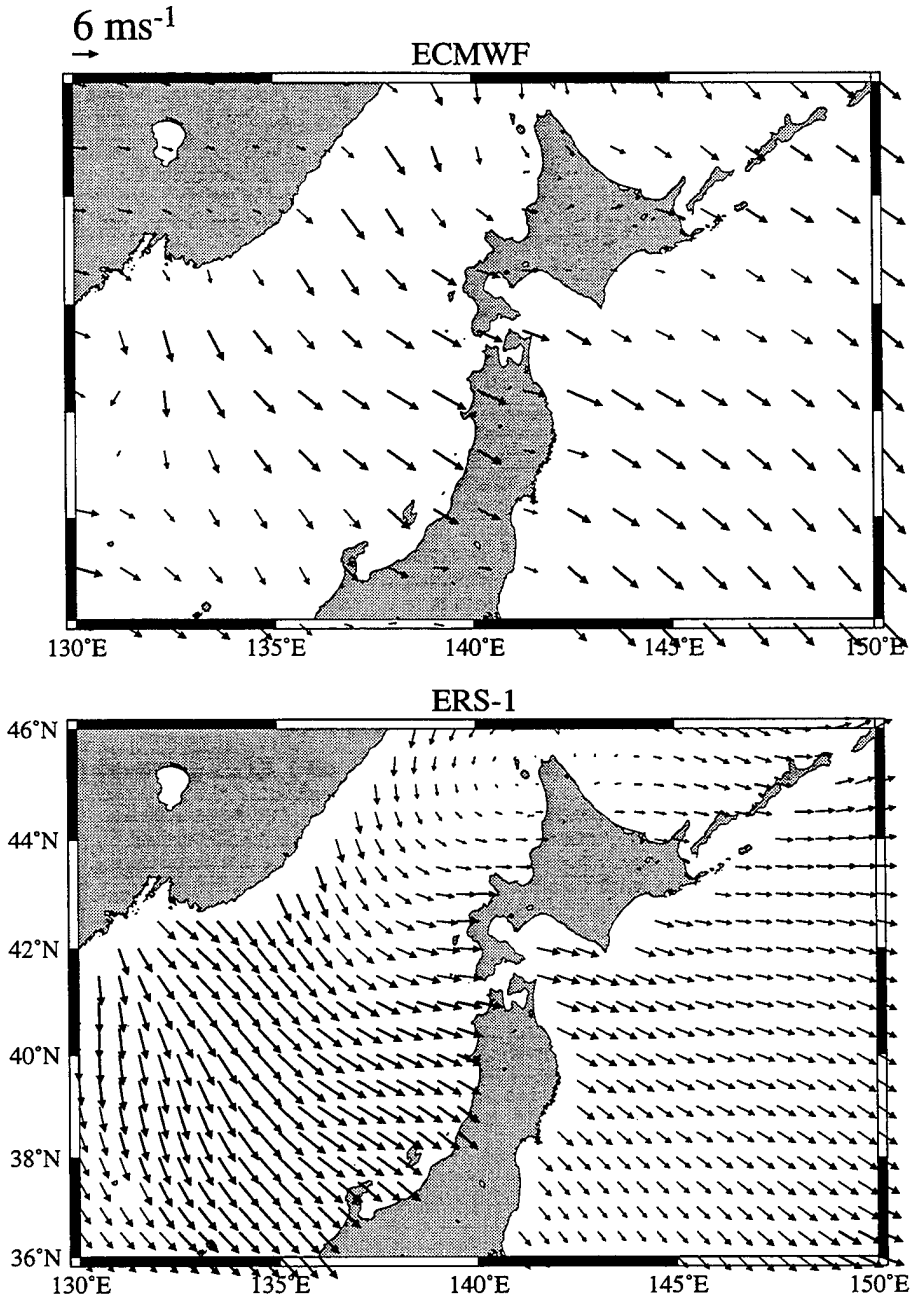

Figure 13: Comparison of ECWMF winds (top) and ERS-1 winds (bottom) for biweek 25: Dec 16–Dec 29, 1992.

4.2.1 Zonally Averaged Wind Components

A comparison of the zonally averaged winds for the North Pacific Ocean for one year (July 1992–June 1993) also shows good large scale agreement. The ERS-1 zonal wind component shows a very similar structure to the ECMWF winds, but is weaker than the

ECMWF winds between 25°and 50° N. The meridional components also show large scale agreement. However, the ERS-1 winds have a stronger southward component between 5° and 22° N, and a stronger northward component south of the equator which gives the ERS-1 winds a stronger convergence near the equator.

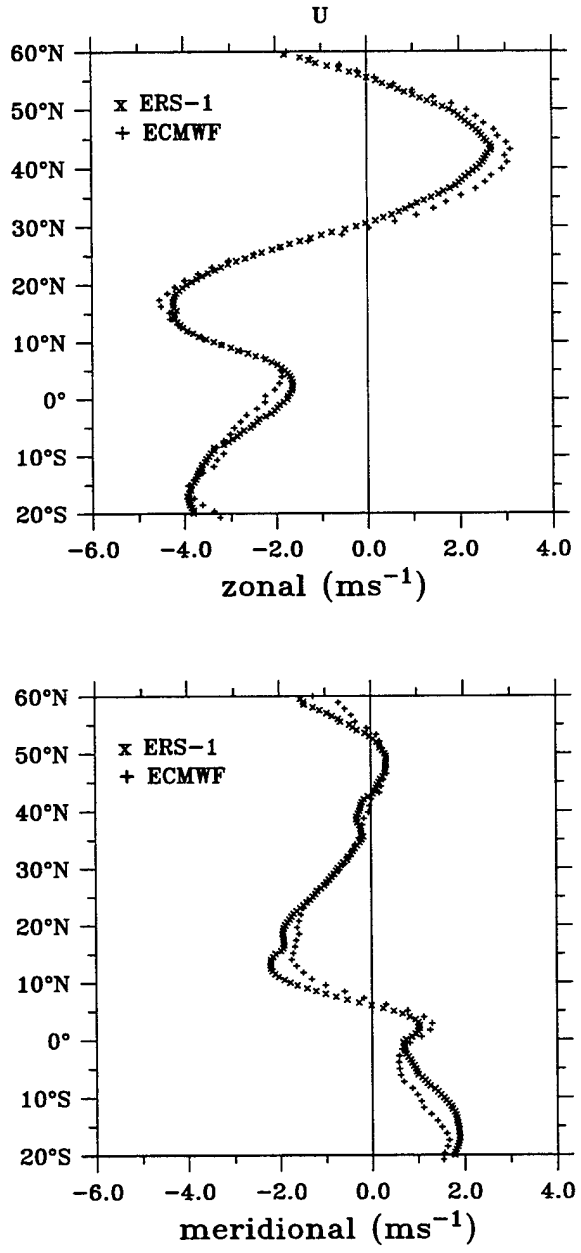

Figure 14: Comparison of the ECWMF and ERS-1 zonally averaged winds for the North Pacific Ocean.

4.3 Buoy wind comparisons

Hourly wind speed and direction measurements from 11 National Data Buoy Center (NDBC) buoys were also used to compare with the ERS-1 scatterometer estimates. Bi-weekly averages of winds were calculated for the same time periods in Table 5 for the buoy winds and the collocated ECMWF winds. The locations of the 3 buoys used in the comparison are given in Table 6 and in Figure 15.

Buoy	Latitude °N	Longitude °W
46002	42° 31'	130° 15'
46014	39° 11'	124° 00'
46022	40° 45'	124° 30'

Table 6: NDBC buoy locations.

All three buoys are in good agreement with the ERS-1 wind components. The offshore buoy (46002) shows the best agreement due to the fact that the ERS-1 has a higher number of data drop-outs near the coast. The ERS-1 estimates are occasionally influenced by individual events such as November 1992 near buoy 46002. The coastal buoys (46014 and 46022) show similar results, however, they also tend to have more negative meridional components.

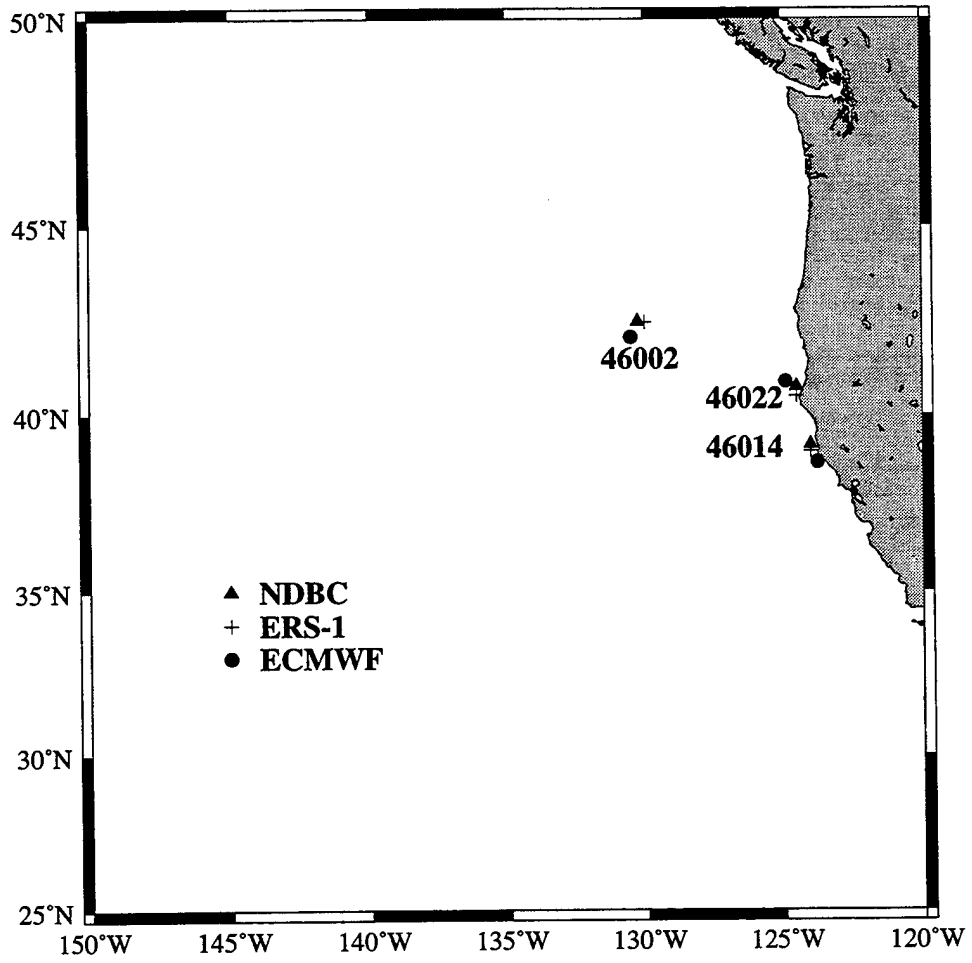

Figure 15: The locations of NDBC buoys in the North Pacific Ocean. Latitude and longitudes for all buoys are given in Table 6.

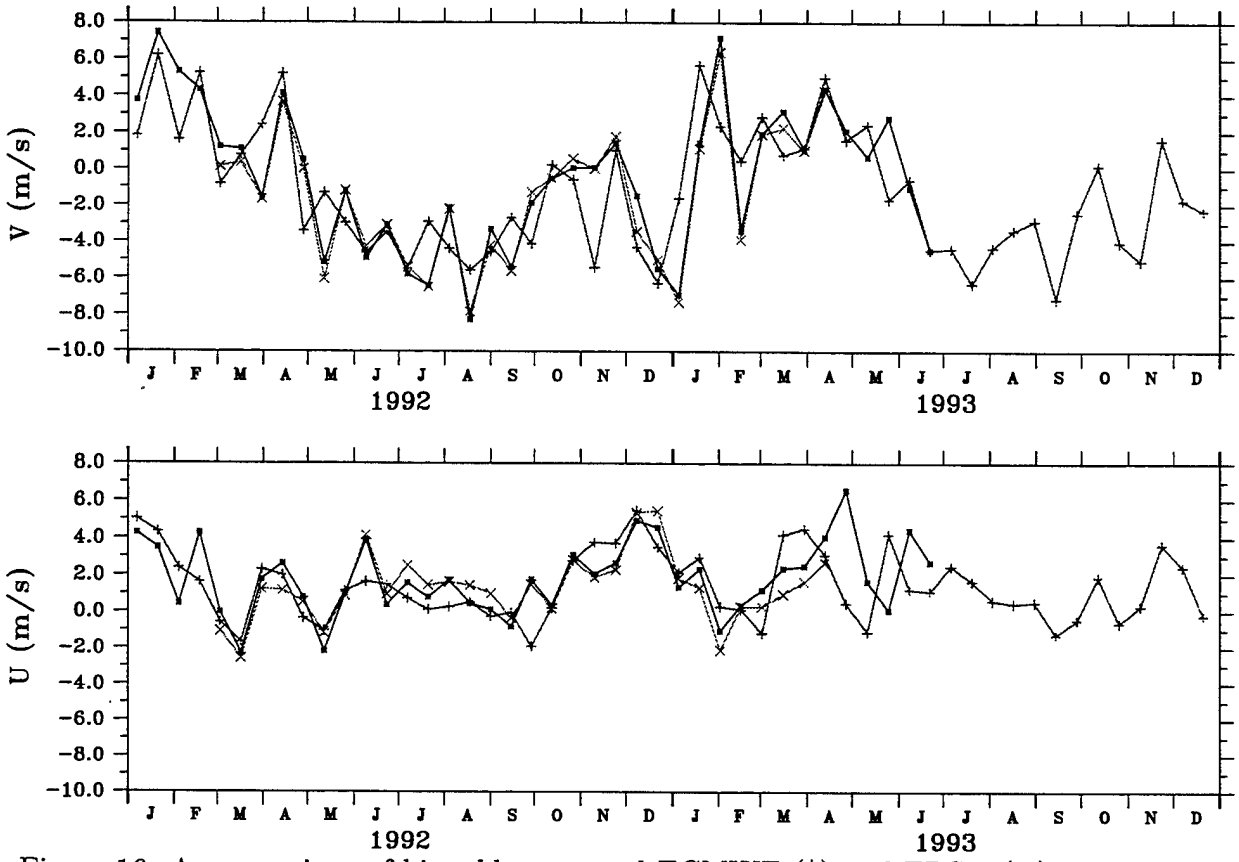

Figure 16: A comparison of biweekly averaged ECMWF (*) and ERS-1 (+) winds with NDBC buoy 46002 (x). The ERS-1 winds show good overall agreement with the buoy winds, but are occasionally influenced by single events such as November 1992.

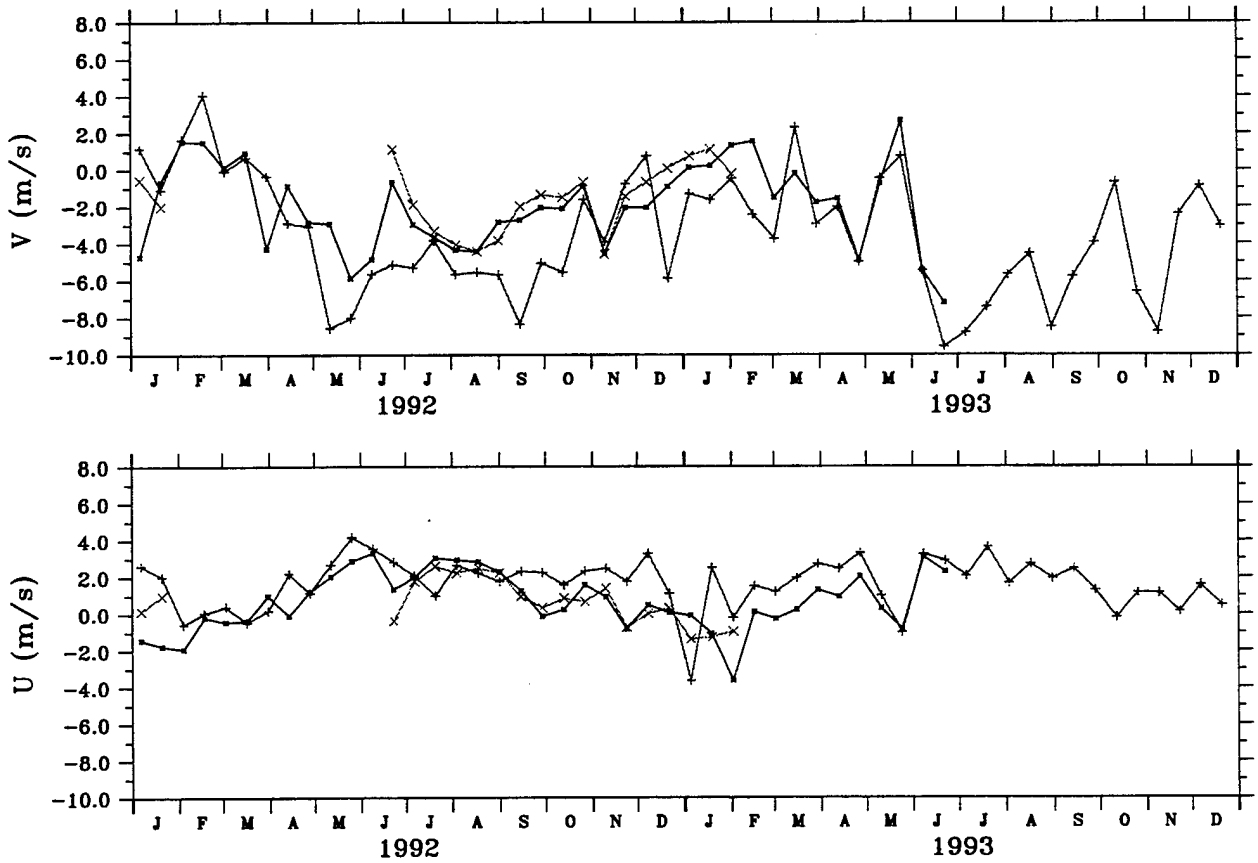

Figure 17: A comparison of biweekly averaged ECMWF (*) and ERS-1 (+) winds near NDBC buoy 46014 (x). The ERS-1 winds show good overall agreement with the buoy winds, particularly in the zonal component. The meridional component tends to be more negative (southward).

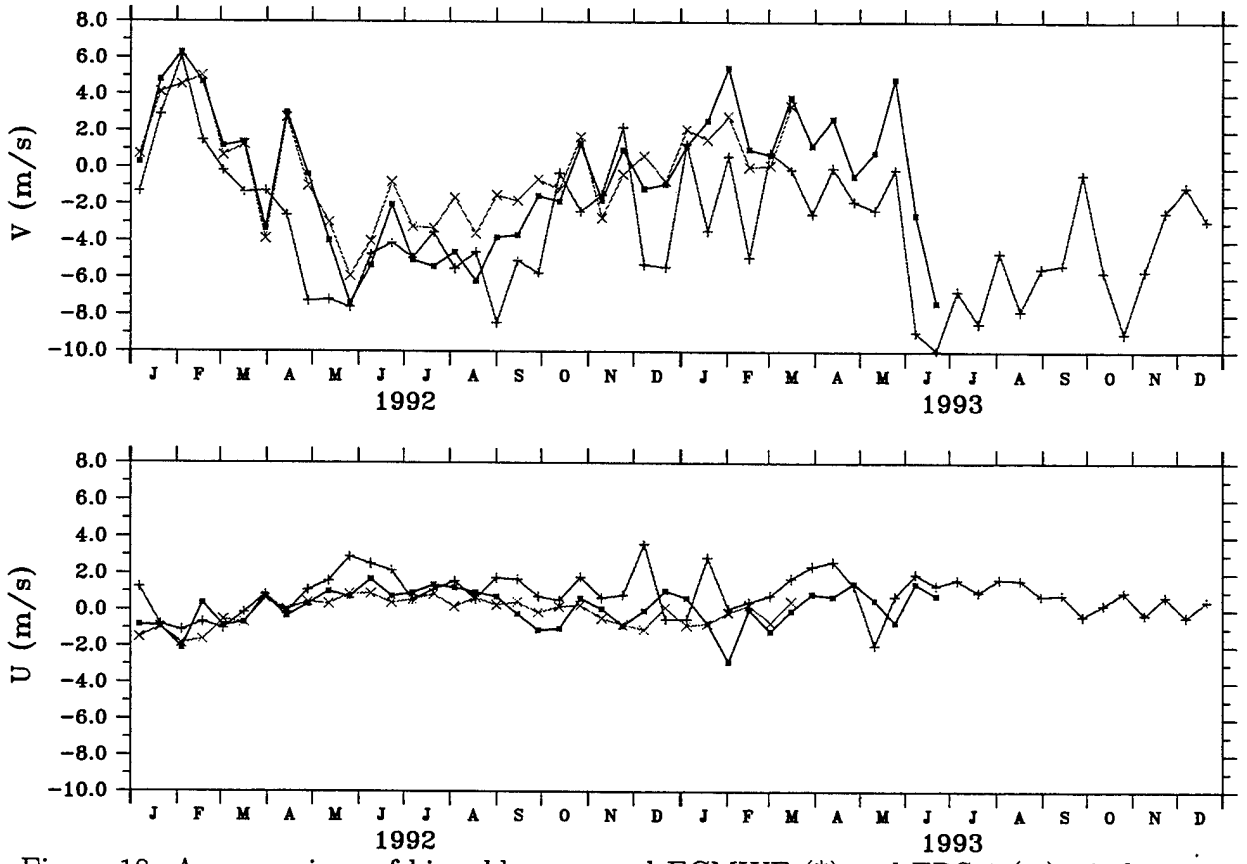

Figure 18: A comparison of biweekly averaged ECMWF (*) and ERS-1 (+) winds near NDBC buoy 46022 (x). The ERS-1 winds show good overall agreement with the buoy winds, particularly in the zonal component. The meridional component tends to be more negative (southward).

5 Results

The appendix contains plots of annual and season mean values derived from the ERS-1 scatterometer using the technique described in this report. In addition, plots of biweekly wind components and wind stress curl are also presented.

The annual winds (Appendix A) show strong interannual variability. The peaks of the zonal component of the westerlies and trade winds coincide in a given year, but the longitude varies from year-to-year. The wind stress curl has a more complicated pattern, but the zero curl line runs east-west with a northeast-southwest tilt in the North Pacific basin.

The seasonal winds (Appendix B) show strong large-scale similarities between the winter and spring components and between the summer and fall components. The most significant seasonal changes occur in the meridional component. The summer/fall meridional wind is positive [northward] whereas the winter/spring meridional wind is weak or

slightly negative. The eastern mid-latitude region has its peak southerly speed during summer, a transition during fall and a northerly speed during winter with another transition during spring. The mid-latitude zero wind stress curl line is north during summer and fall (40° N–50° N) and south during winter and spring (30° N–40° N).

6 Summary

In general, the ERS-1 scatterometer suffers from several problems. The most important seems to be the ground coverage of the single swath. The large gaps in the coverage preclude any type of daily wind maps. Although weekly wind maps are possible, the estimated errors are unacceptably high. In this report, we show that it is possible to create biweekly wind maps with acceptable errors. Another major problem with the ERS-1 scatterometer is the large number of missing data due to errors in selecting the correct ambiguity and the lack of directional information at low wind speeds. The estimation technique used here provides a more robust estimate of the biweekly mean than simple averaging due to the irregular temporal spacing of the data. This technique is not heavily biased if the only measurement in the two-week period is made during a large storm.

The scatterometer winds have large-scale agreement with ECMWF 10-m winds. Major differences occur in patches, due to sampling errors and occasional problems with the median filter used by JPL to remove the vector ambiguities in the winds.

Acknowledgements

Funding for this project was provided by the National Aeronautics and Space Administration under contract number 765200 (NSCAT) and the Office of Naval Research under the Eastern Boundary Current N00014-92-J-1486 and Kuroshio Extension Regional Experiment initiative N00014-92-J-1656 contracts.

7 References

Bentamy, A., Y. Quilfen, F. Gohin, N. Grima, M. Lenaour, and J. Servain, 1996. Determination and validation of average wind fields from ERS-1 scatterometer measurements. *The Global Atmosphere and Ocean System*, **4**, 1–29.

Cardone, V.J, H.C. Graber, R.E. Jensen, S. Hasselmann and M.J. Caruso, 1995. In search of the true surface wind field in SWADE IOP-1: Ocean wave modelling perspective. *Global Atm. and Ocean Sys.*, **3(2–3)**, 107–150.

Chelton, D.B., and M.G. Schlax, 1991. Estimation of time-averaged chlorophyll concentration from irregularly spaced satellite observations. *J. Geophys. Res.*, **96**, 14,669–14,692.

Freilich, M.H., and R.S. Dunbar, 1992. A preliminary C-band scatterometer model function for the ERS-1 AMI instrument, Proceedings of the First ERS-1 Symposium: Space at the Service of our Environment, Cannes, 4–6 November, 1992, **ESA SP-359**, European Space Agency, Paris.

Kelly, K.A., and M.J. Caruso, 1990. A modified objective mapping technique for scatterometer wind data. *J. Geophys. Res.*, **95**, 13,483–13,496.

Large, W.G., and S. Pond, 1981. Open ocean momentum flux measurements in moderate and strong winds. *J. Phys. Oceanogr.*, **11**, 324–336.

Tang, W., and W. T. Liu, 1996. Objective Interpolation of Scatterometer Winds. *Jet Propulsion Laboratory*, JPL Publication 96-19.

Vass, P., and B. Battrick, 1992. ERS-1 System, **ESA SP-1146**, European Space Agency.

Wright, D.G., and K.R. Thompson, 1982. Time-averaged forms of the nonlinear stress law. *J. Phys. Oceanogr.*, **13**, 341–345.

A Annual winds

This section contains plots of the annual mean zonal and meridional wind components for the North Pacific ocean (20°–62° N, 109°–285° E). The contour interval for these plots is 1 $ms^{-1}$for the wind components and 0.5 $\times 10^{-7}$ Nm^{-3} for the wind stress curl. Figure 19 shows the mean components from 1992–1995. Figures 20 to 23 show the annual means from 1992 to 1995 respectively and Figures 24 to 27 show the departures of the annual means from the four year mean.

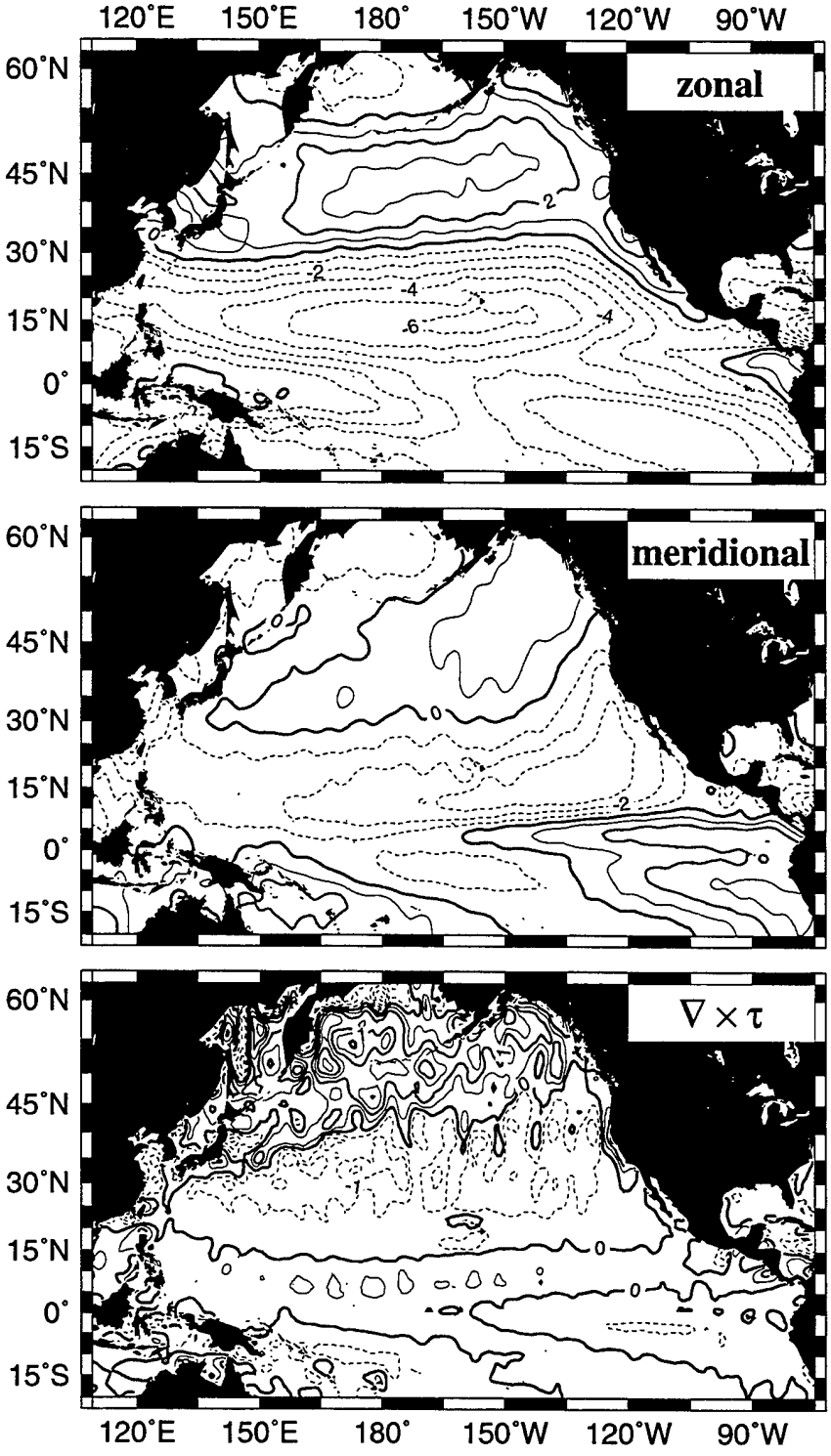

Figure 19: 1992–1995 mean wind components and wind stress curl. Contour interval is 1.0 ms^{-1} for the wind components and 0.5×10^{-7} Nm^{-3} for the wind stress curl.

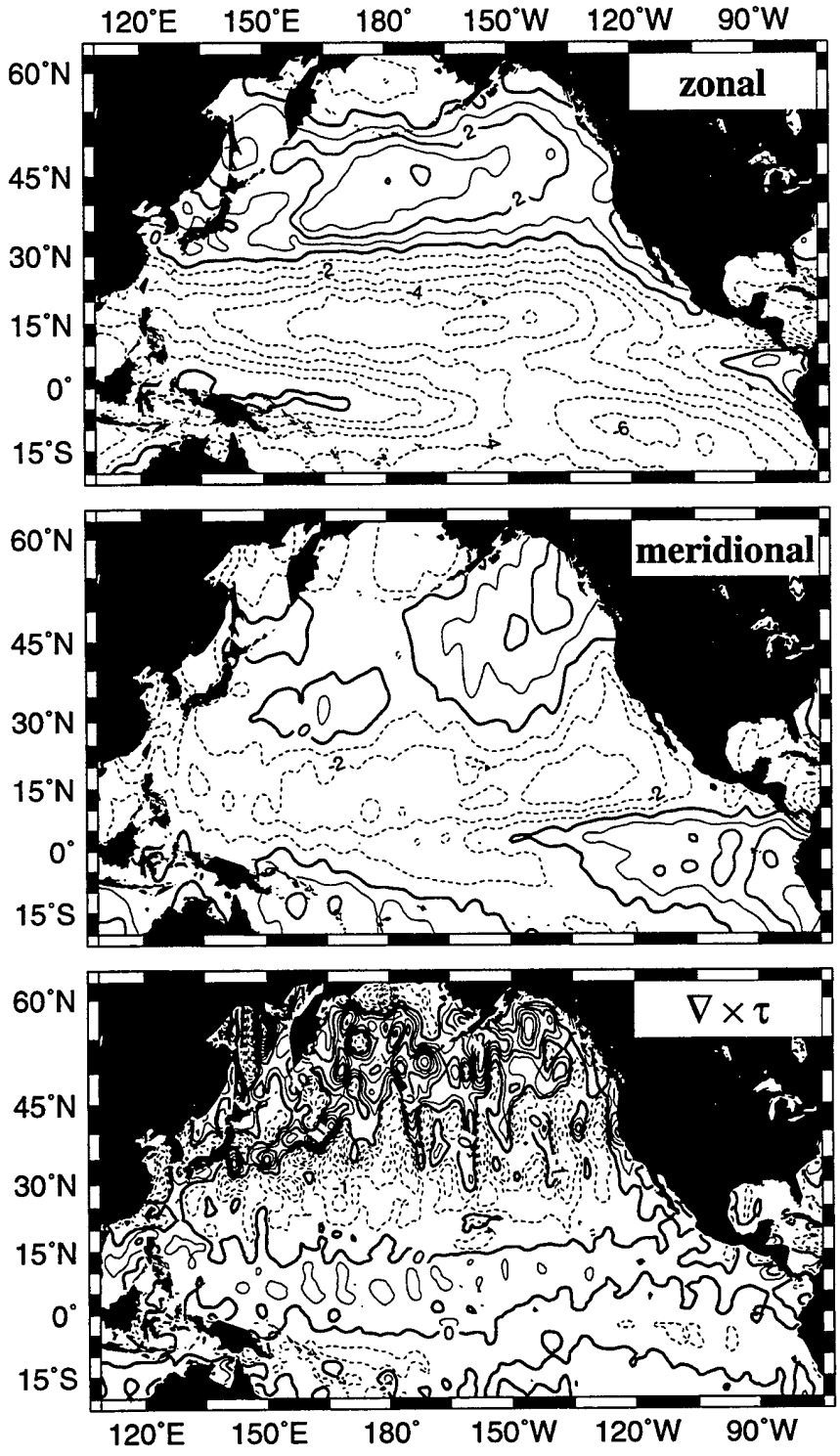

Figure 20: 1992 mean wind components and wind stress curl. Contour interval is 1.0 ms^{-1} for the wind components and 0.5×10^{-7} Nm^{-3} for the wind stress curl.

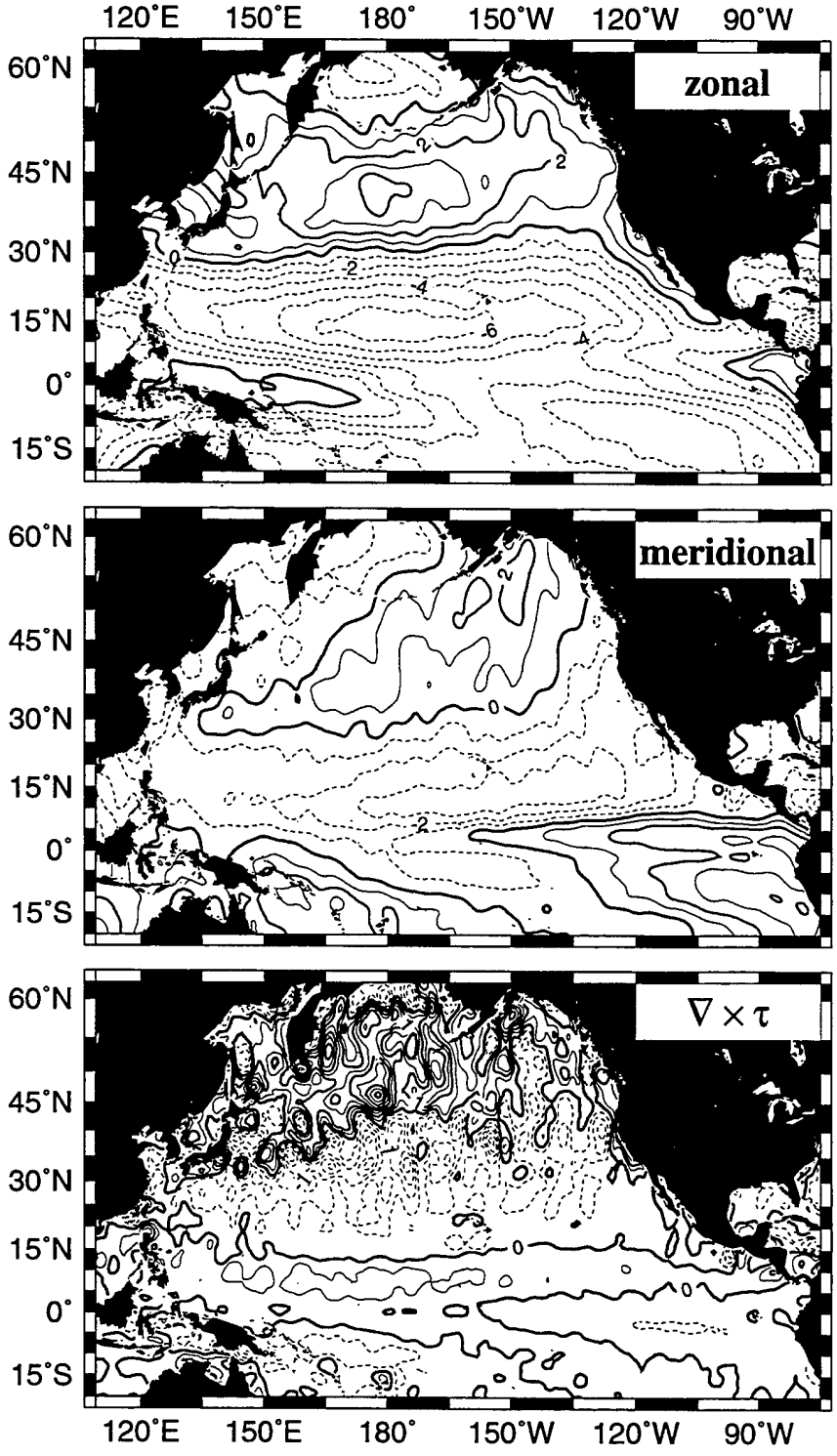

Figure 21: 1993 mean wind components and wind stress curl. Contour interval is 1.0 ms^{-1} for the wind components and 0.5×10^{-7} Nm^{-3} for the wind stress curl.

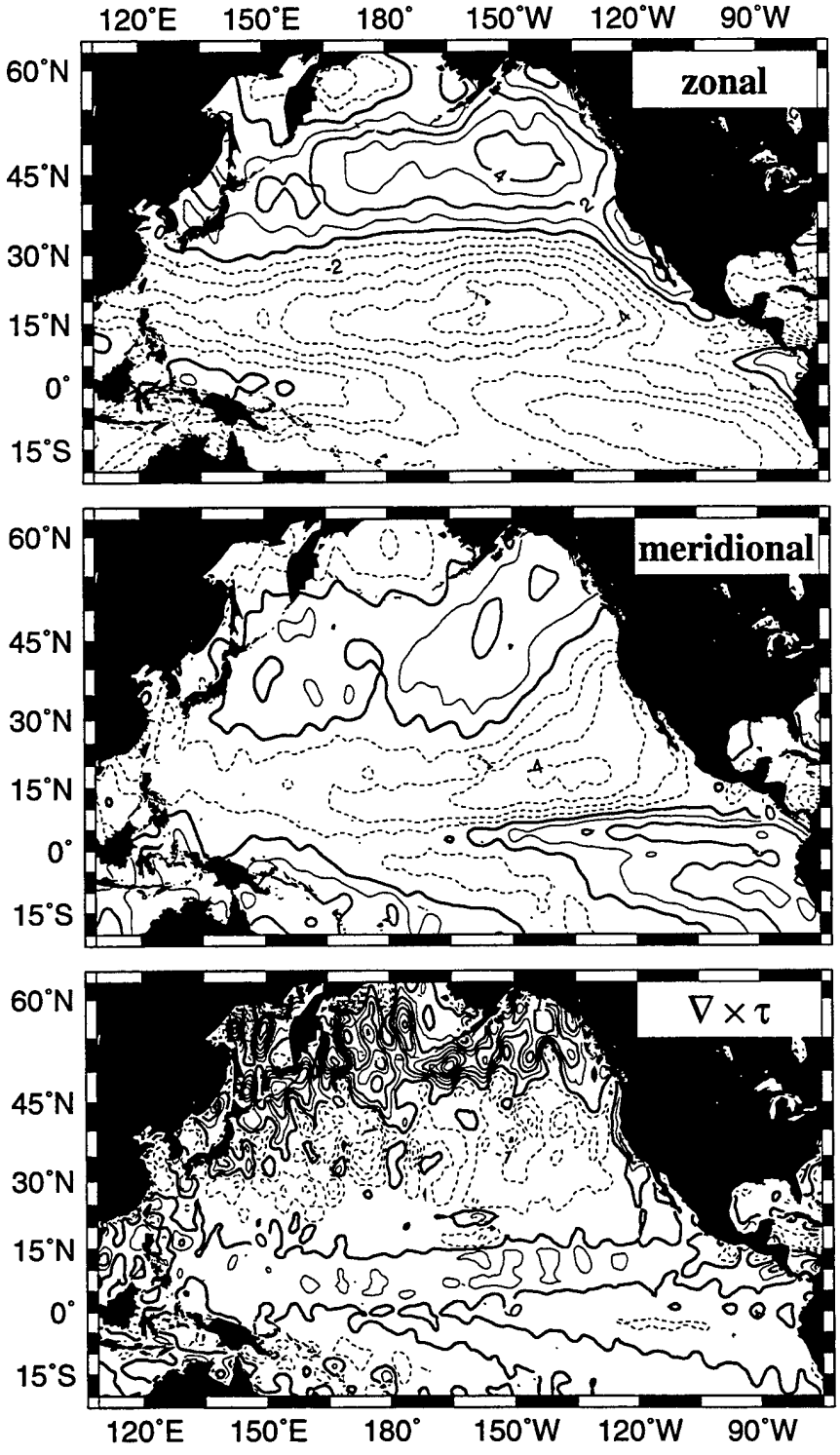

Figure 22: 1994 mean wind components and wind stress curl. Contour interval is 1.0 ms^{-1} for the wind components and 0.5×10^{-7} Nm^{-3} for the wind stress curl.

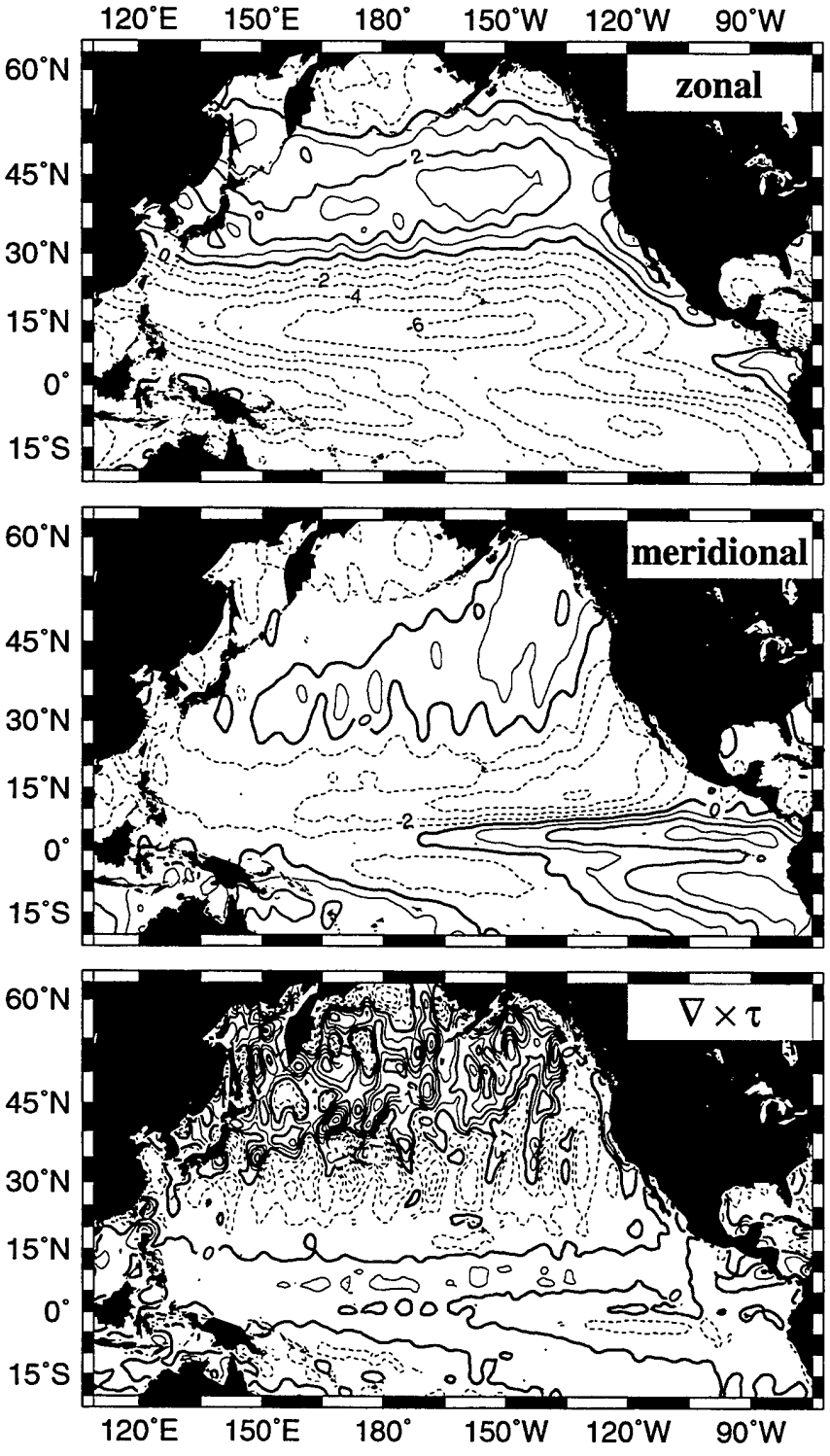

Figure 23: 1995 mean wind components and wind stress curl. Contour interval is 1.0 ms^{-1} for the wind components and 0.5×10^{-7} Nm^{-3} for the wind stress curl.

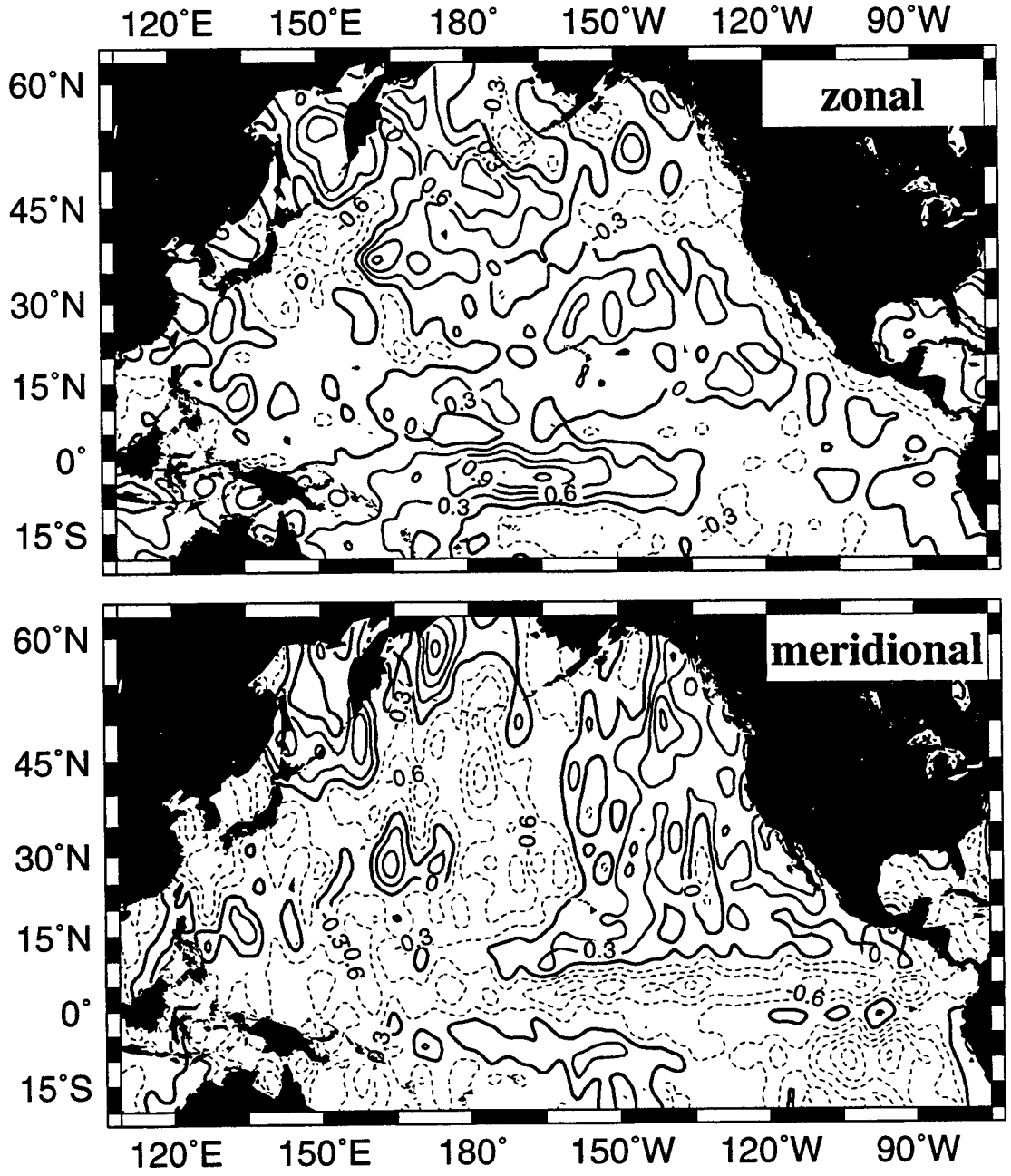

Figure 24: Variance of the 1992 mean wind components from the 1992–1995 mean. Contour interval is 0.3 ms^{-1} for the wind components.

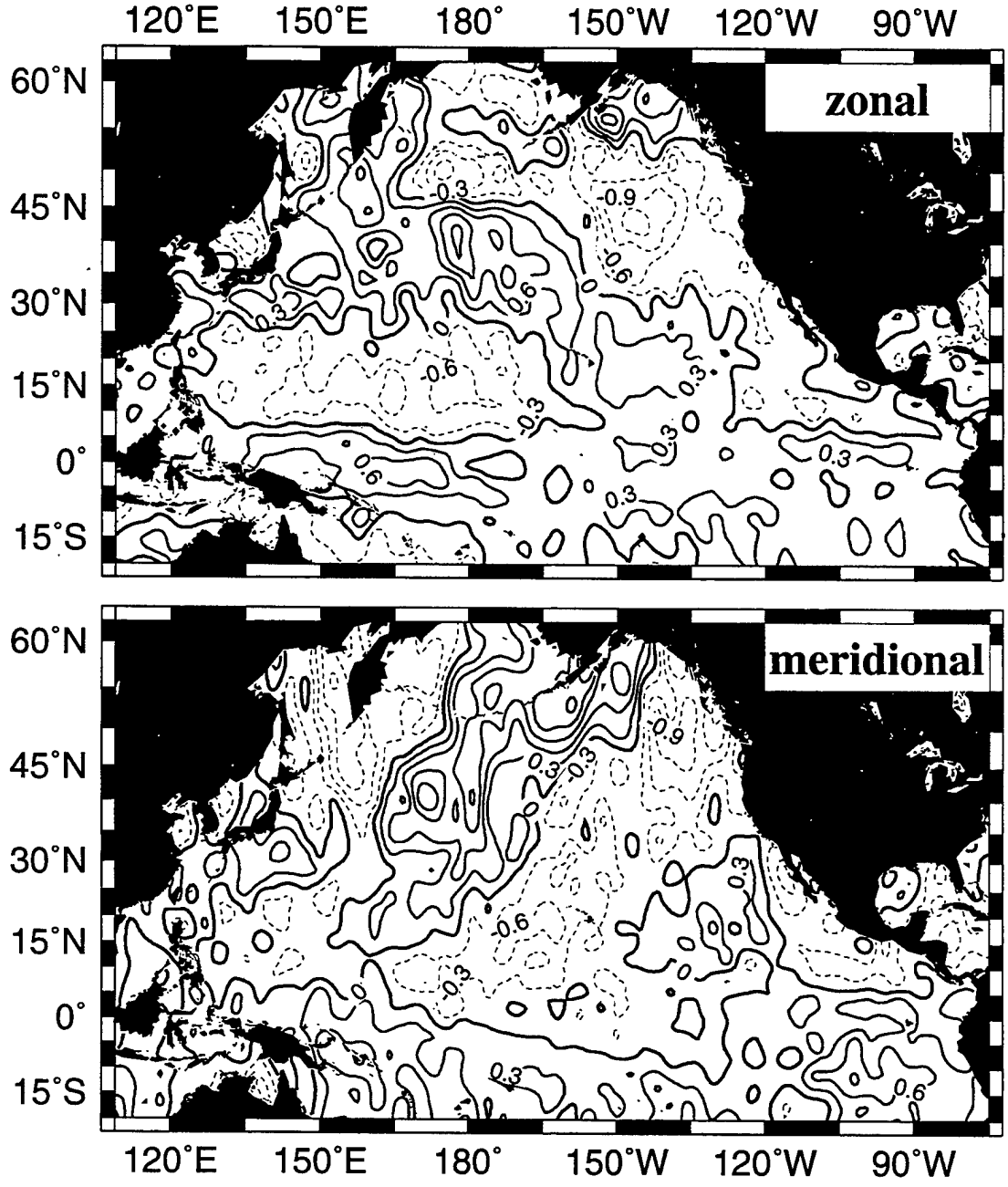

Figure 25: Variance of the 1993 mean wind components from the 1992–1995 mean. Contour interval is 0.3 ms^{-1} for the wind components.

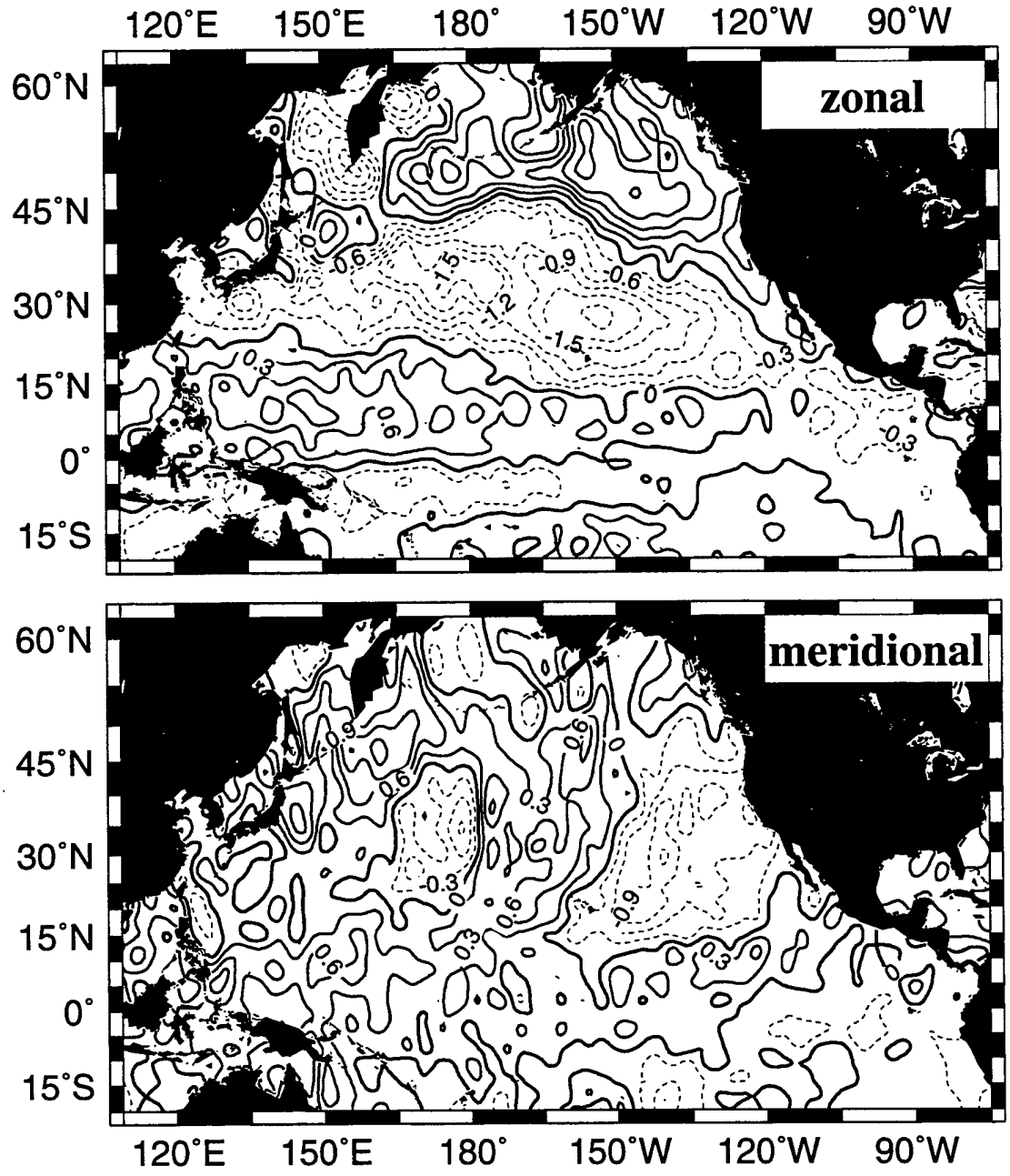

Figure 26: Variance of the 1994 mean wind components from the 1992–1995 mean. Contour interval is 0.3 ms^{-1} for the wind components.

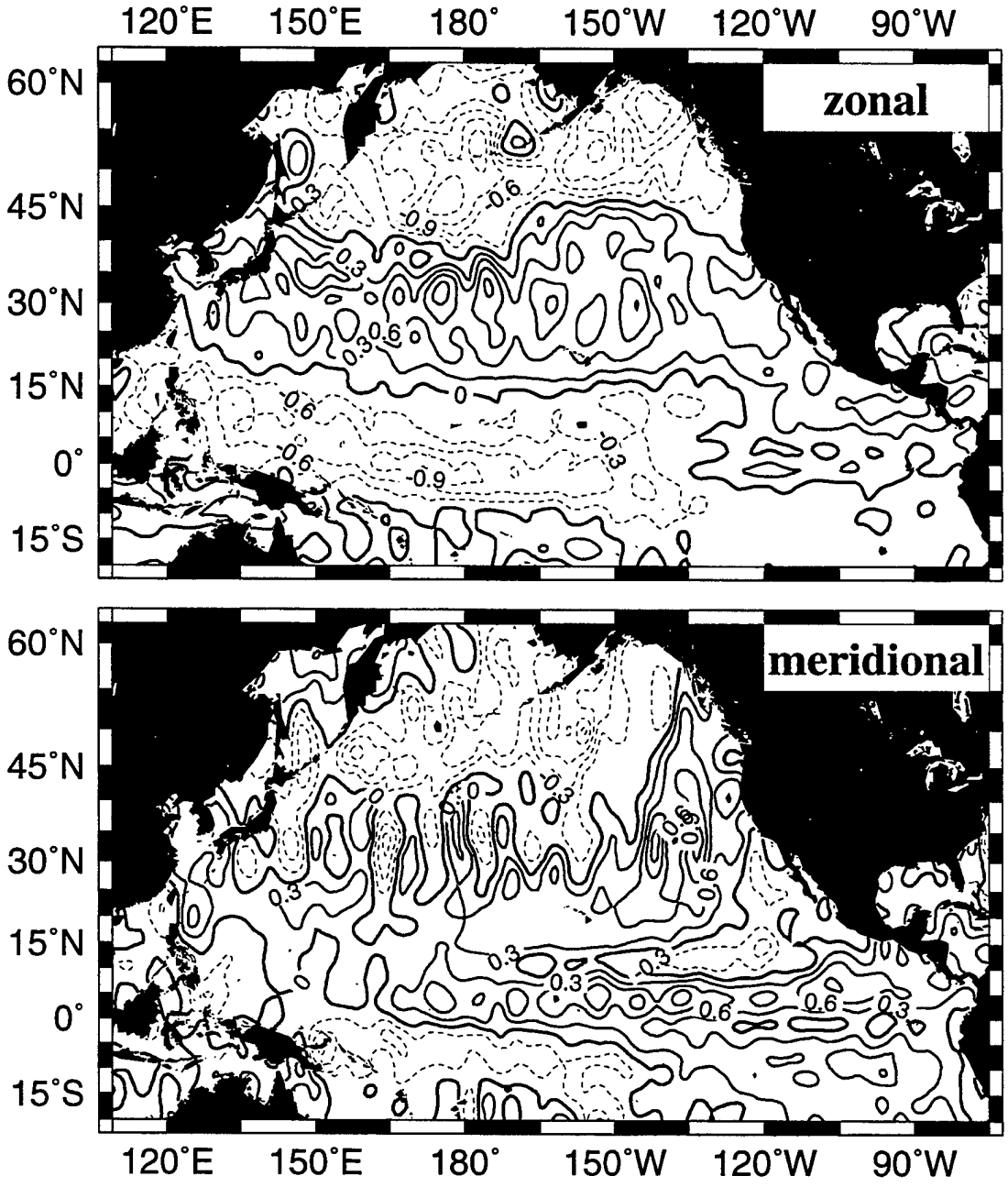

Figure 27: Variance of the 1995 mean wind components from the 1992–1995 mean. Contour interval is 0.3 ms^{-1} for the wind components.

B Seasonal winds

This section contains plots of the seasonal mean zonal and meridional wind components for the North Pacific ocean (20°–62° N, 109°–285° E). The contour interval for these plots is 1 ms^{-1} for the wind components and 0.5×10^{-7} Nm^{-3} for the wind stress curl. Table 7 contains a list of the months used to calculate seasonal averages.

Season	**Months**
Winter	January, February, March
Spring	April, May, June
Summer	July, August, September
Fall	October, November, December

Table 7: The months used to calculate seasonal averages.

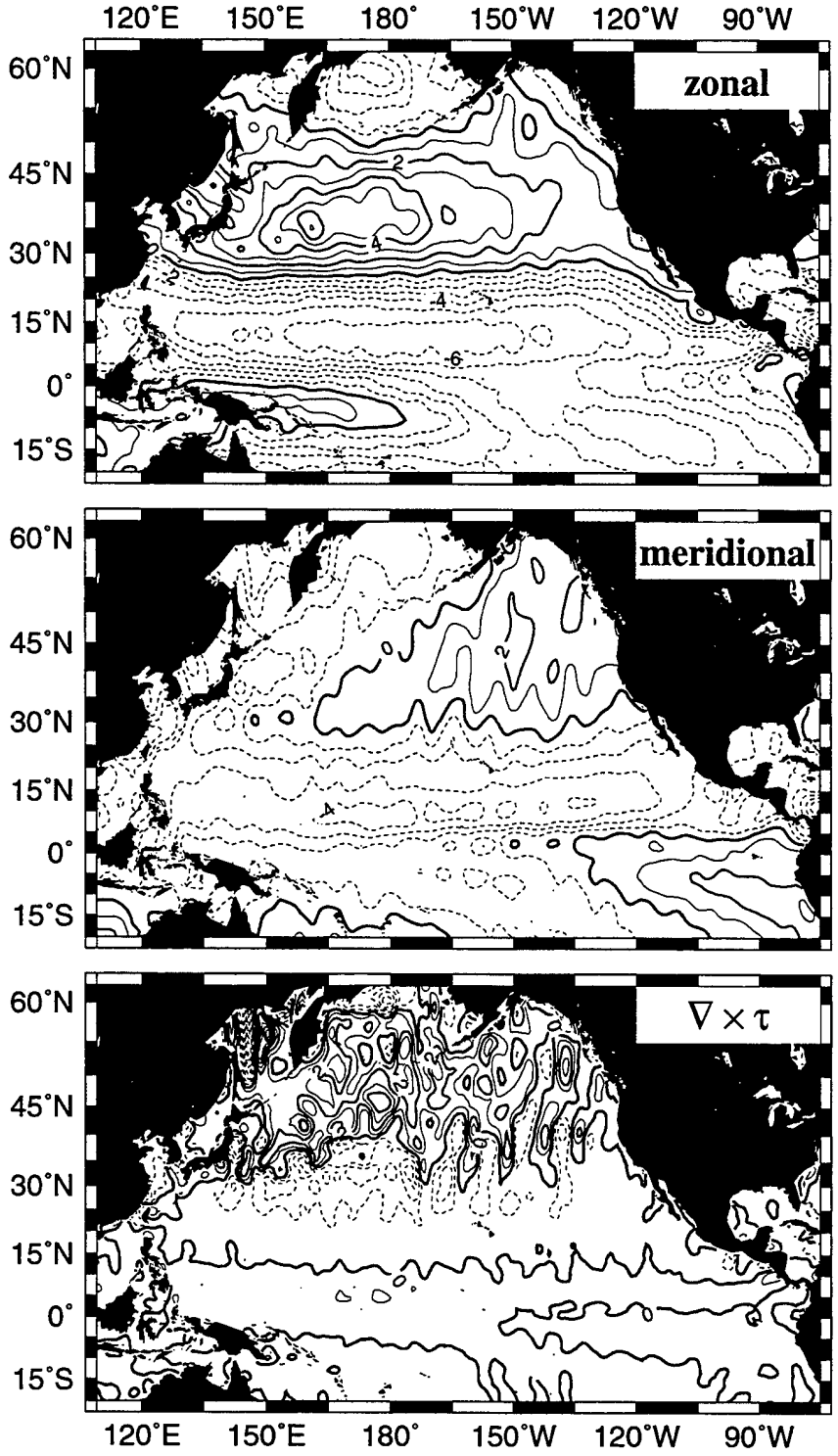

Figure 28: Winter 1992–1995 mean wind components and wind stress curl. Contour interval is 1.0 ms^{-1} for the wind components and $0.5 \times 10^{-7} Nm^{-3}$ for the wind stress curl.

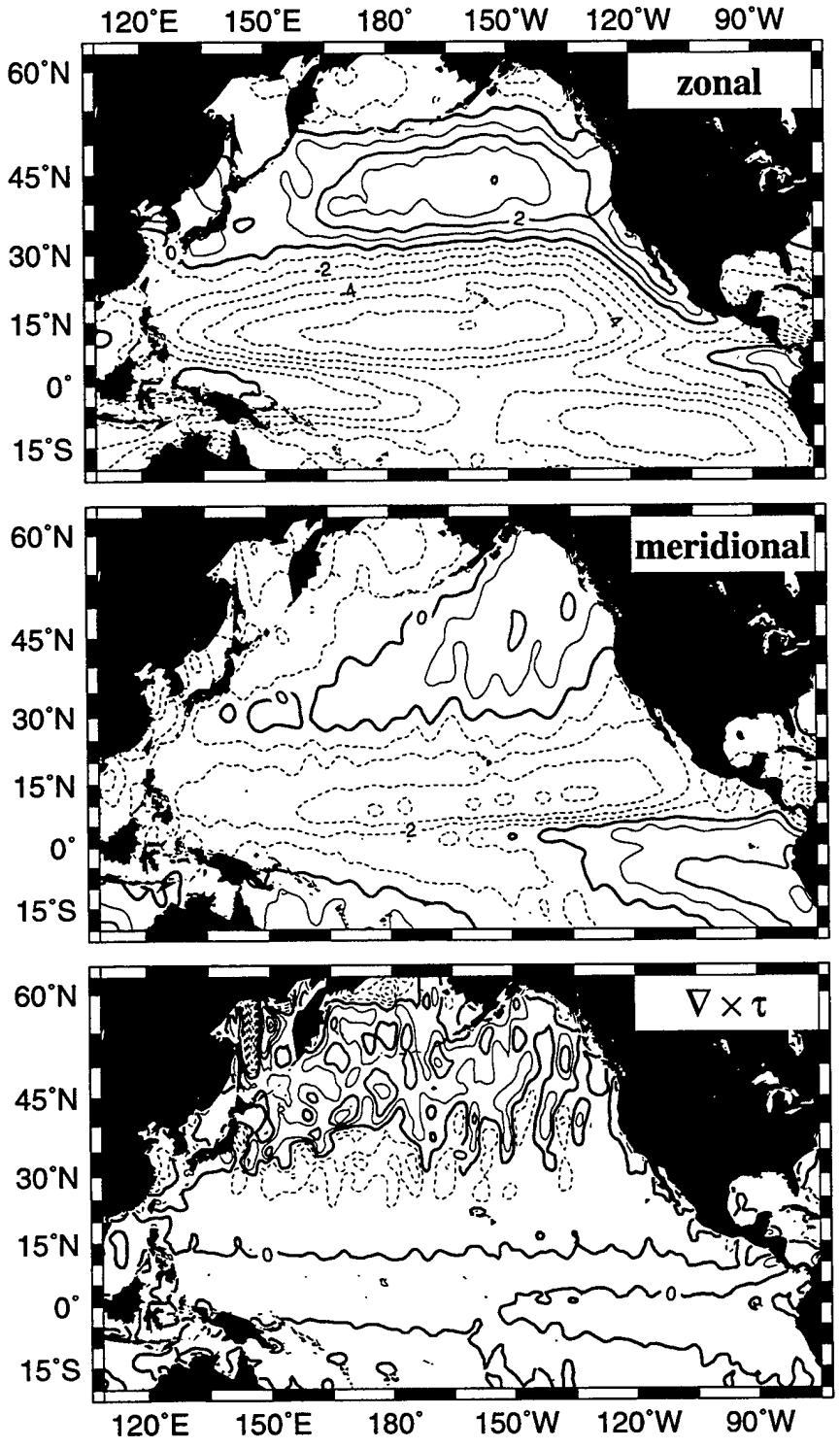

Figure 29: Spring 1992–1995 mean wind components and wind stress curl. Contour interval is 1.0 ms^{-1} for the wind components and $0.5 \times 10^{-7} Nm^{-3}$ for the wind stress curl.

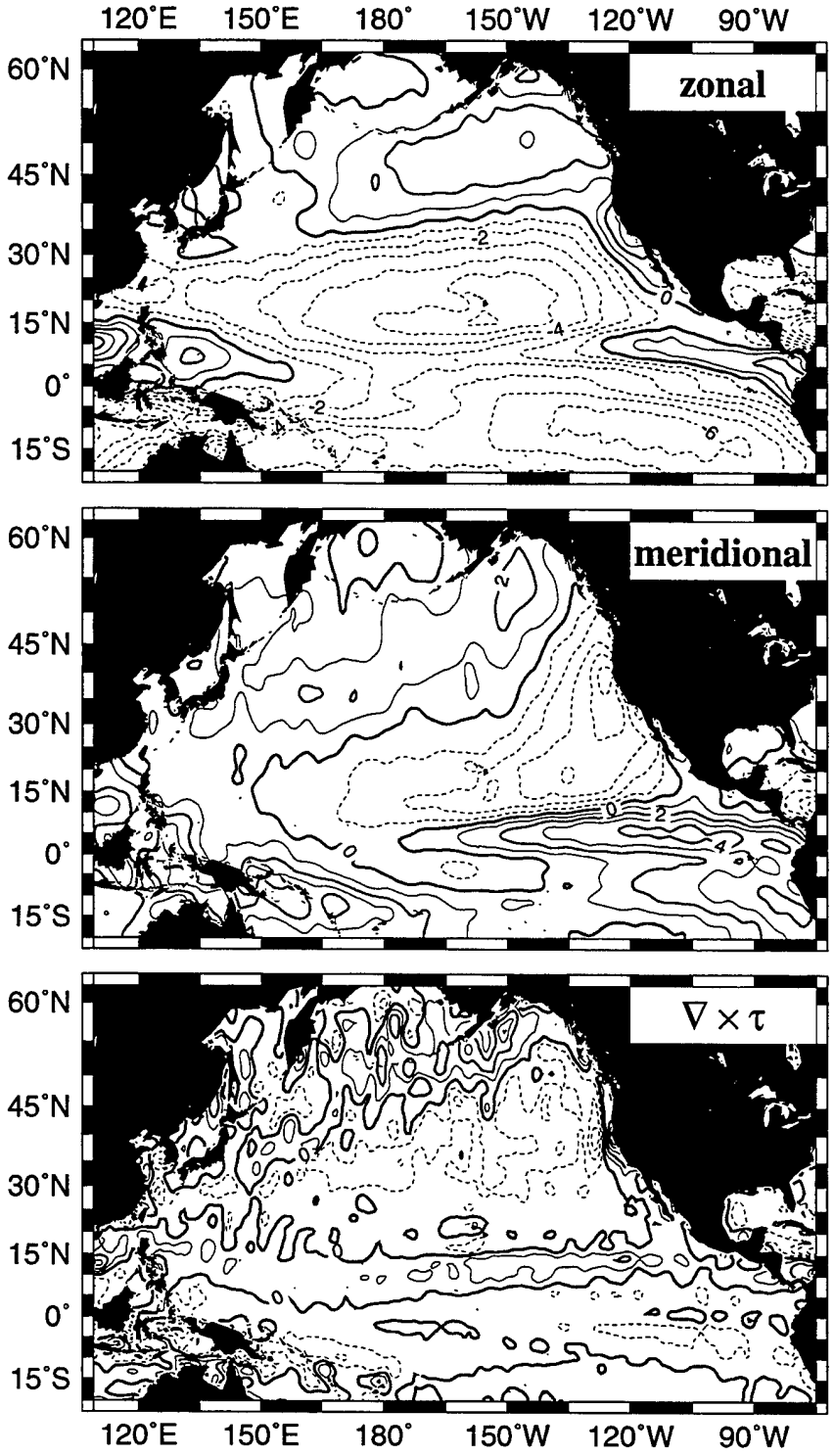

Figure 30: Summer 1992–1995 mean wind components and wind stress curl. Contour interval is 1.0 ms^{-1} for the wind components and $0.5 \times 10^{-7} Nm^{-3}$ for the wind stress curl.

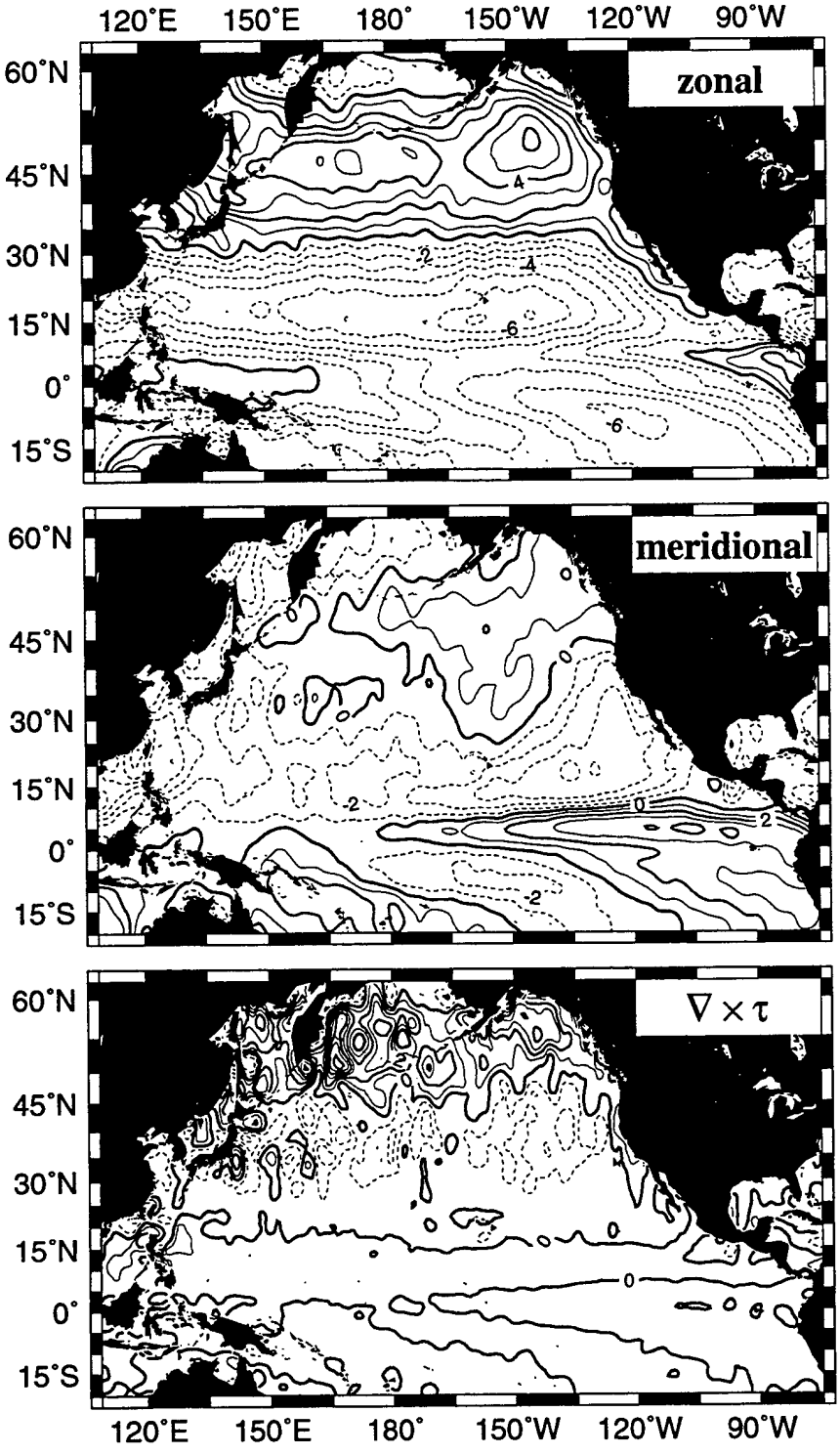

Figure 31: Fall 1992–1995 mean wind components and wind stress curl. Contour interval is 1.0 ms^{-1} for the wind components and $0.5 \times 10^{-7} Nm^{-3}$ for the wind stress curl.

C Monthly winds

This section contains plots of sample biweekly and the monthly mean zonal and meridional wind components for the North Pacific ocean (20°–62° N, 109°–285° E) and vector plots for the Northeast Pacific (25°–50° N, 210°–240° E). A complete list of the averaging intervals is given in Table 8.

Month	1992		1993	
	Start Date	End Date	Start Date	End Date
00	Jan 1	Jan 28	Dec 30	Jan 26
01	Jan 29	Feb 25	Jan 27	Feb 23
02	Feb 26	Mar 24	Feb 24	Mar 23
03	Mar 25	Apr 21	Mar 24	Apr 20
04	Apr 22	May 19	Apr 21	May 18
05	May 20	Jun 16	May 19	Jun 15
06	Jun 17	Jul 14	Jun 16	Jul 13
07	Jul 15	Aug 11	Jul 14	Aug 10
08	Aug 12	Sep 8	Aug 11	Sep 7
09	Sep 9	Oct 6	Sep 8	Oct 5
10	Oct 7	Nov 3	Oct 6	Nov 2
11	Nov 4	Dec 1	Nov 3	Nov 30
12	Dec 2	Dec 29	Dec 1	Dec 28

Month	1992		1993	
	Start Date	End Date	Start Date	End Date
00	Dec 29	Jan 25	Dec 28	Jan 24
01	Jan 26	Feb 22	Jan 25	Feb 21
02	Feb 23	Mar 22	Feb 22	Mar 21
03	Mar 23	Apr 19	Mar 22	Apr 18
04	Apr 20	May 17	Apr 19	May 16
05	May 18	Jun 14	May 17	Jun 13
06	Jun 15	Jul 12	Jun 14	Jul 11
07	Jul 13	Aug 9	Jul 10	Aug 8
08	Aug 10	Sep 6	Aug 9	Sep 5
09	Sep 7	Oct 4	Sep 6	Oct 3
10	Oct 5	Nov 1	Oct 4	Oct 31
11	Nov 2	Nov 29	Nov 1	Nov 28
12	Nov 30	Dec 27	Nov 29	Dec 26

Table 8: Periods for monthly averages.

North Pacific components

This section contains plots of sample biweekly and the monthly mean zonal and meridional wind components for the North Pacific ocean (20°–62° N, 109°–285° E). Figures 32 and 33 show an example of biweekly wind components for the beginning of July for 1992–1995. Figures 34 to 61 show the plots of the monthly averages. A complete list of the monthly averaging intervals is given in Table 8.

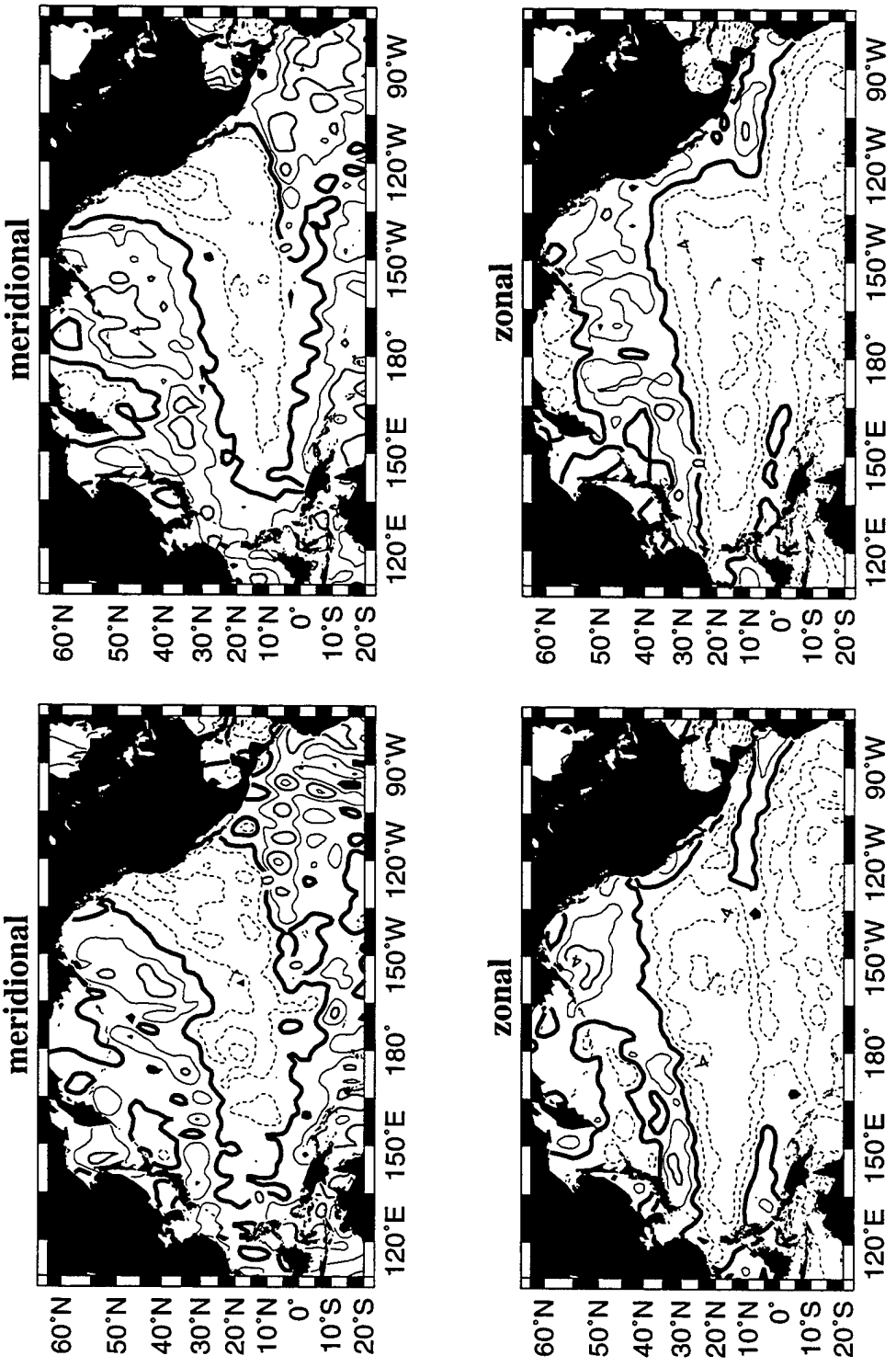

Figure 32: Wind components for July 1–July 14, 1992 (left) and June 30–July 13, 1993 (right). Contour interval is 2.0 ms^{-1} for the wind components

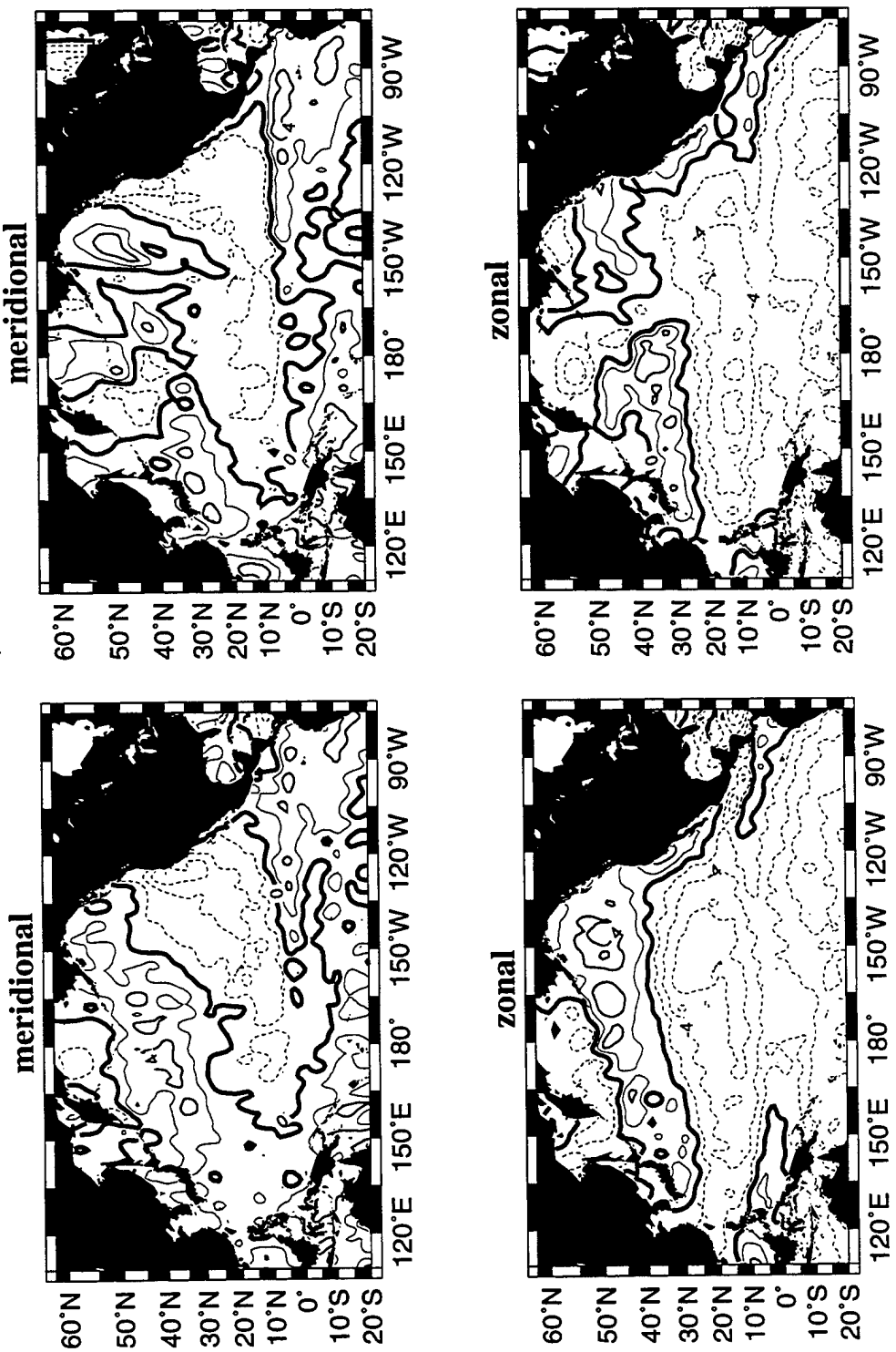

Figure 33: Wind components for June 29–July 12, 1994 (left) and June 28–July 11, 1995 (right). Contour interval is 2.0 ms^{-1} for the wind components

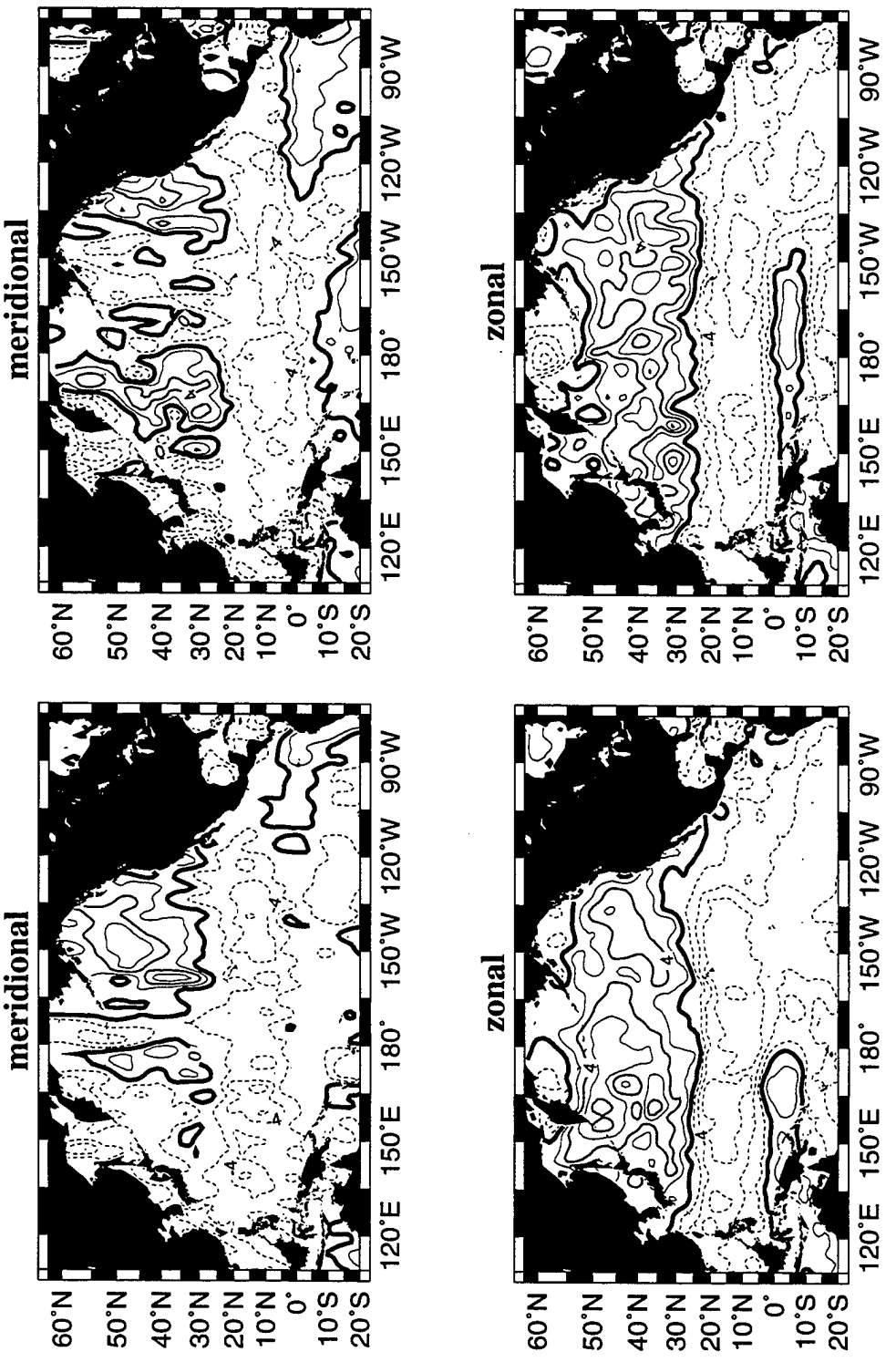

Figure 34: Wind components for January 1–January 28, 1992 (left) and January 29–February 25, 1992 (right). Contour interval is 2.0 ms^{-1} for the wind components

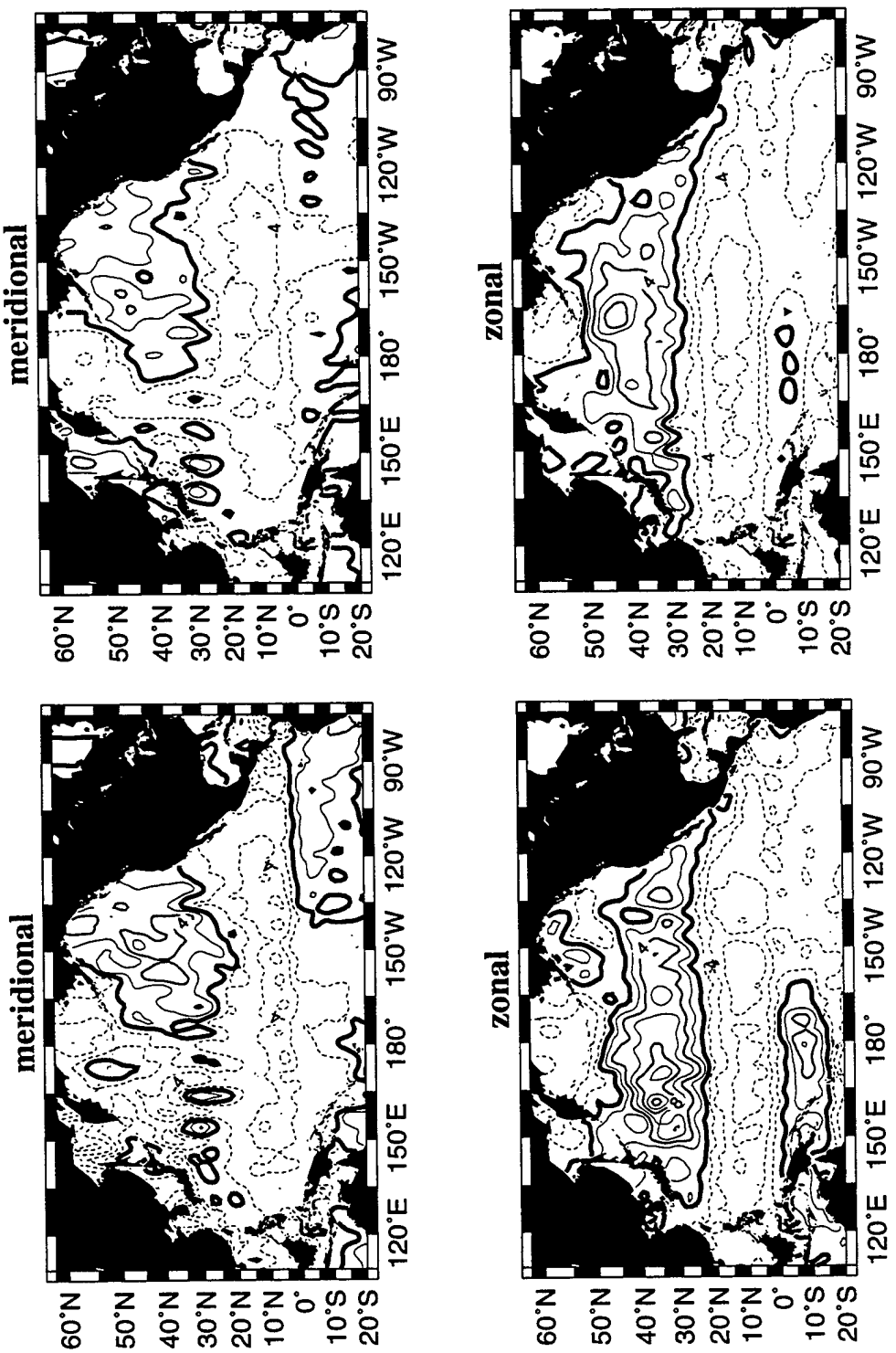

Figure 35: Wind components for February 26–March 24, 1992 (left) and March 25–April 21, 1992 (right). Contour interval is 2.0 ms^{-1} for the wind components

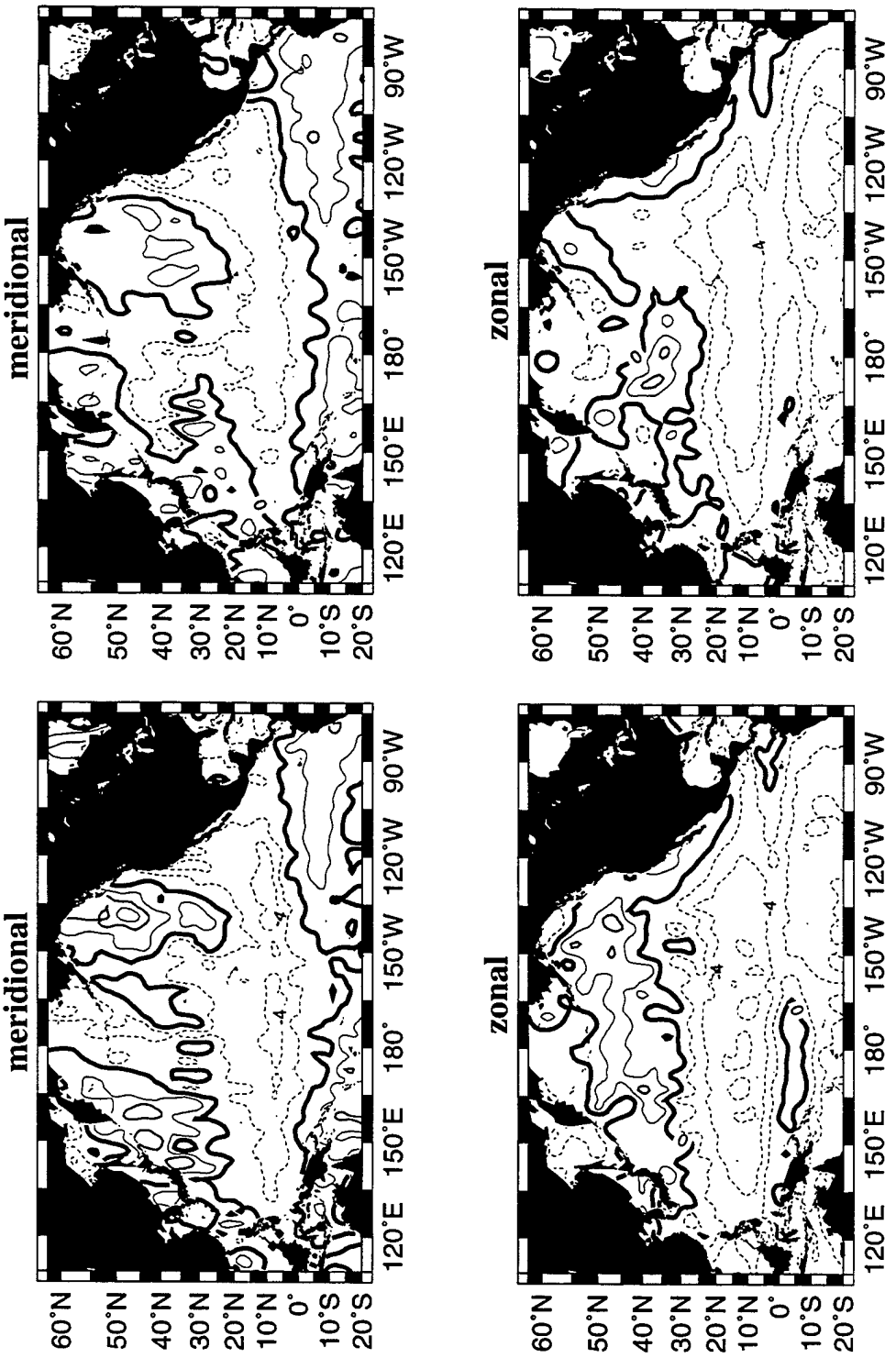

Figure 36: Wind components for April 22–May 19, 1992 (left) and May 20–June 16, 1992 (right). Contour interval is 2.0 ms^{-1} for the wind components

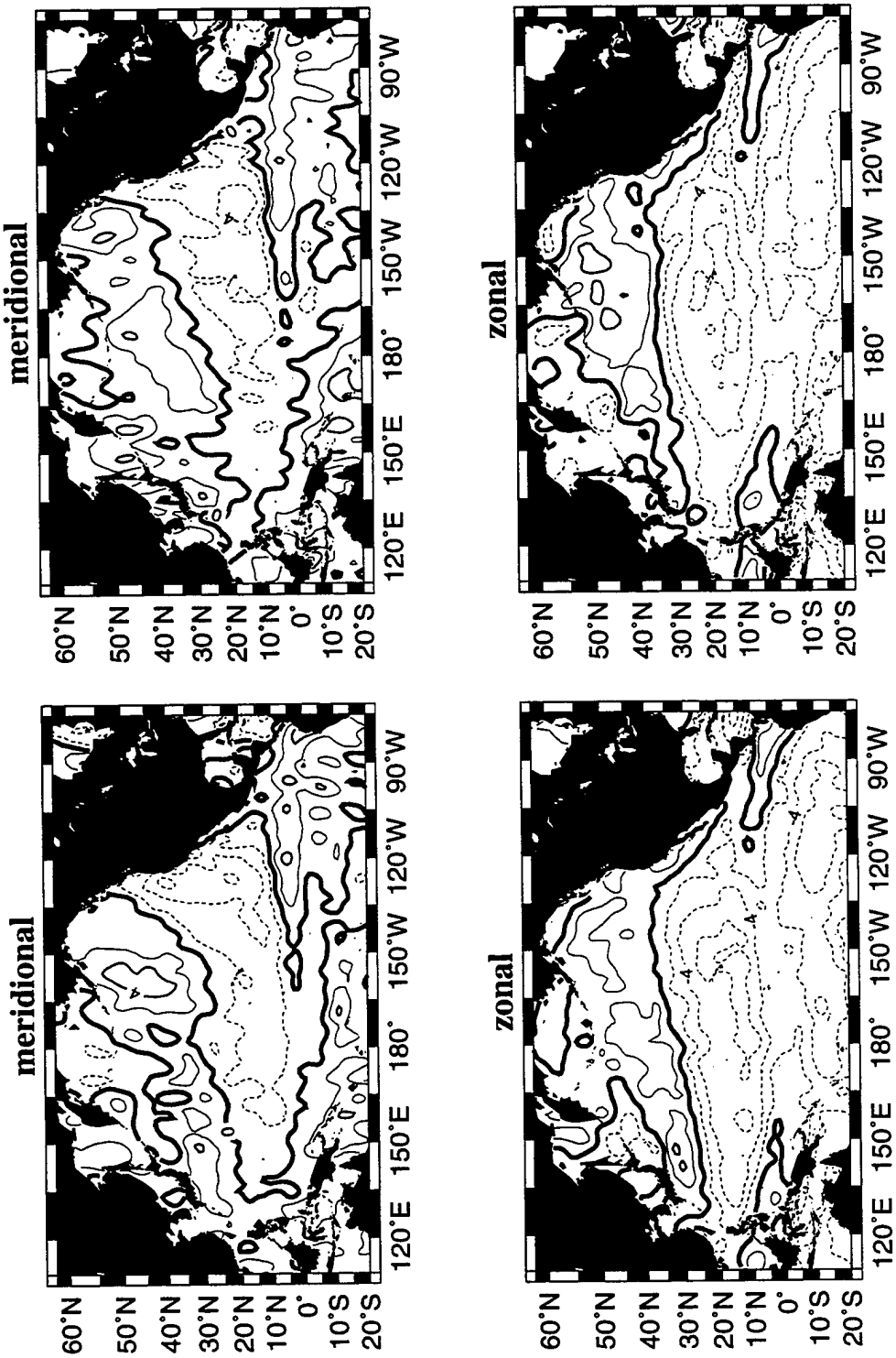

Figure 37: Wind components for June 17–July 14, 1992 (left) and July 15–August 11, 1992 (right). Contour interval is 2.0 ms^{-1} for the wind components

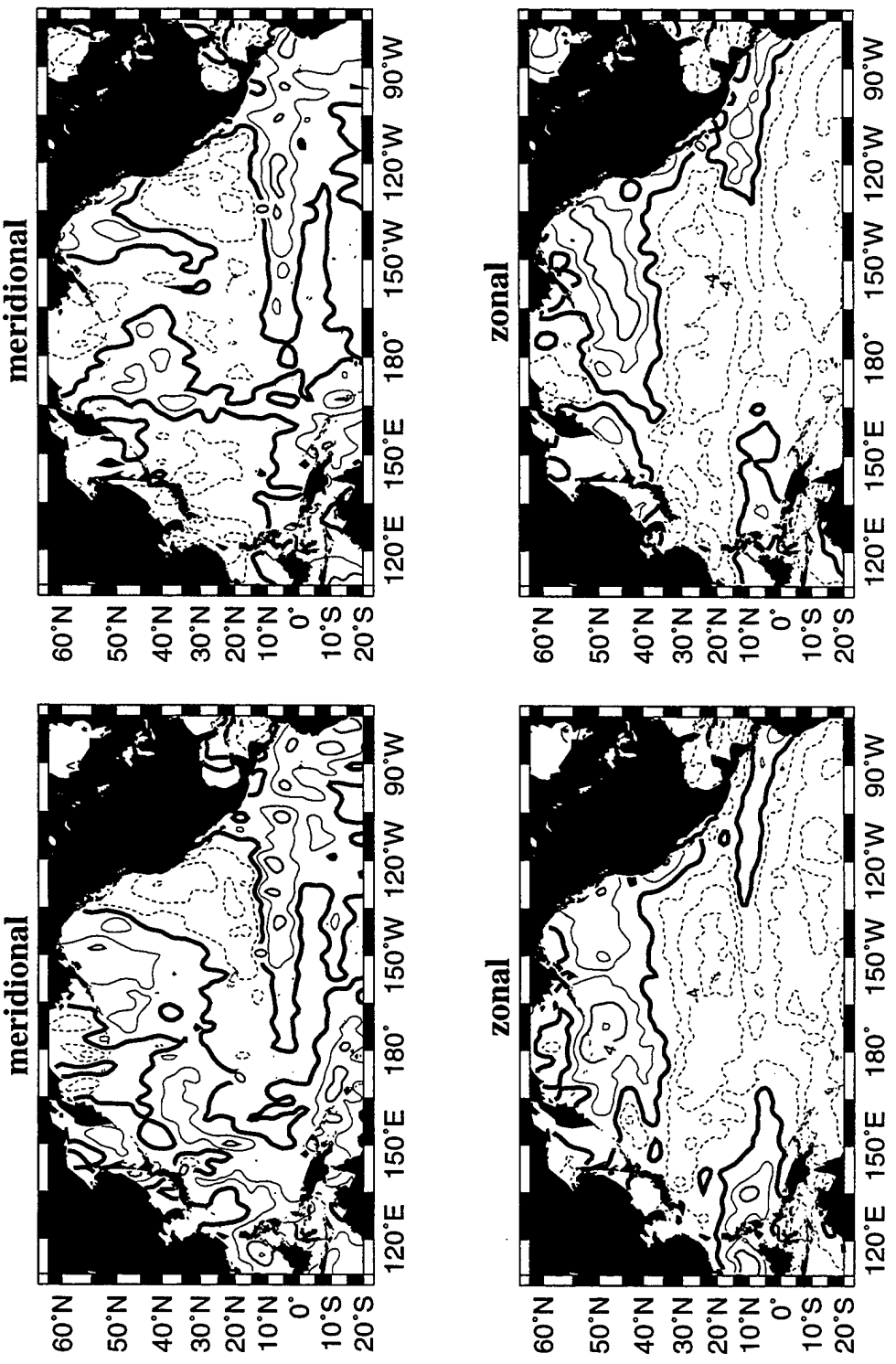

Figure 38: Wind components for August 12–September 8, 1992 (left) and September 9–October 6, 1992 (right). Contour interval is 2.0 ms^{-1} for the wind components

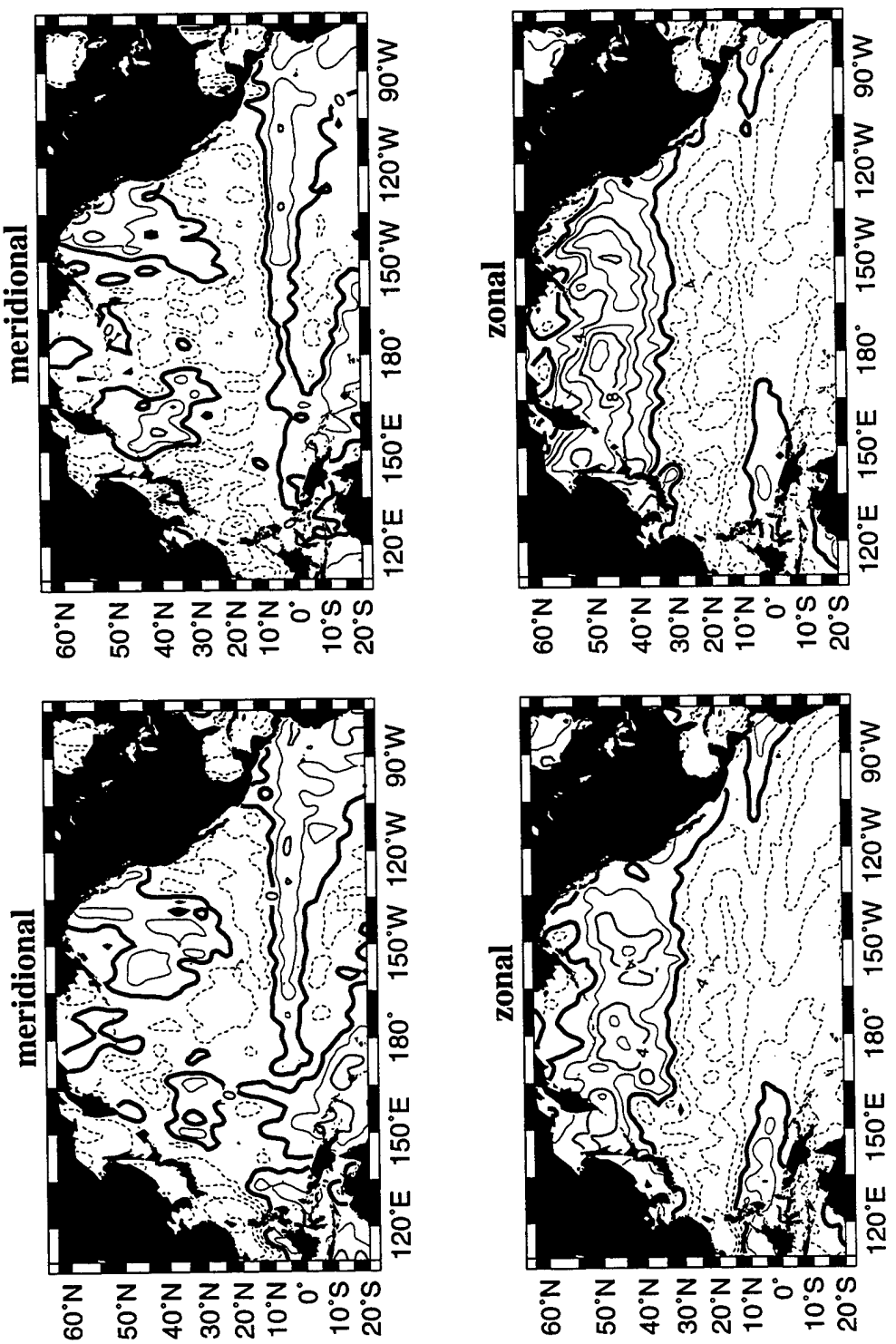

Figure 39: Wind components for October 7–November 3, 1992 (left) and November 4–December 1, 1992 (right). Contour interval is 2.0 ms^{-1} for the wind components

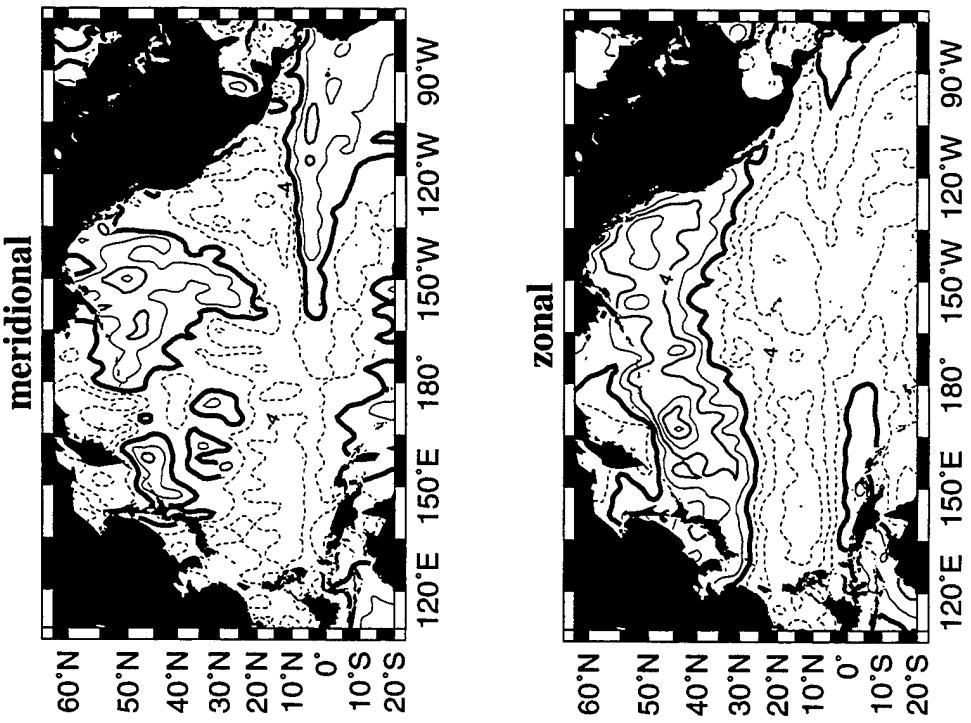

Figure 40: Wind components for December 2–December 29, 1992 (left). Contour interval is 2.0 ms^{-1} for the wind components

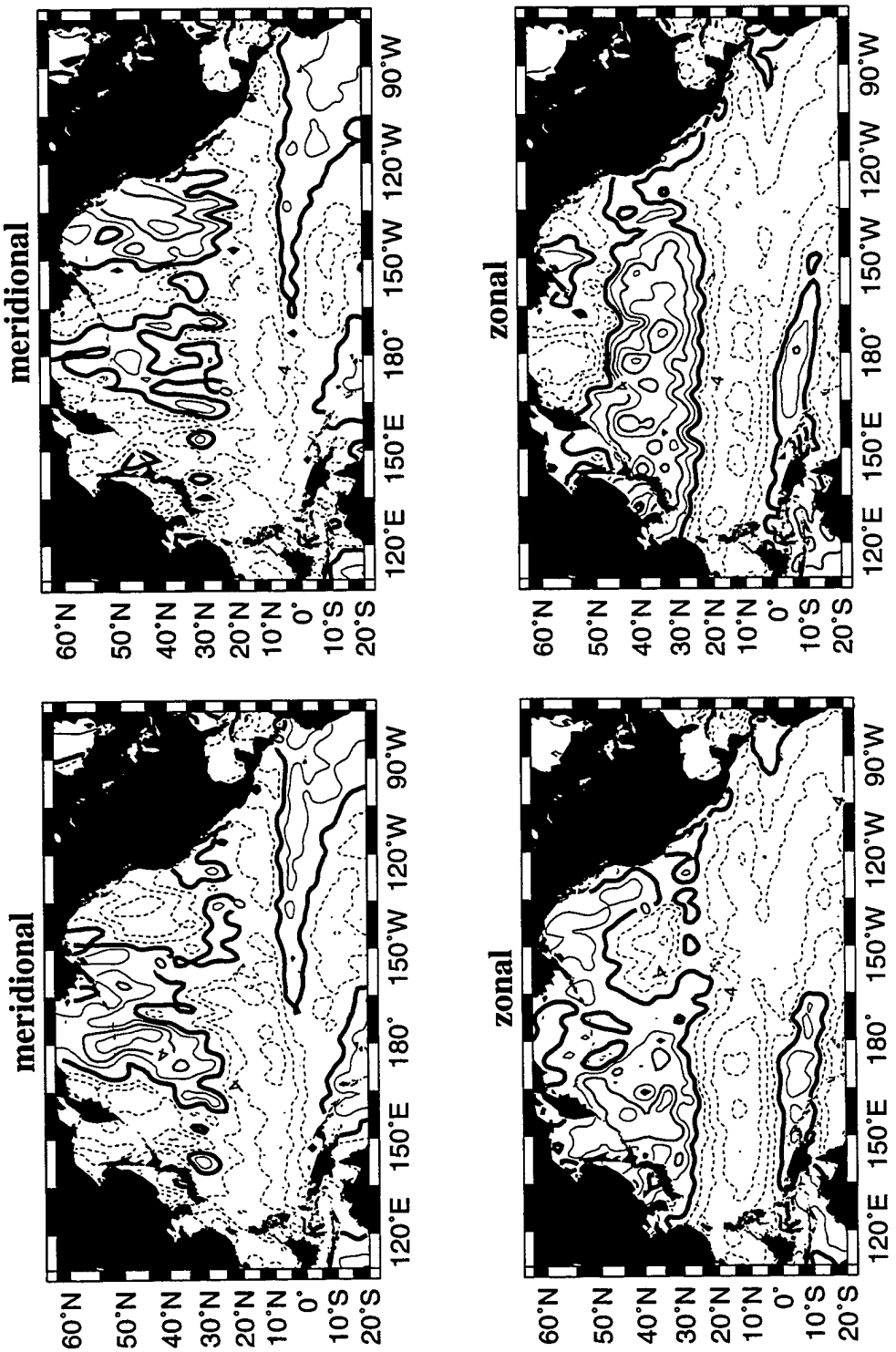

Figure 41: Wind components for December 30, 1992–January 26, 1993 (left) and January 27–February 23, 1993 (right). Contour interval is 2.0 ms^{-1} for the wind components

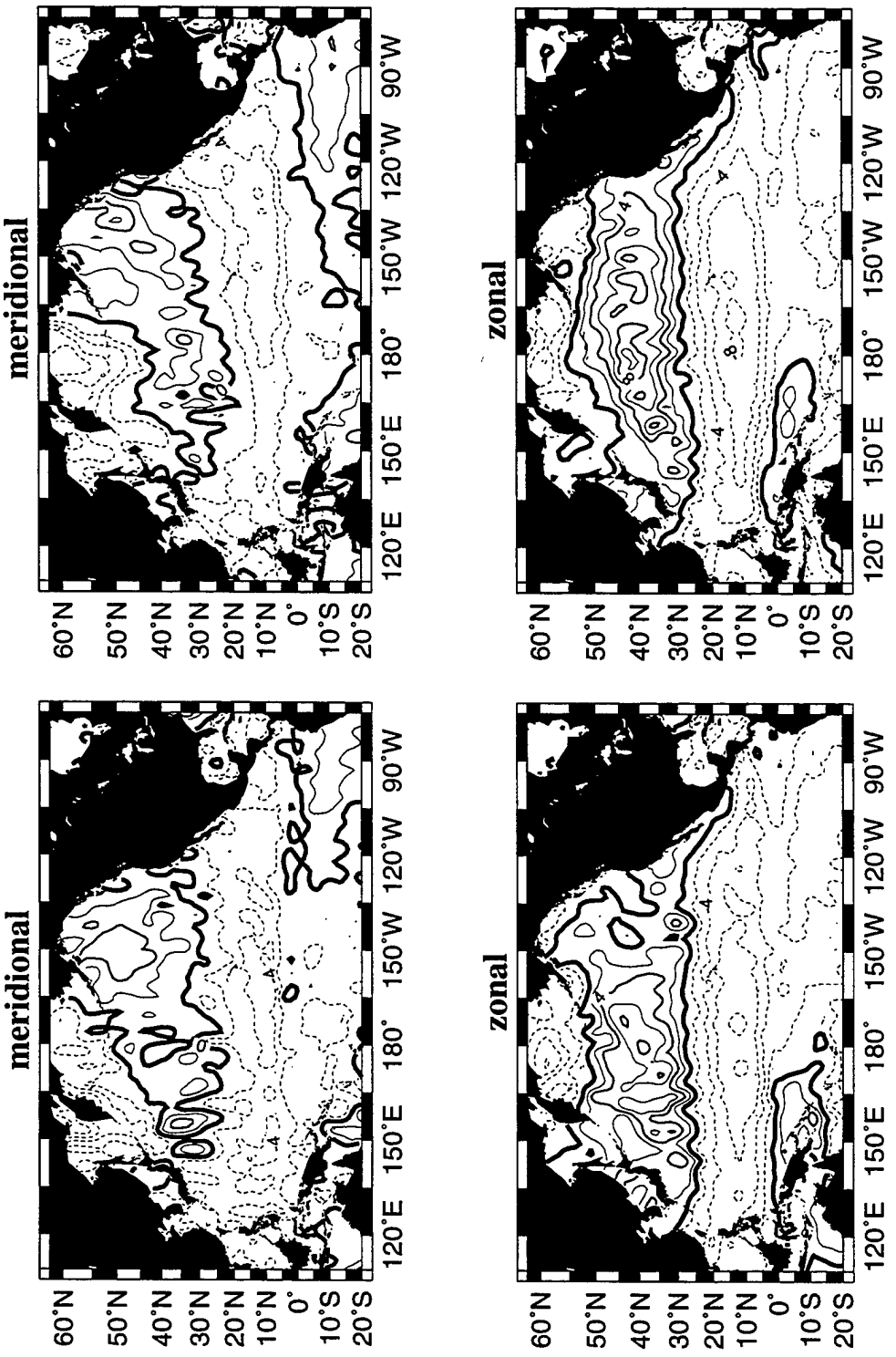

Figure 42: Wind components for February 24–March 23, 1993 (left) and March 24–April 20, 1993 (right). Contour interval is 2.0 ms^{-1} for the wind components

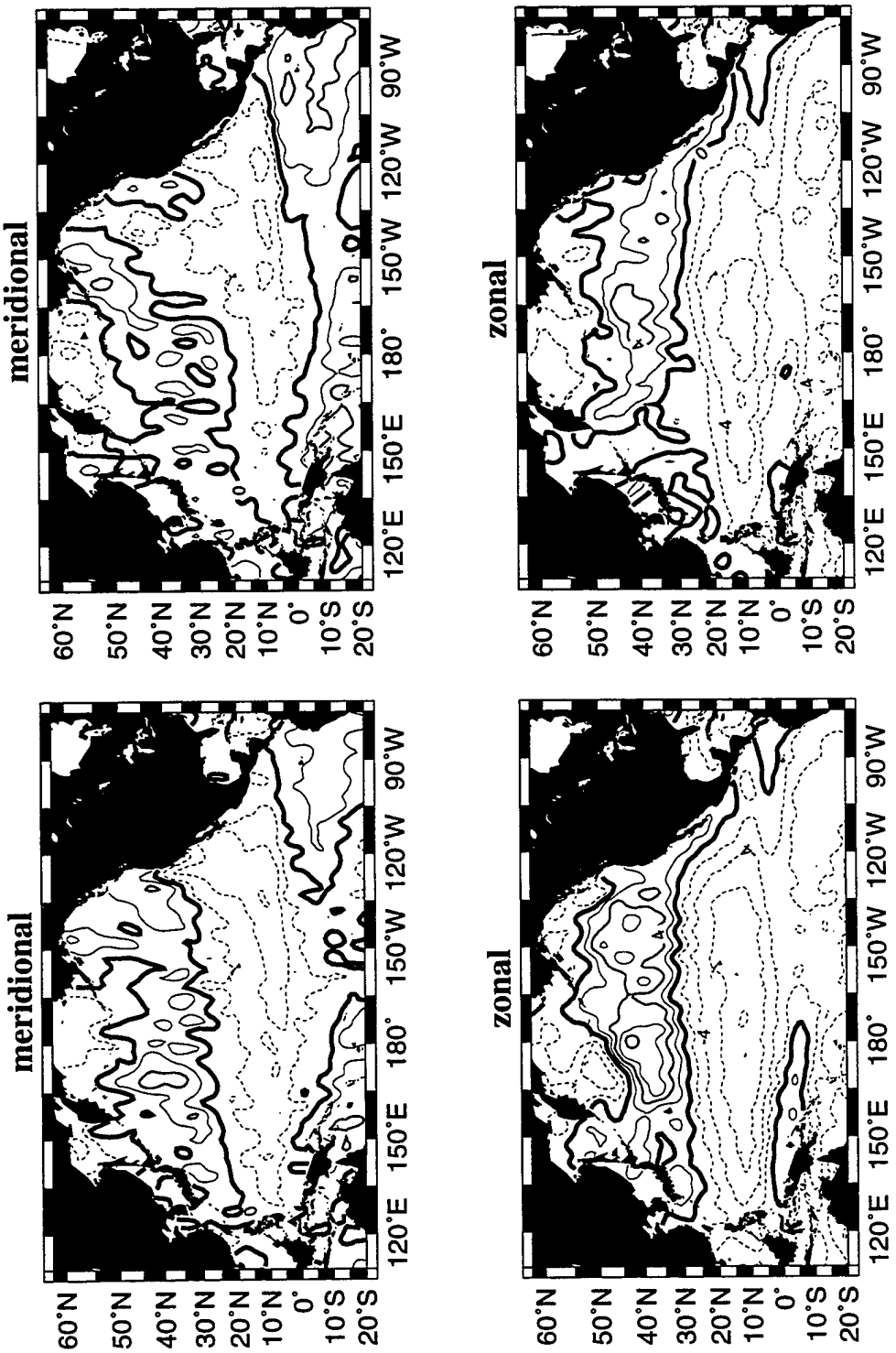

Figure 43: Wind components for April 21–May 18, 1993 (left) and May 19–June 15, 1993 (right). Contour interval is 2.0 ms^{-1} for the wind components

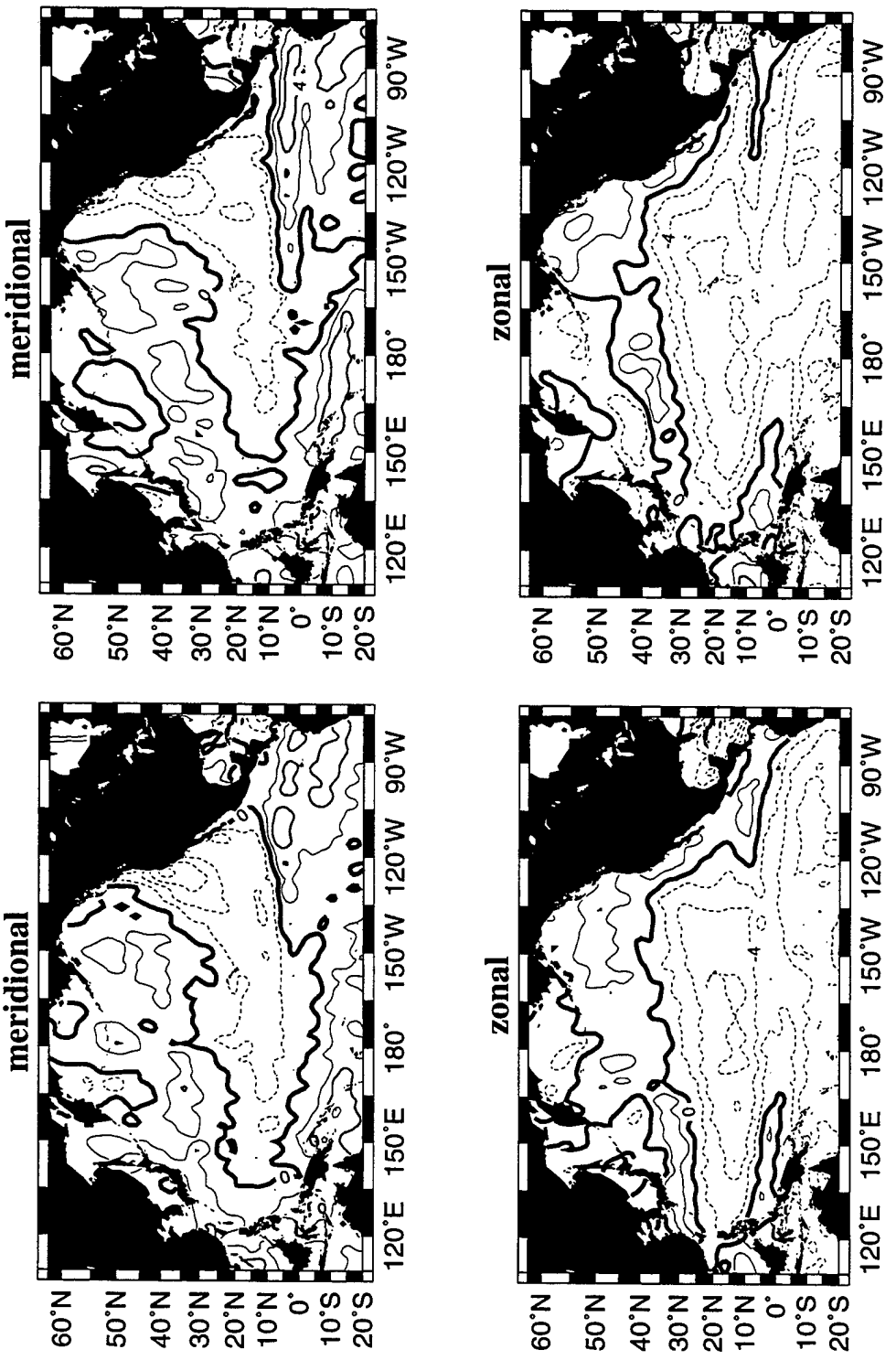

Figure 44: Wind components for June 16–July 13, 1993 (left) and July 14–August 10, 1993 (right). Contour interval is 2.0 ms^{-1} for the wind components

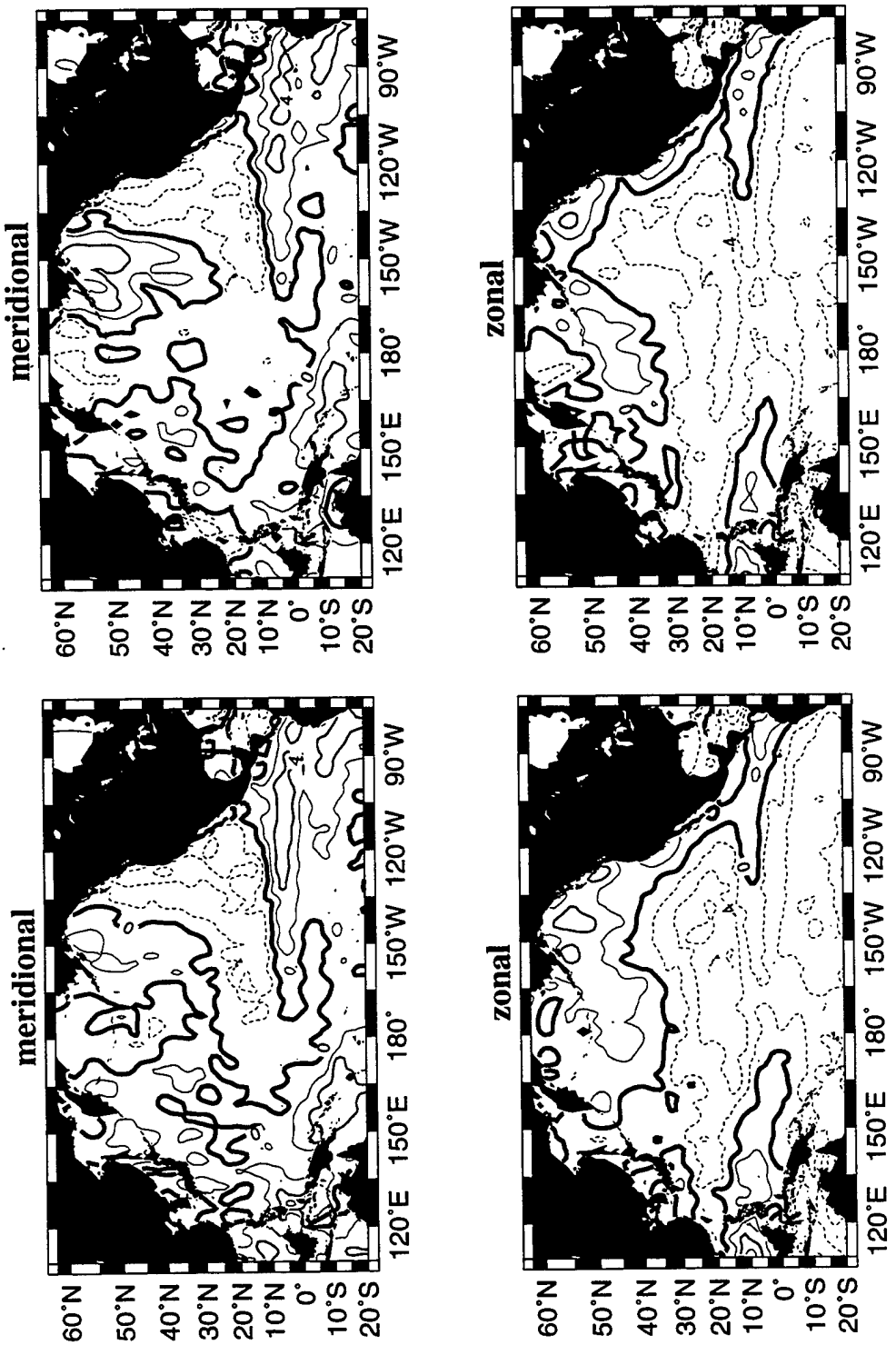

Figure 45: Wind components for August 11–September 7, 1993 (left) and September 8–October 5, 1993 (right). Contour interval is 2.0 ms^{-1} for the wind components

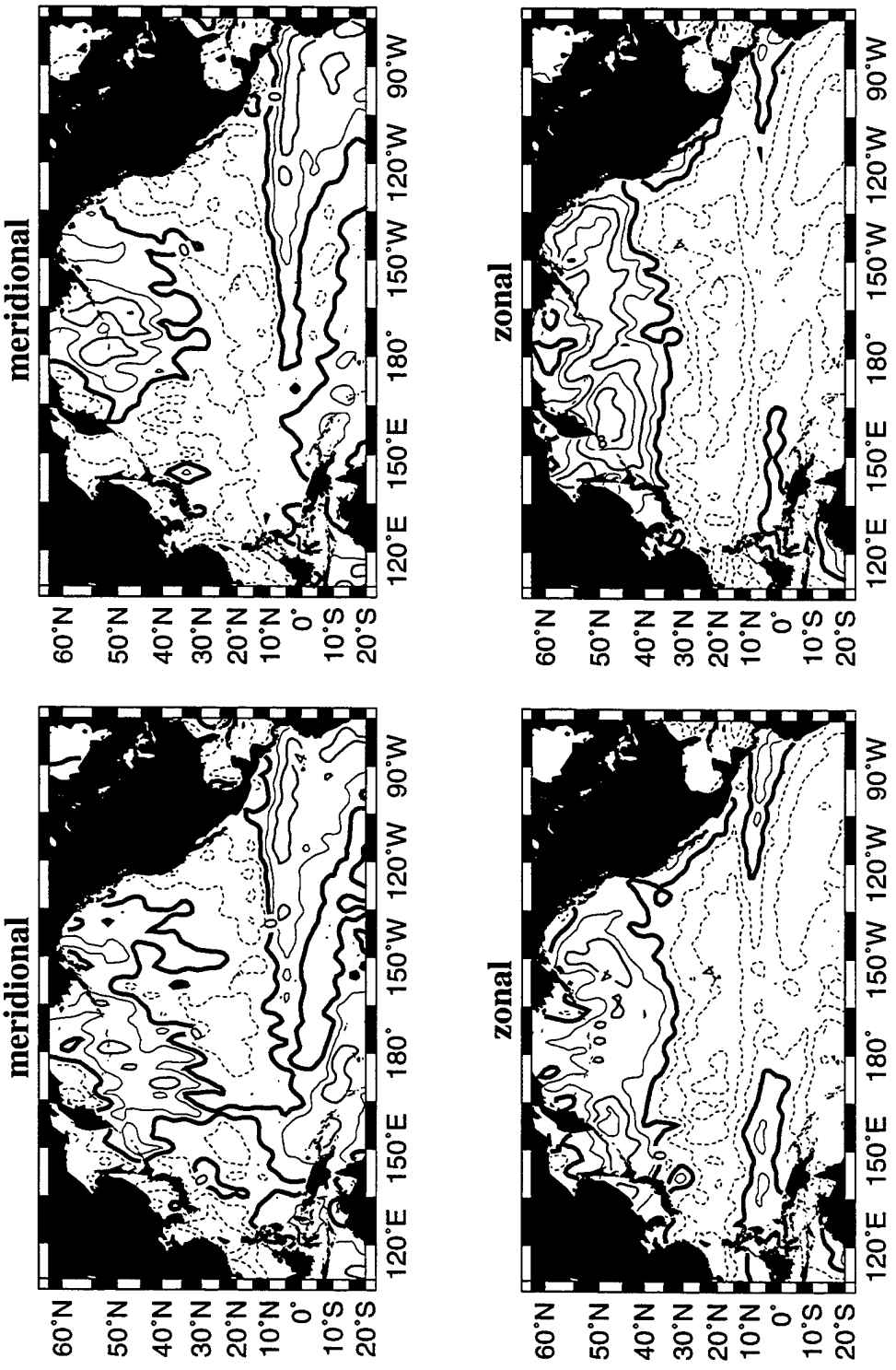

Figure 46: Wind components for October 6–November 2, 1993 (left) and November 3–November 30, 1993 (right). Contour interval is 2.0 ms^{-1} for the wind components

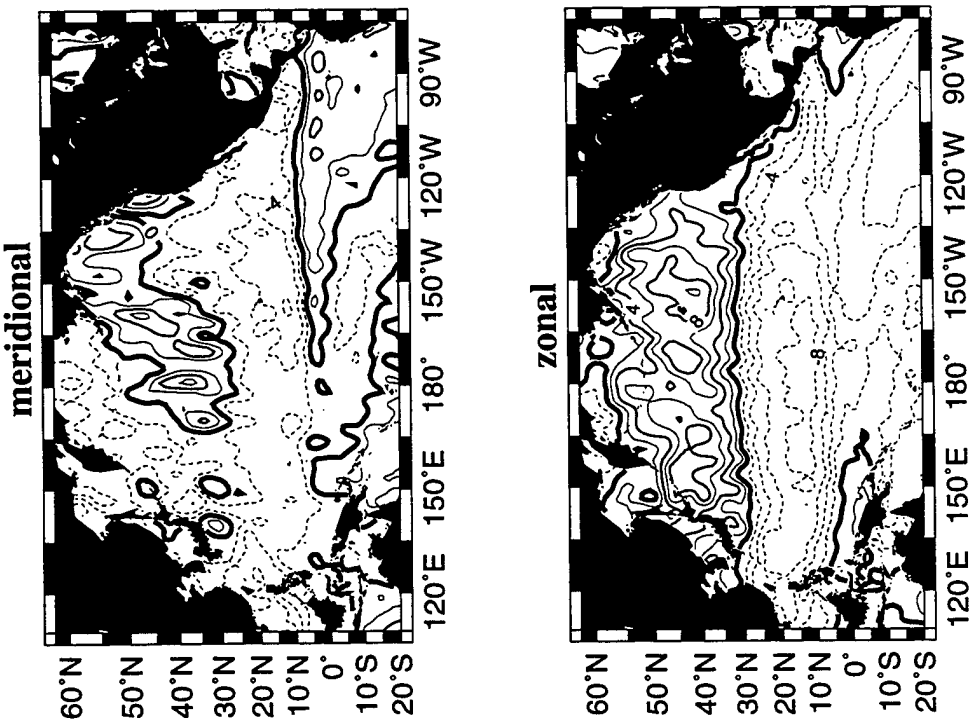

Figure 47: Wind components for December 1–December 28, 1993 (left). Contour interval is 2.0 ms^{-1} for the wind components

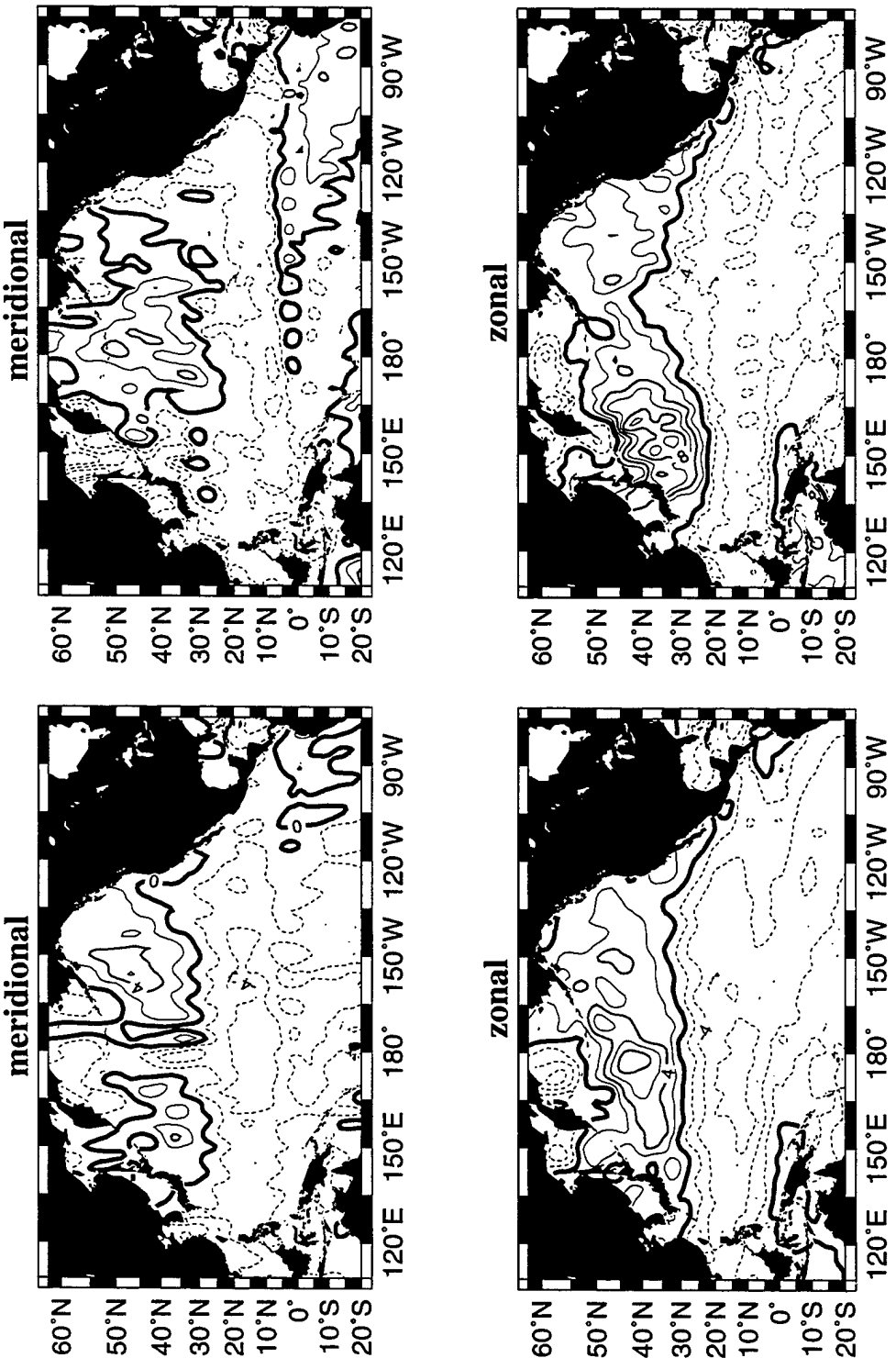

Figure 48: Wind components for December 29, 1993–January 25, 1994 (left) and January 26–February 22, 1994 (right). Contour interval is 2.0 ms^{-1} for the wind components

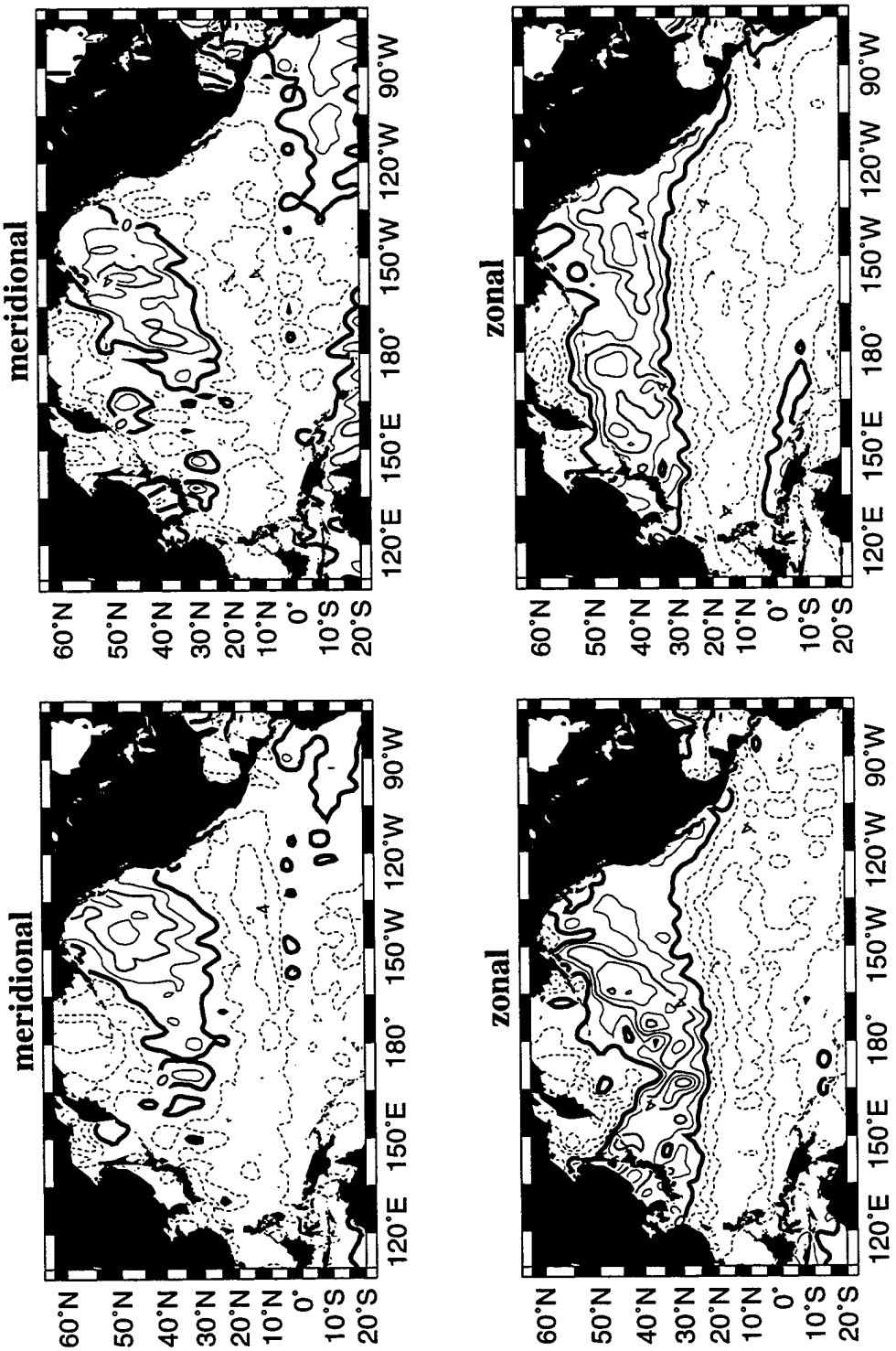

Figure 49: Wind components for February 23–March 22, 1994 (left) and March 23–April 19, 1994 (right). Contour interval is 2.0 ms^{-1} for the wind components

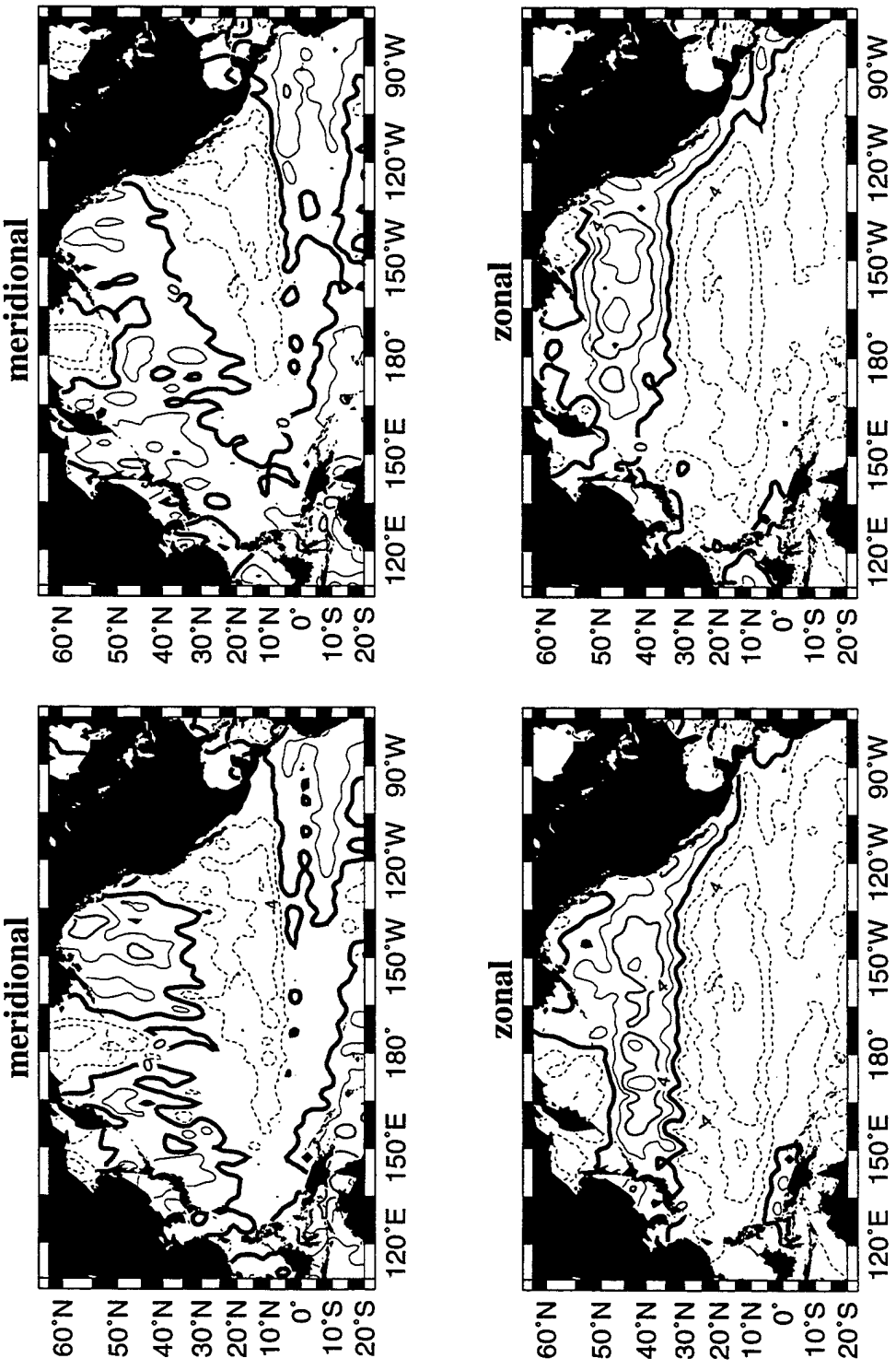

Figure 50: Wind components for April 20–May 17, 1994 (left) and May 18–June 14, 1994 (right). Contour interval is 2.0 ms^{-1} for the wind components

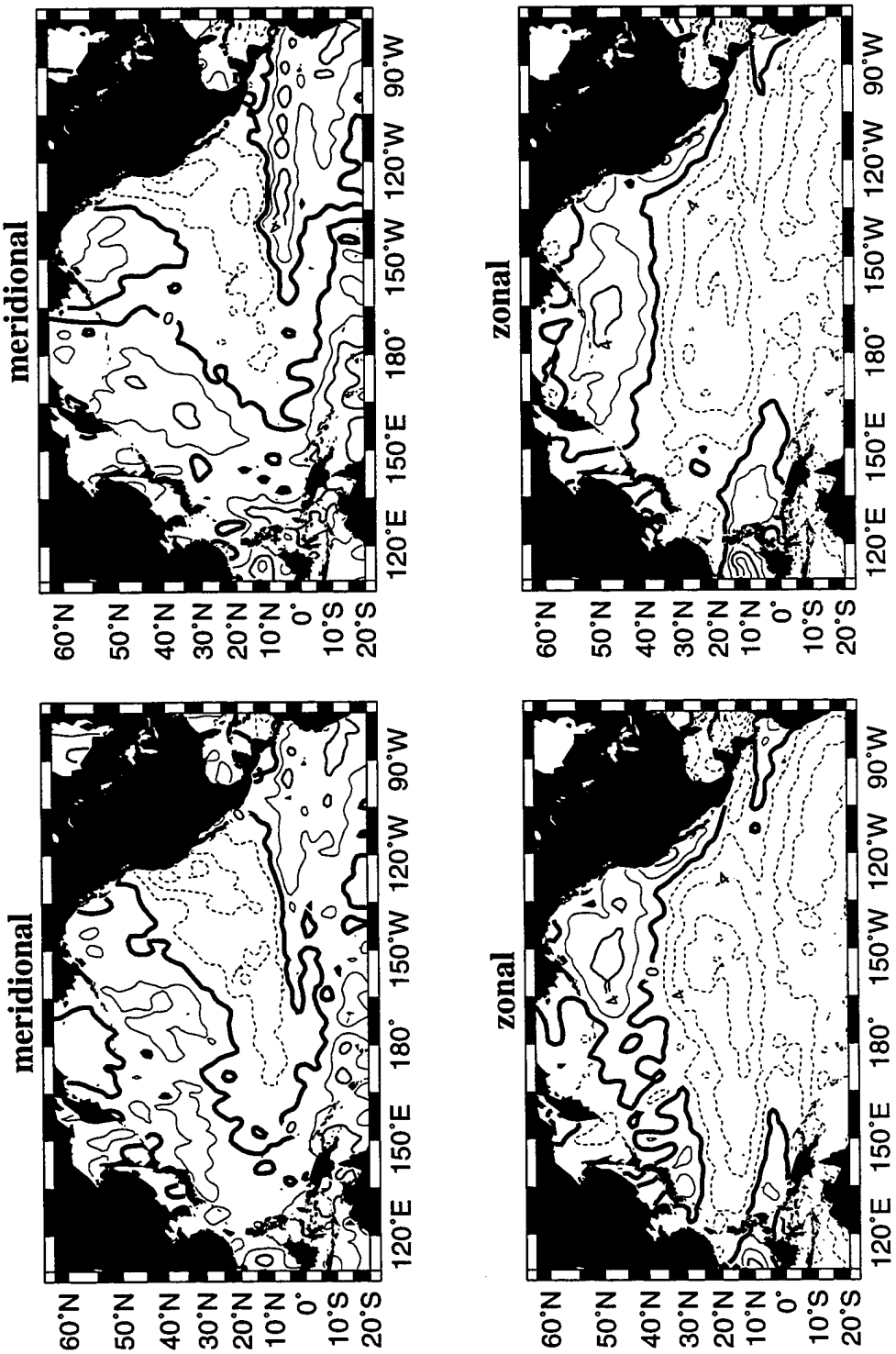

Figure 51: Wind components for June 15–July 12, 1994 (left) and July 13–August 9, 1994 (right). Contour interval is 2.0 ms^{-1} for the wind components

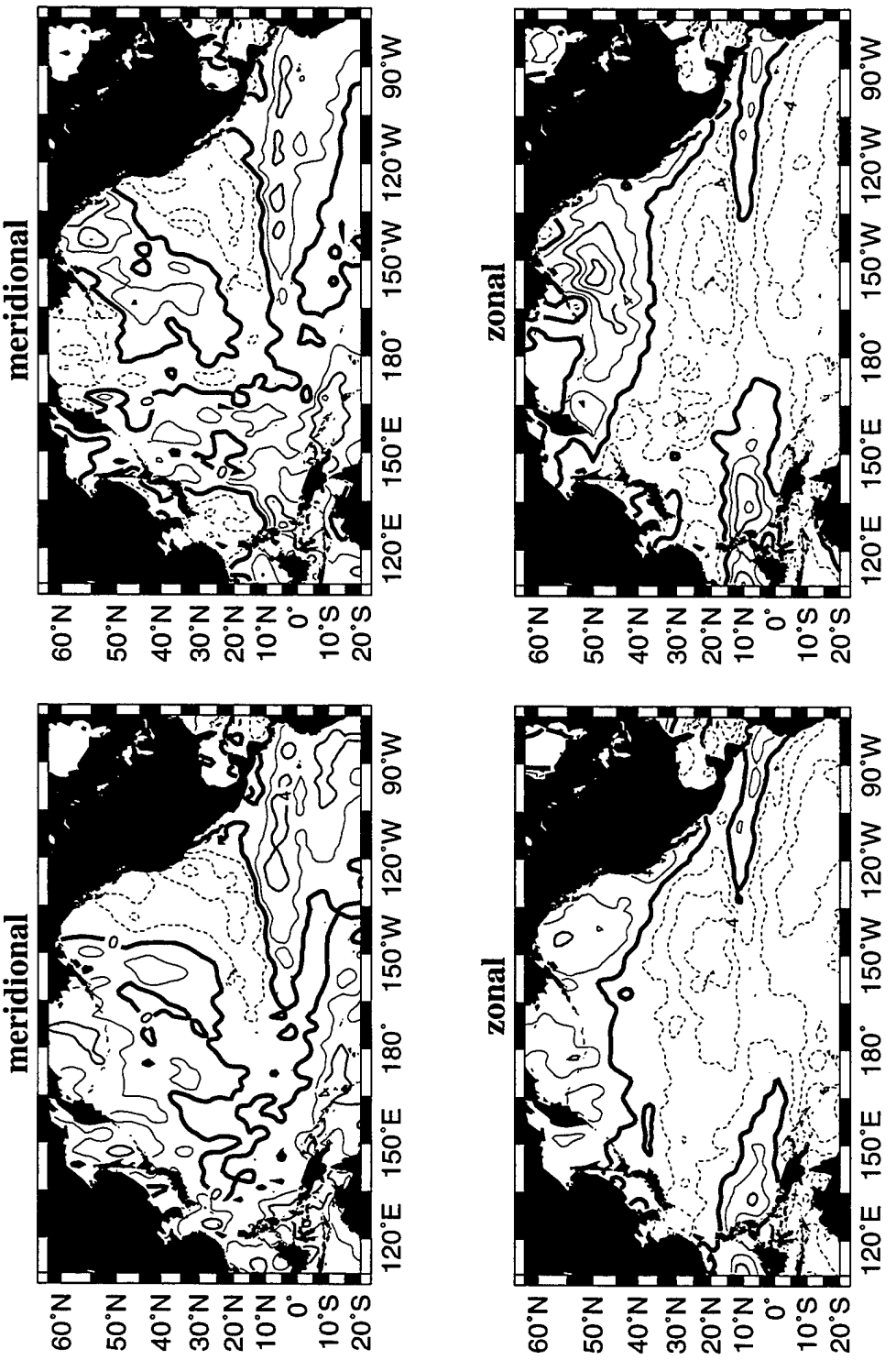

Figure 52: Wind components for August 10–September 6, 1994 (left) and September 7–October 4, 1994 (right). Contour interval is 2.0 ms^{-1} for the wind components

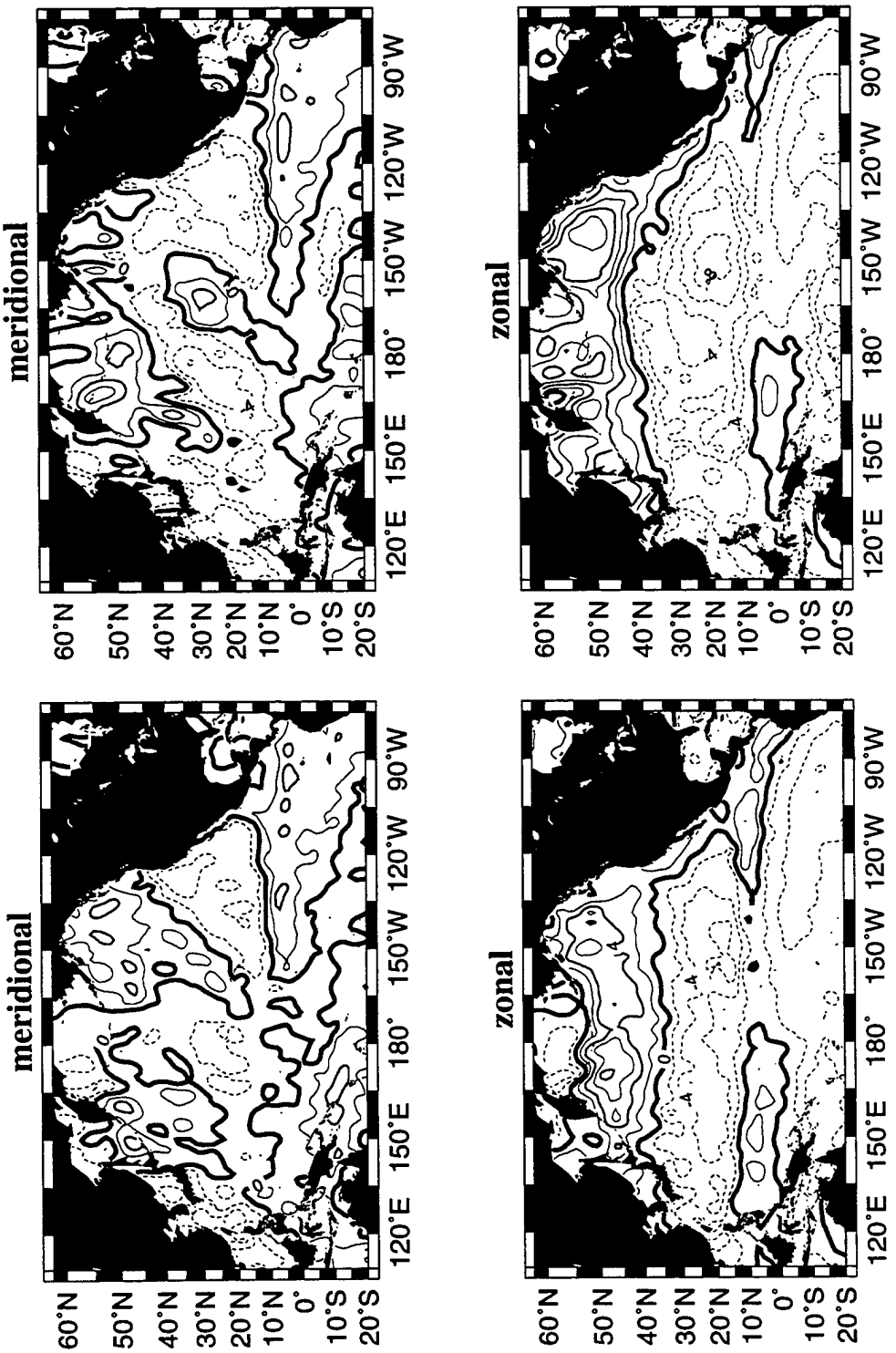

Figure 53: Wind components for October 5–November 1, 1994 (left) and November 2–November 29, 1994 (right). Contour interval is 2.0 ms^{-1} for the wind components

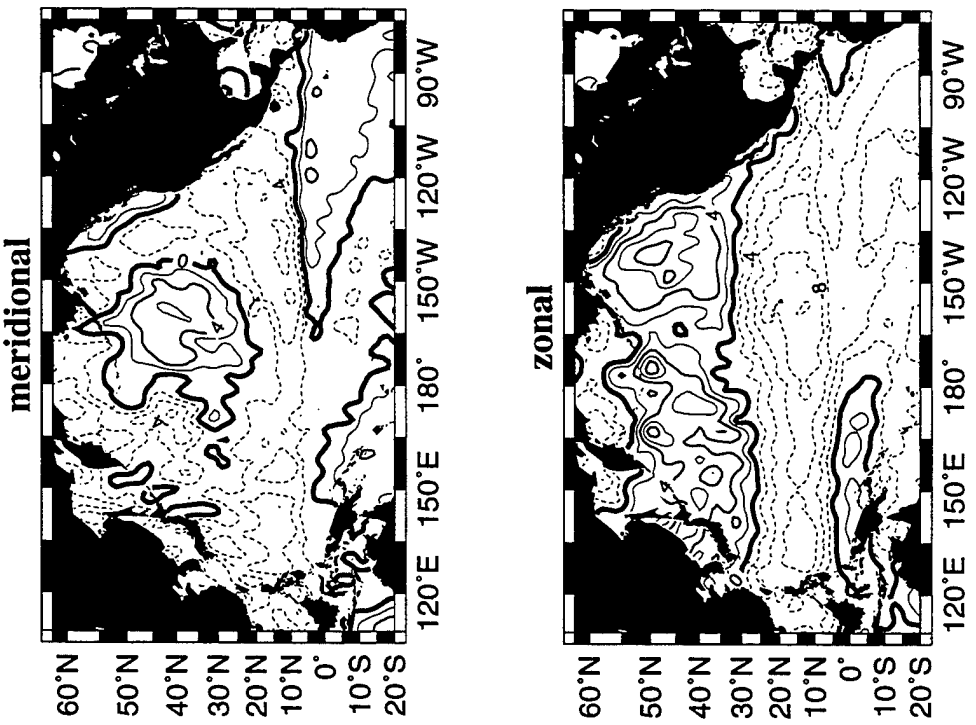

Figure 54: Wind components for November 30–December 27, 1994 (left). Contour interval is 2.0 ms^{-1} for the wind components

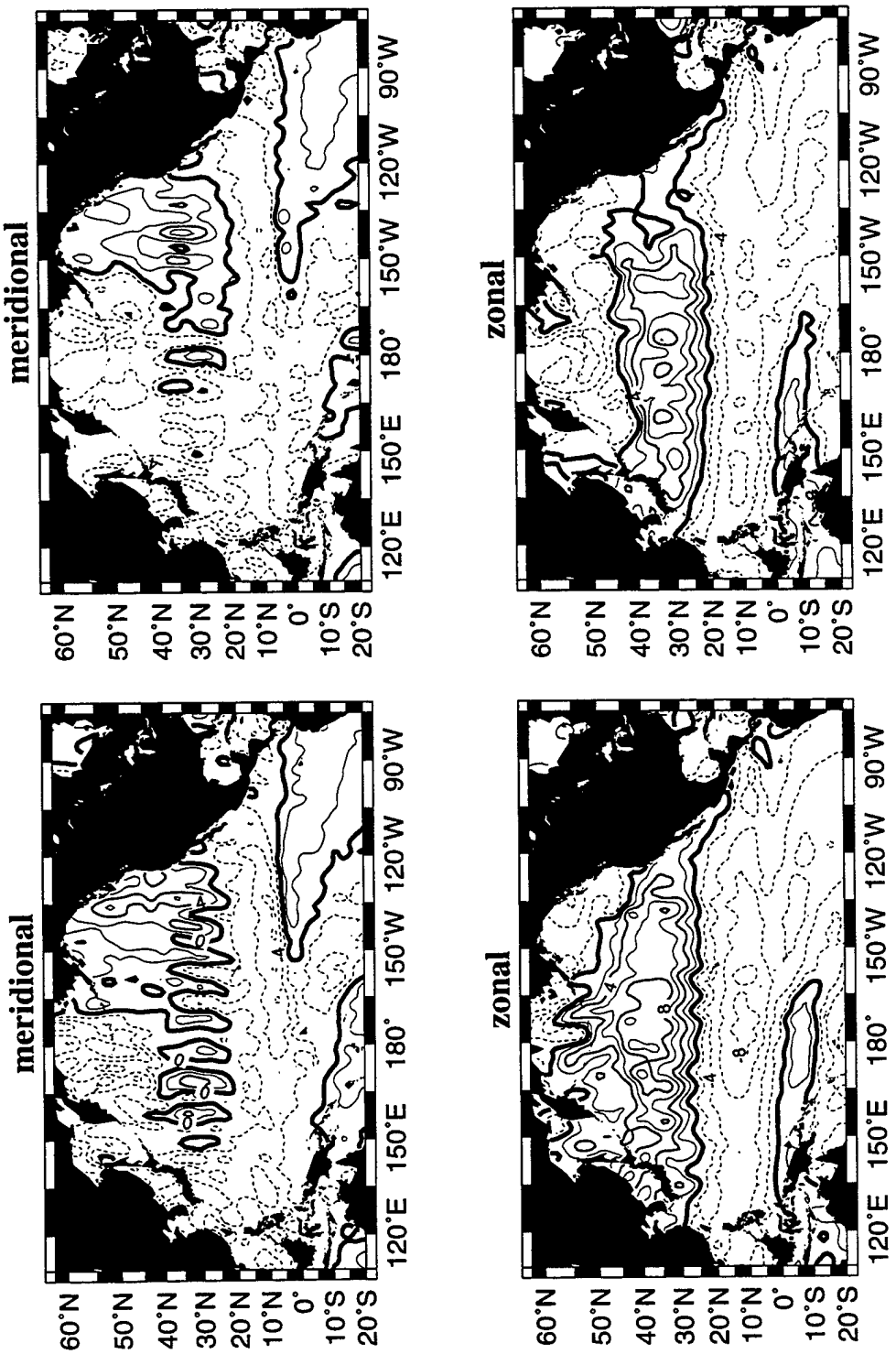

Figure 55: Wind components for December 28, 1994–January 24, 1995 (left) and January 25–February 21, 1995 (right). Contour interval is 2.0 ms^{-1} for the wind components

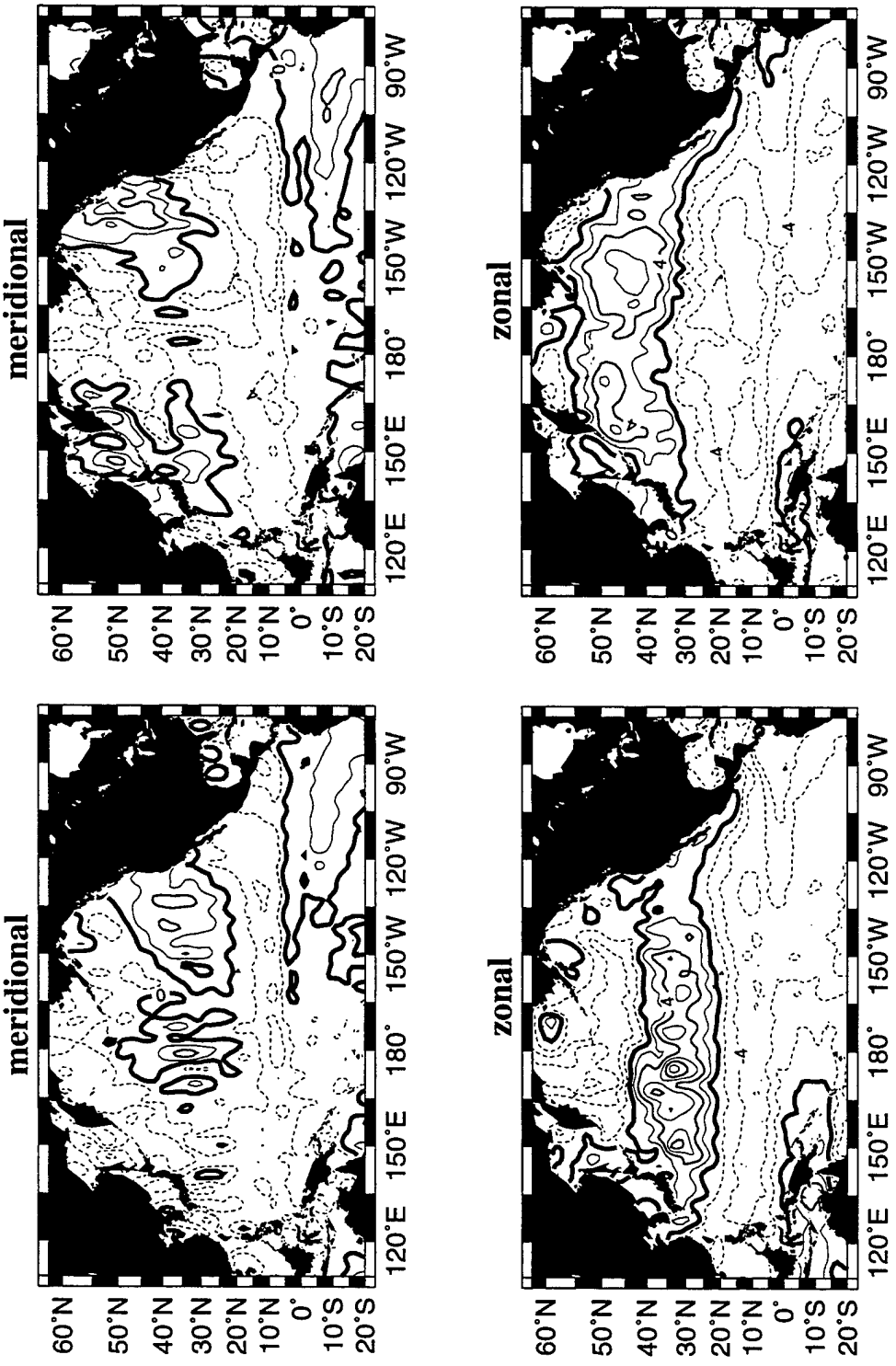

Figure 56: Wind components for February 22–March 21, 1995 (left) and March 22–April 18, 1995 (right). Contour interval is 2.0 ms^{-1} for the wind components

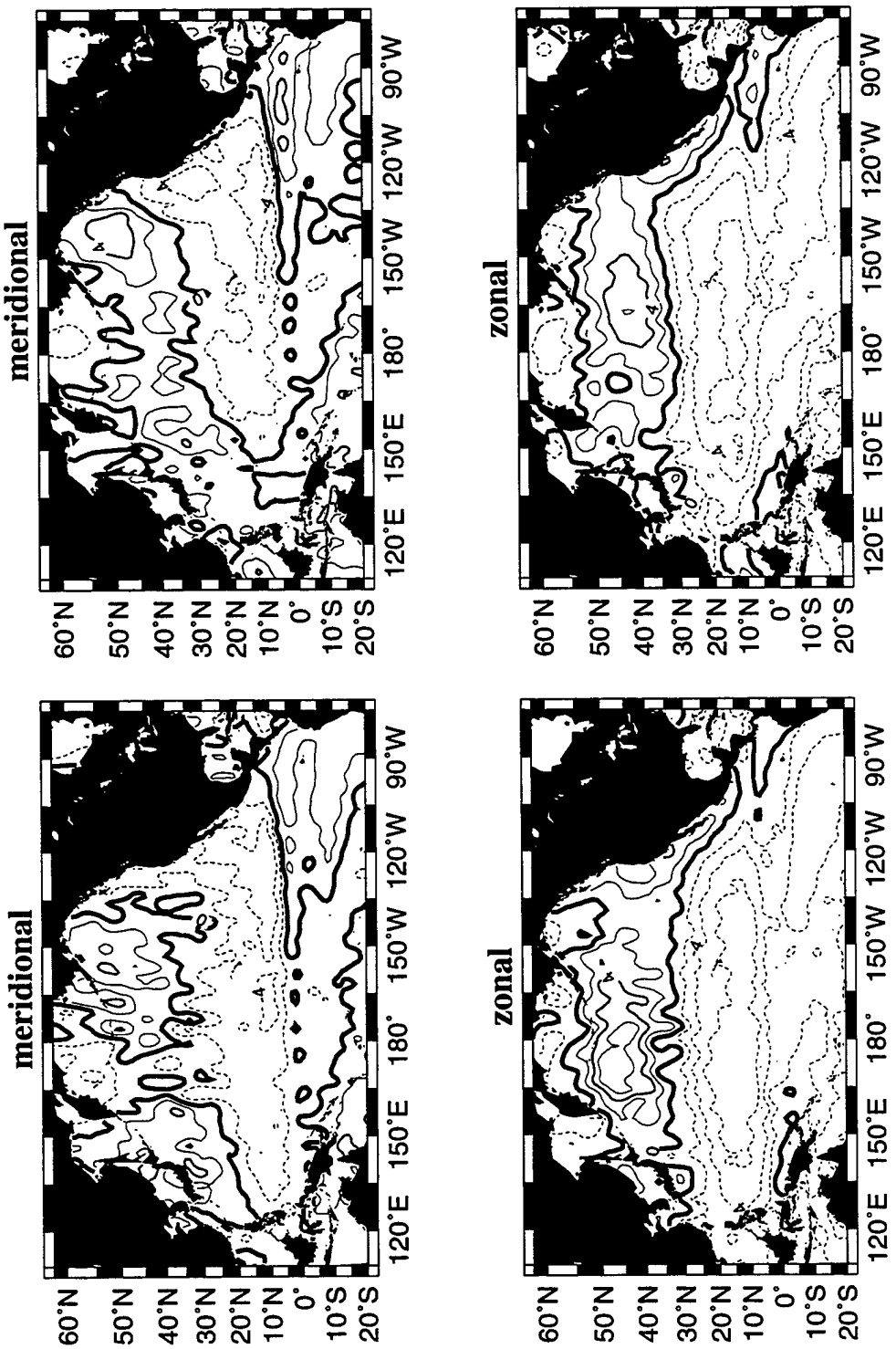

Figure 57: Wind components for April 19–May 16, 1995 (left) and May 17–June 13, 1995 (right). Contour interval is 2.0 ms^{-1} for the wind components

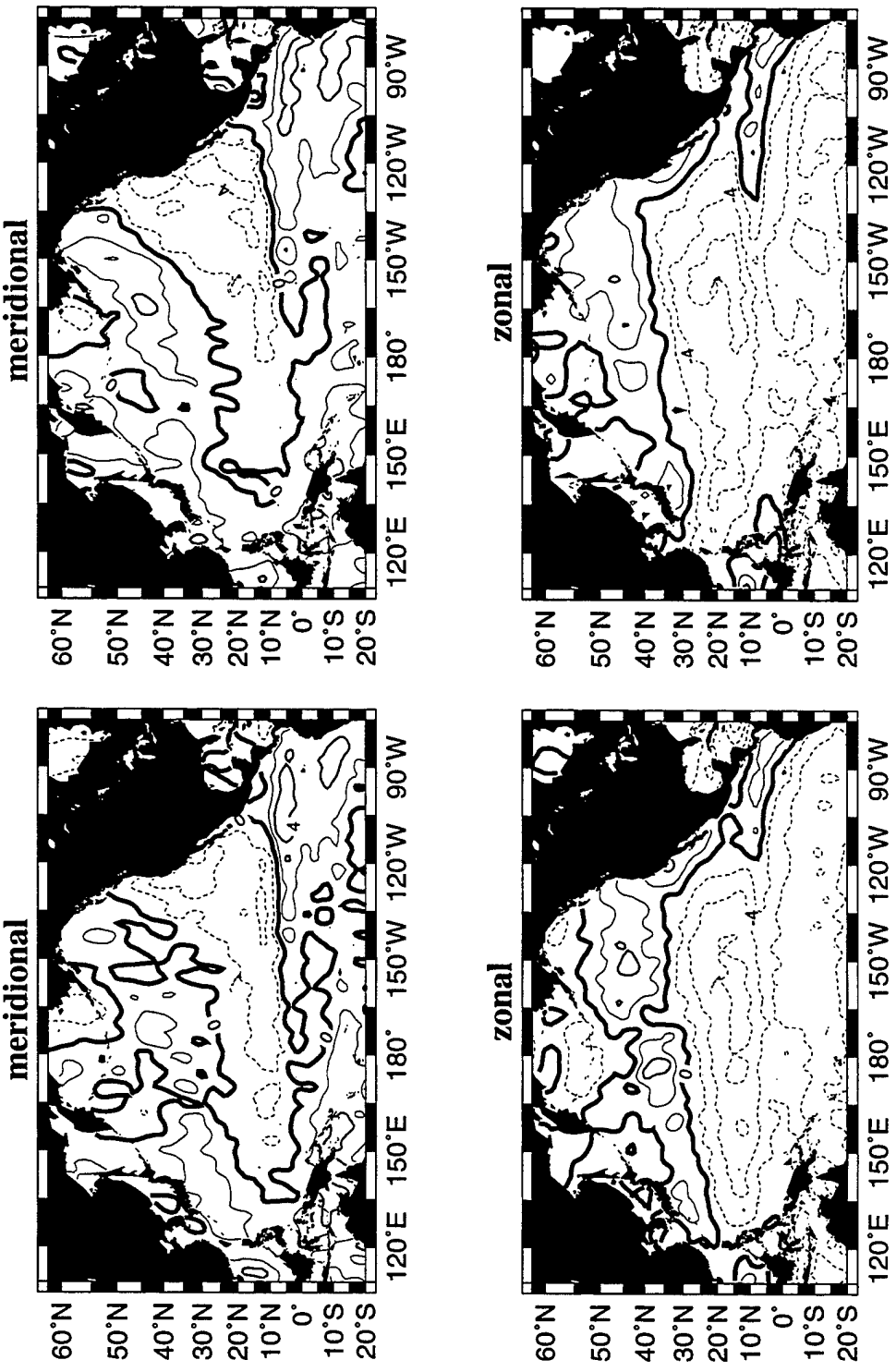

Figure 58: Wind components for June 14–July 11, 1995 (left) and July 12–August 8, 1995 (right). Contour interval is 2.0 ms^{-1} for the wind components

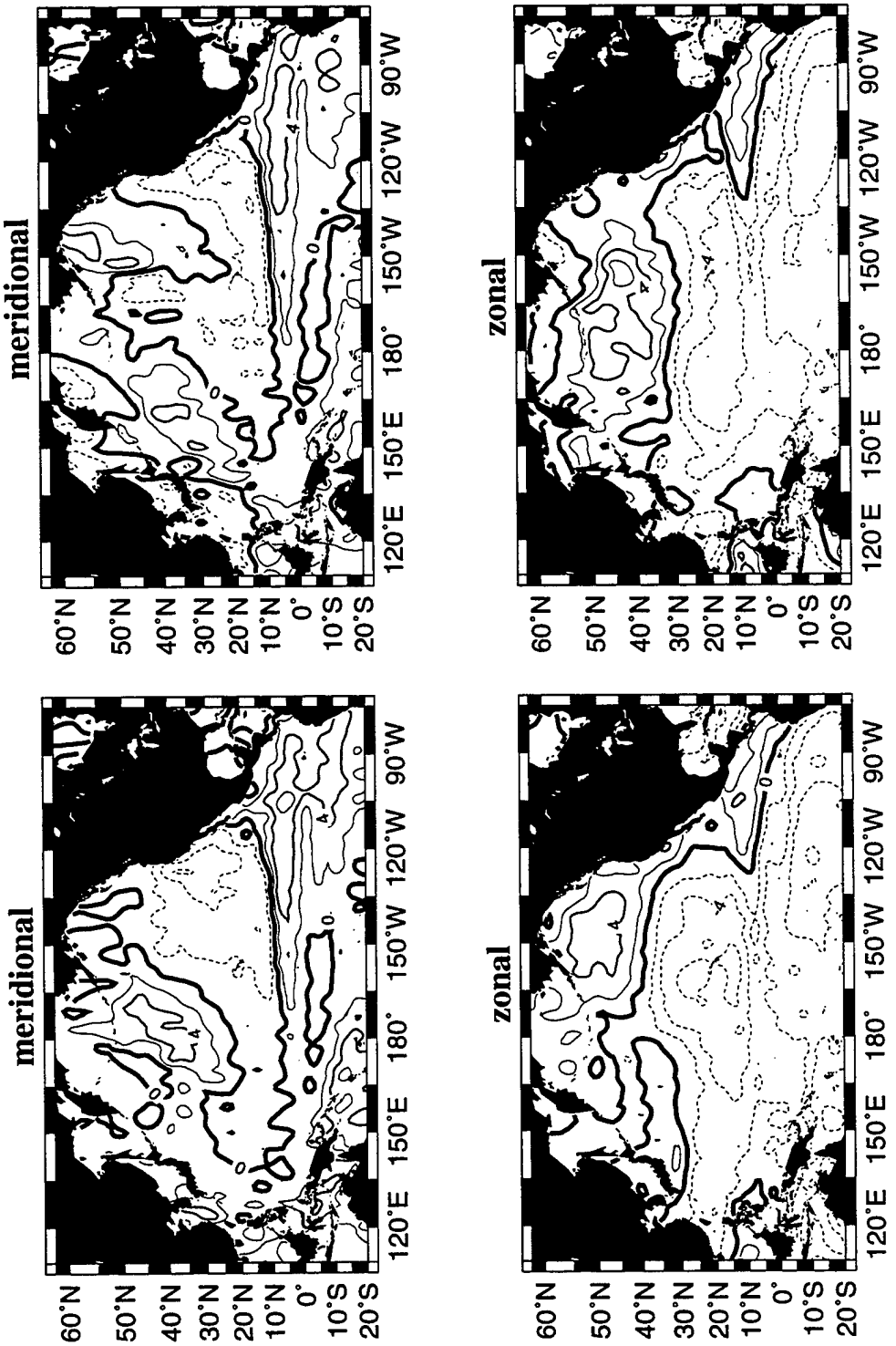

Figure 59: Wind components for August 9–September 5, 1995 (left) and September 6–October 3, 1995 (right). Contour interval is 2.0 ms^{-1} for the wind components

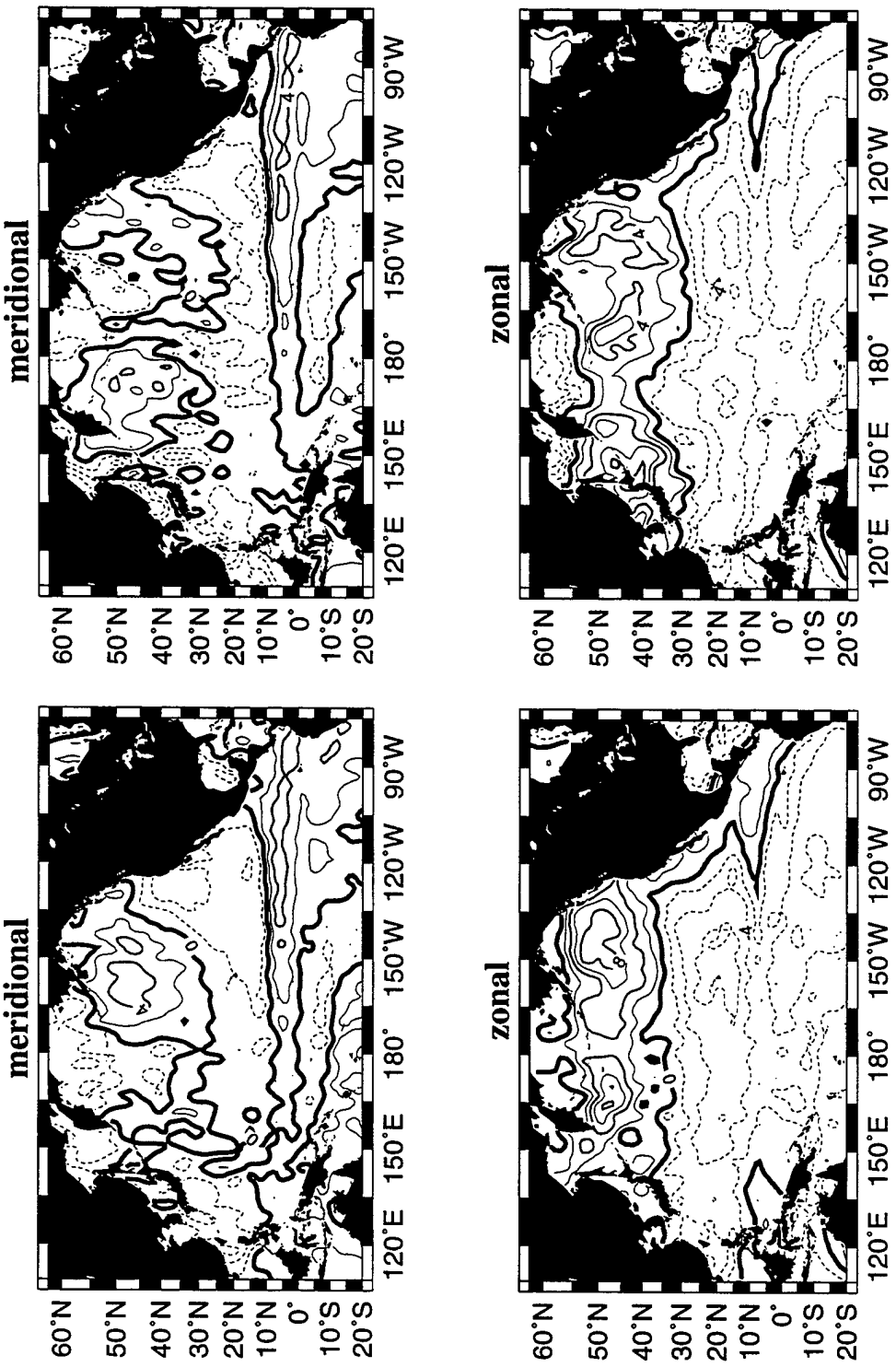

Figure 60: Wind components for October 4–October 31, 1995 (left) and November 1–November 28, 1995 (right). Contour interval is 2.0 ms^{-1} for the wind components

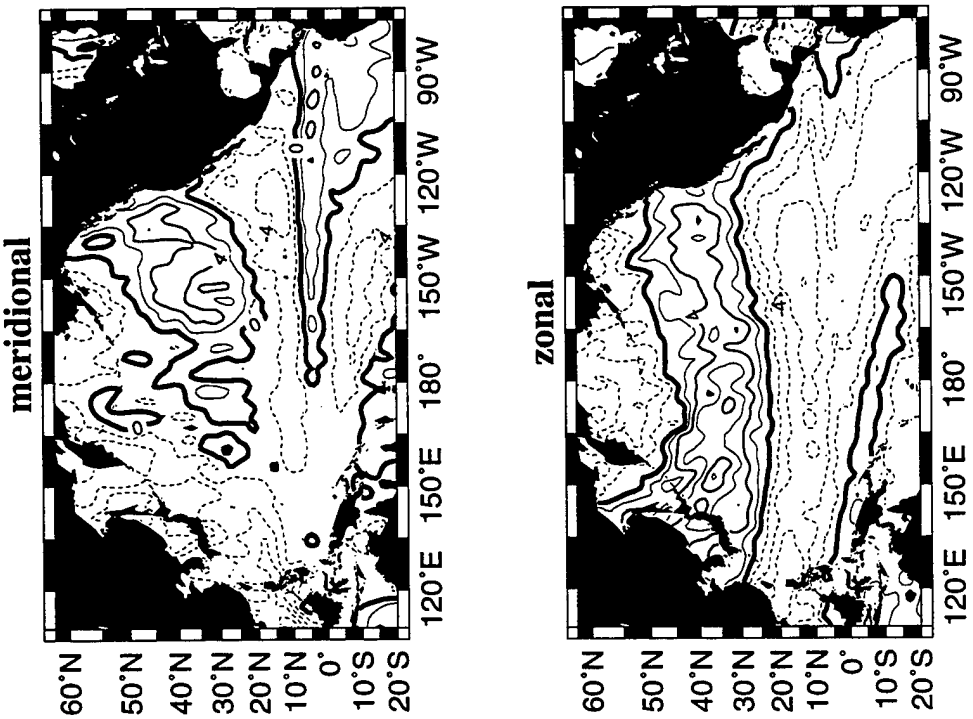

Figure 61: Wind components for November 29–December 26, 1995 (left). Contour interval is 2.0 ms^{-1} for the wind components

Northeast Pacific wind vectors

Section C has vector plots of the winds over the Northeast Pacific from 25°–50° N, 210°–240° E. Figures 62 and 63 show examples of biweekly wind vectors from each year for the beginning of July and the end of September respectively. Figures 64–79 show the complete series of wind vectors. A complete list of the monthly averaging intervals is given in Table 8.

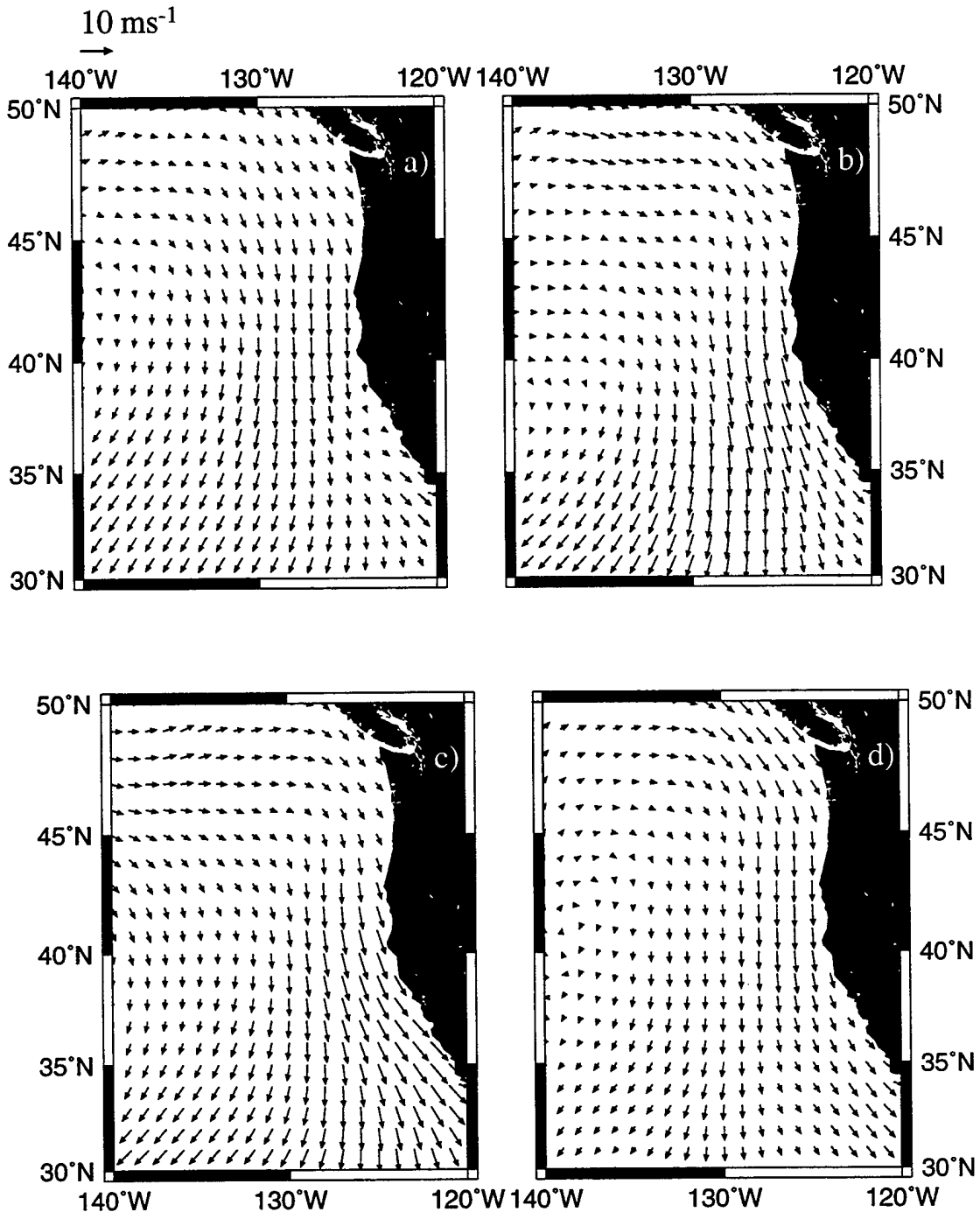

Figure 62: Wind vectors for a) July 1–July 14, 1992; b) June 30–July 13, 1993; c) June 29–July 12, 1994 and d) June 28–July 11, 1995.

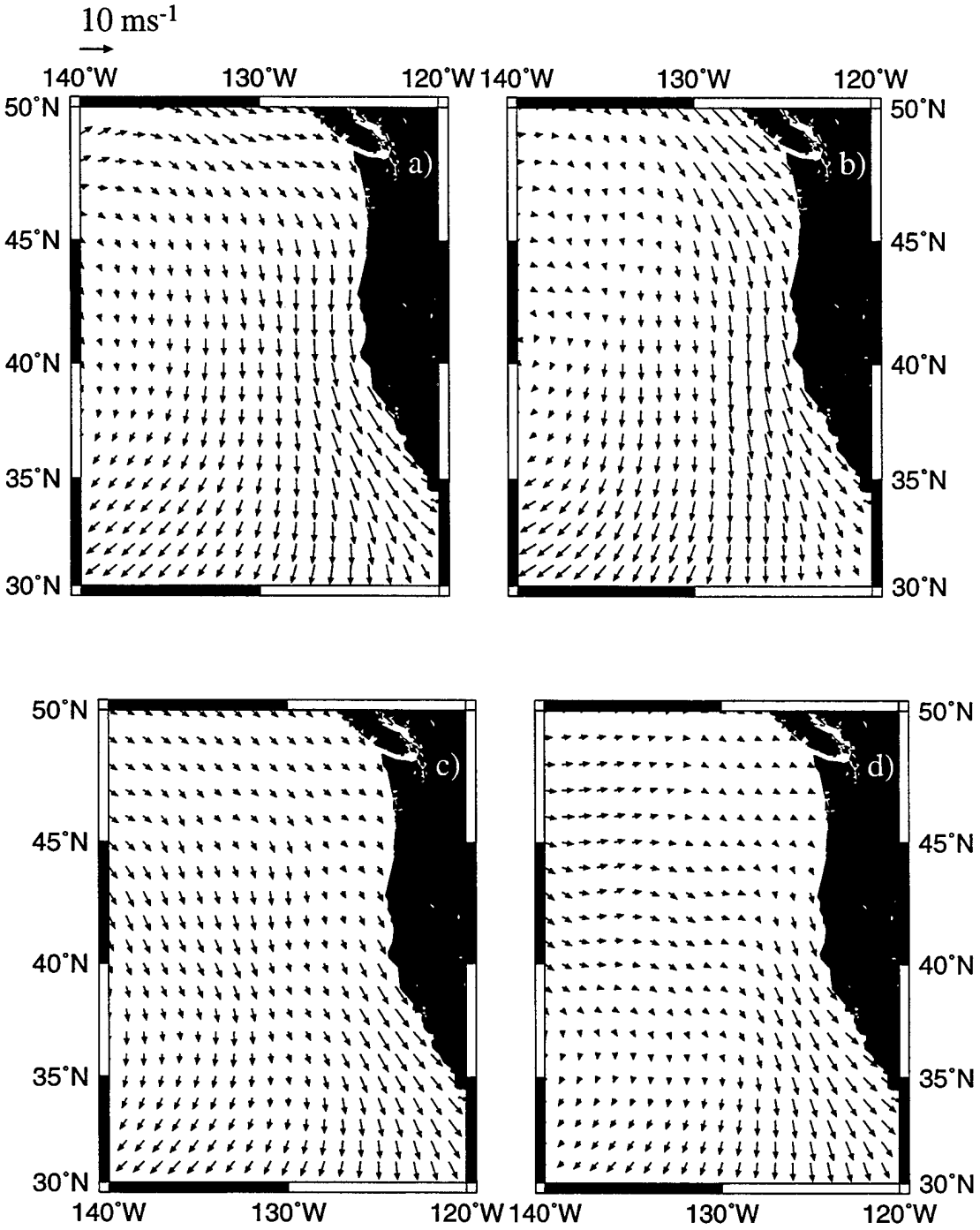

Figure 63: Wind vectors for a) August 26–September 8, 1992; b) August 25–September 7, 1993; c) August 24–September 6, 1994 and d) August 23–September 5, 1995.

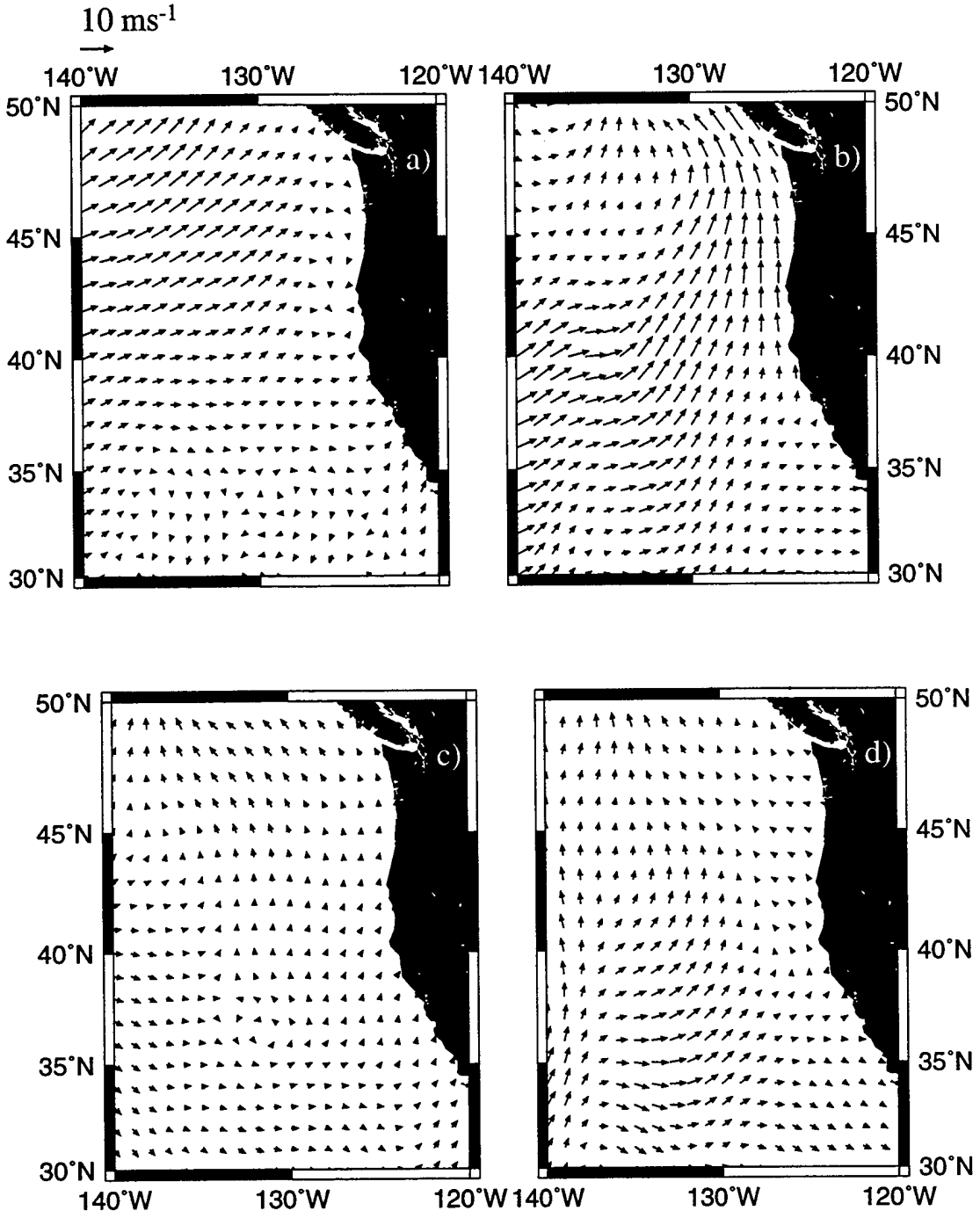

Figure 64: Wind vectors for a) January 1–January 28, 1992; b) January 29–February 25, 1992; c) February 26–March 24, 1992 and d) March 25–April 21, 1992.

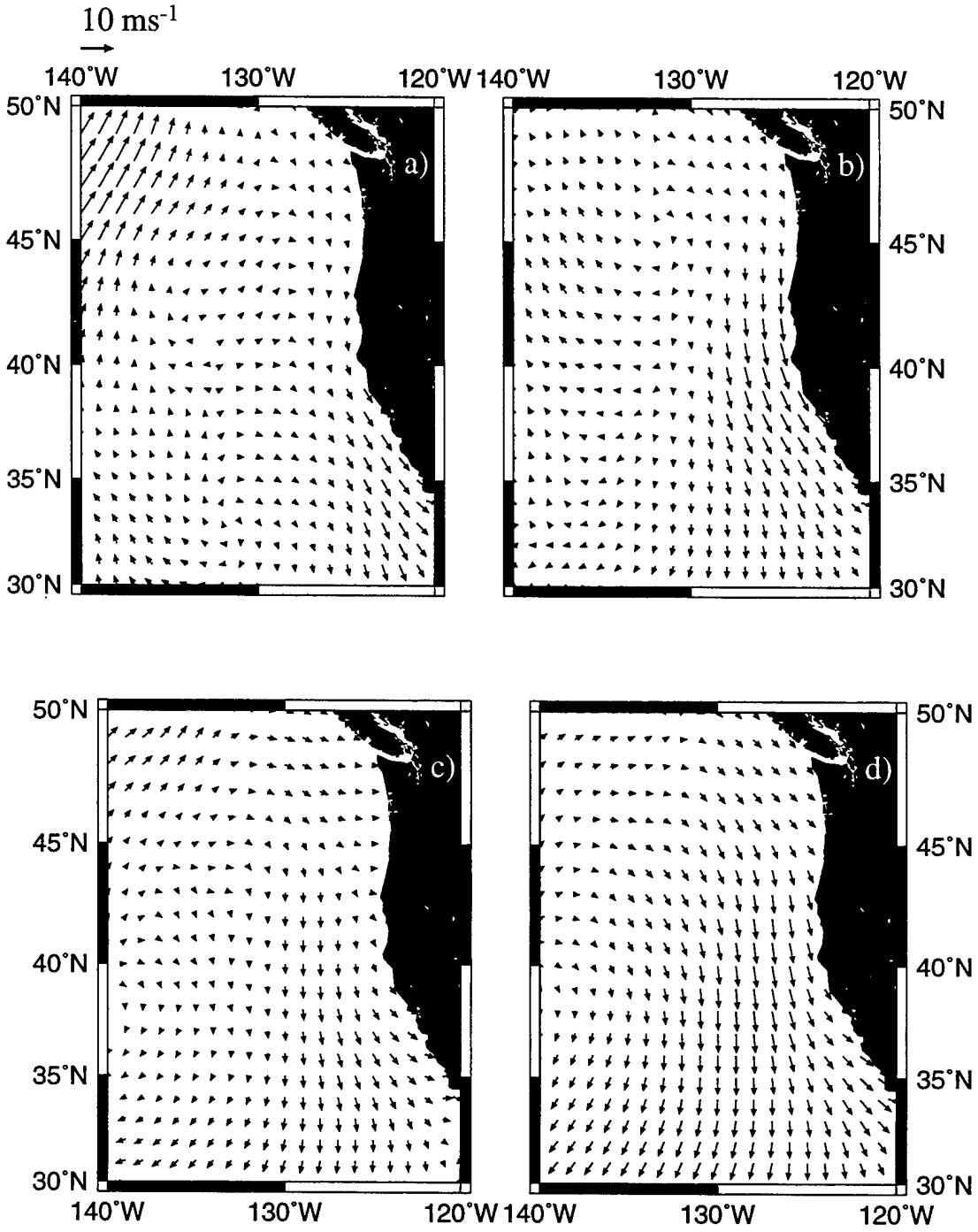

Figure 65: Wind vectors for a) April 22–May 19, 1992; b) May 20–June 16, 1992; c) June 17–July 14, 1992 and d) July 15–August 11, 1992.

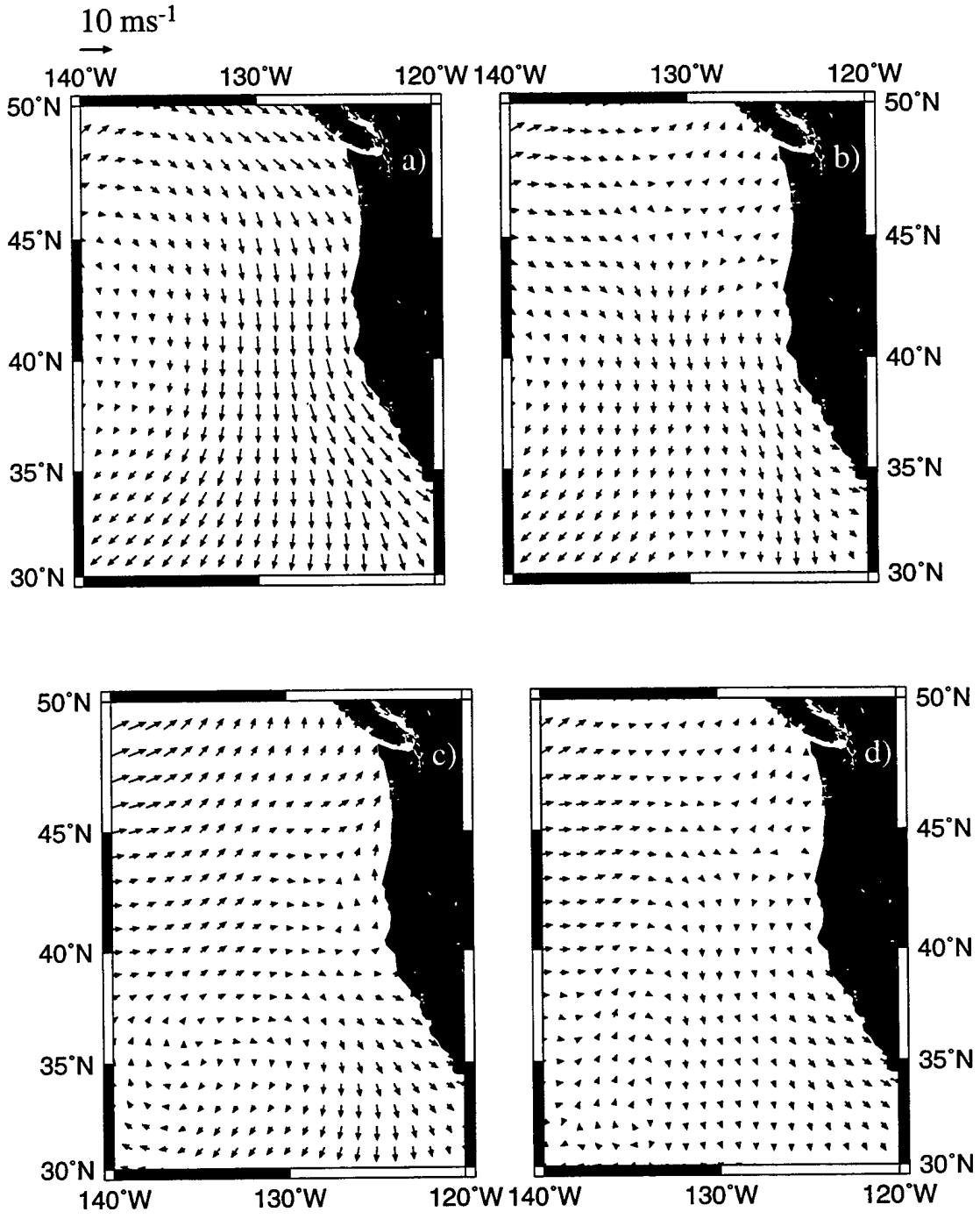

Figure 66: Wind vectors for a) August 12–September 8, 1992; b) September 9–October 6, 1992; c) October 7–November 3, 1992 and d) November 4–December 1, 1992.

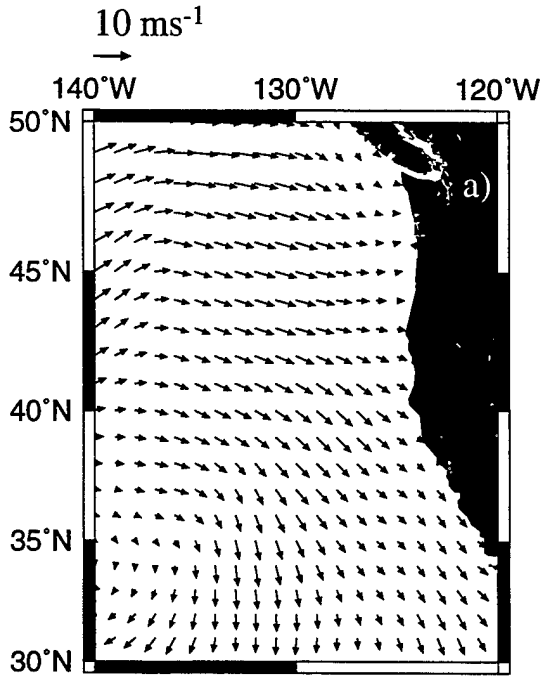

Figure 67: Wind vectors for a) December 2–December 29, 1992.

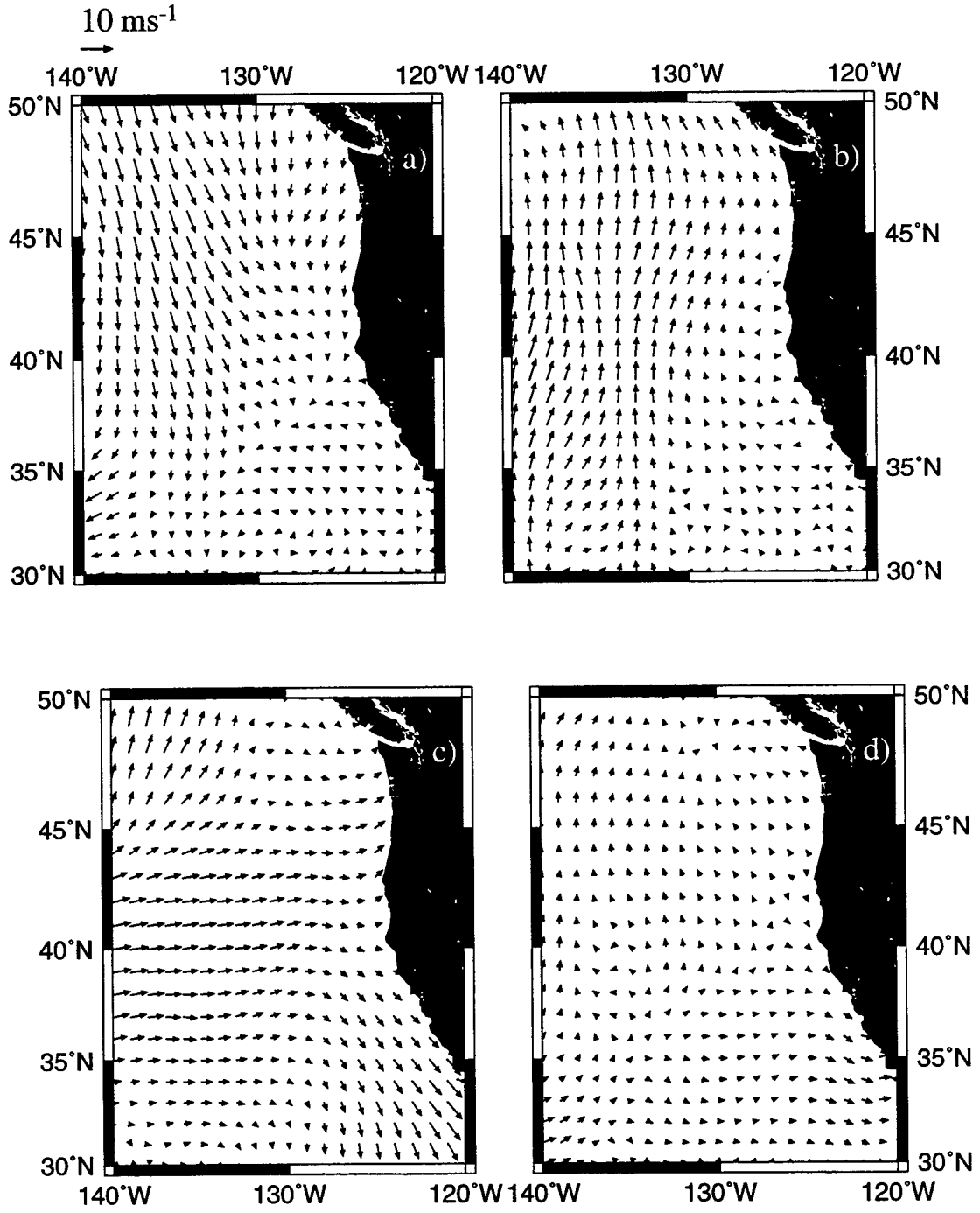

Figure 68: Wind vectors for a) December 30, 1992–January 26, 1993; b) January 27–February 23, 1993; c) February 24–March 23, 1993 and d) March 24–April 20, 1993.

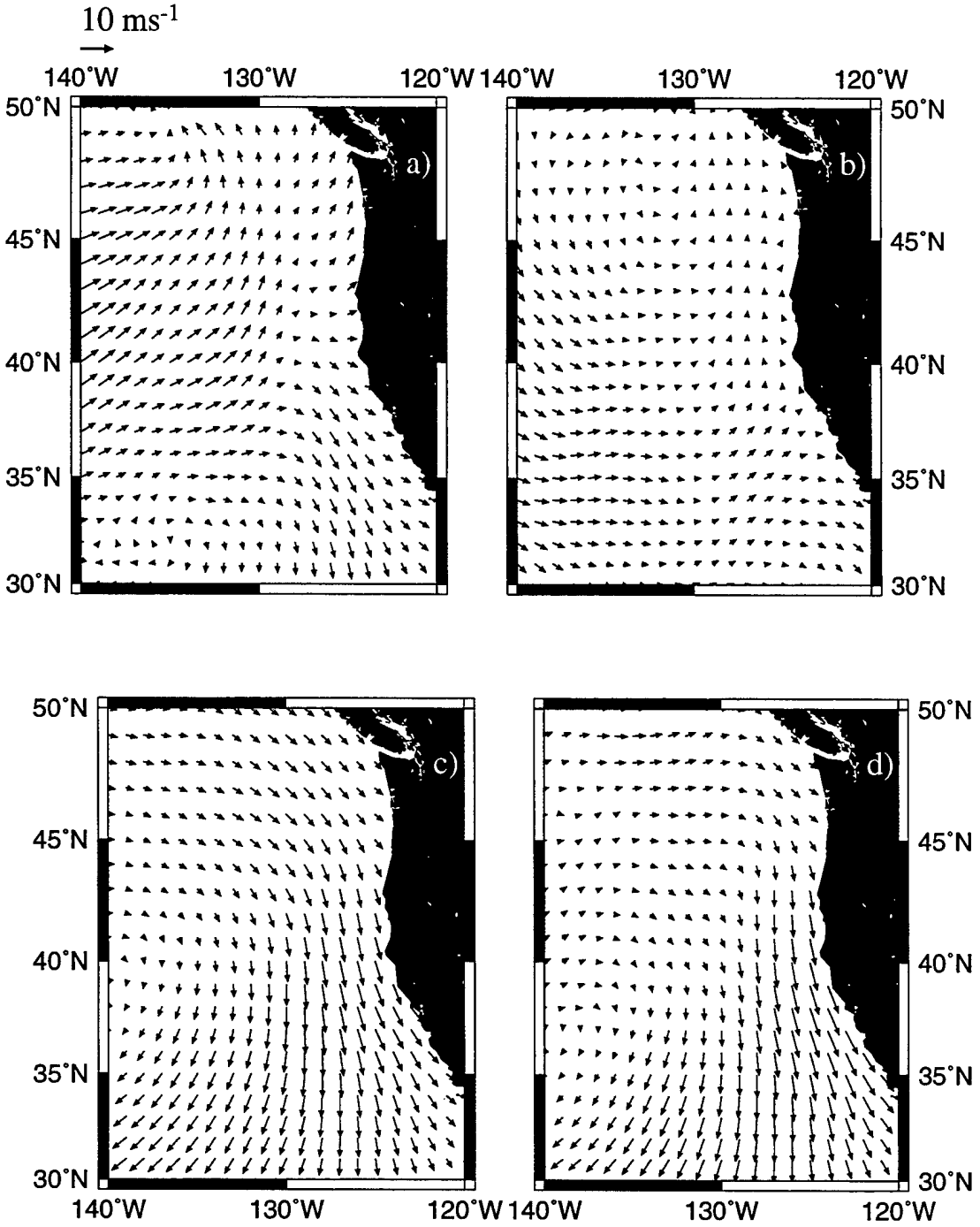

Figure 69: Wind vectors for a) April 21–May 18, 1993; b) May 19–June 15, 1993; c) June 16–July 13, 1993 and d) July 14–August 10, 1993.

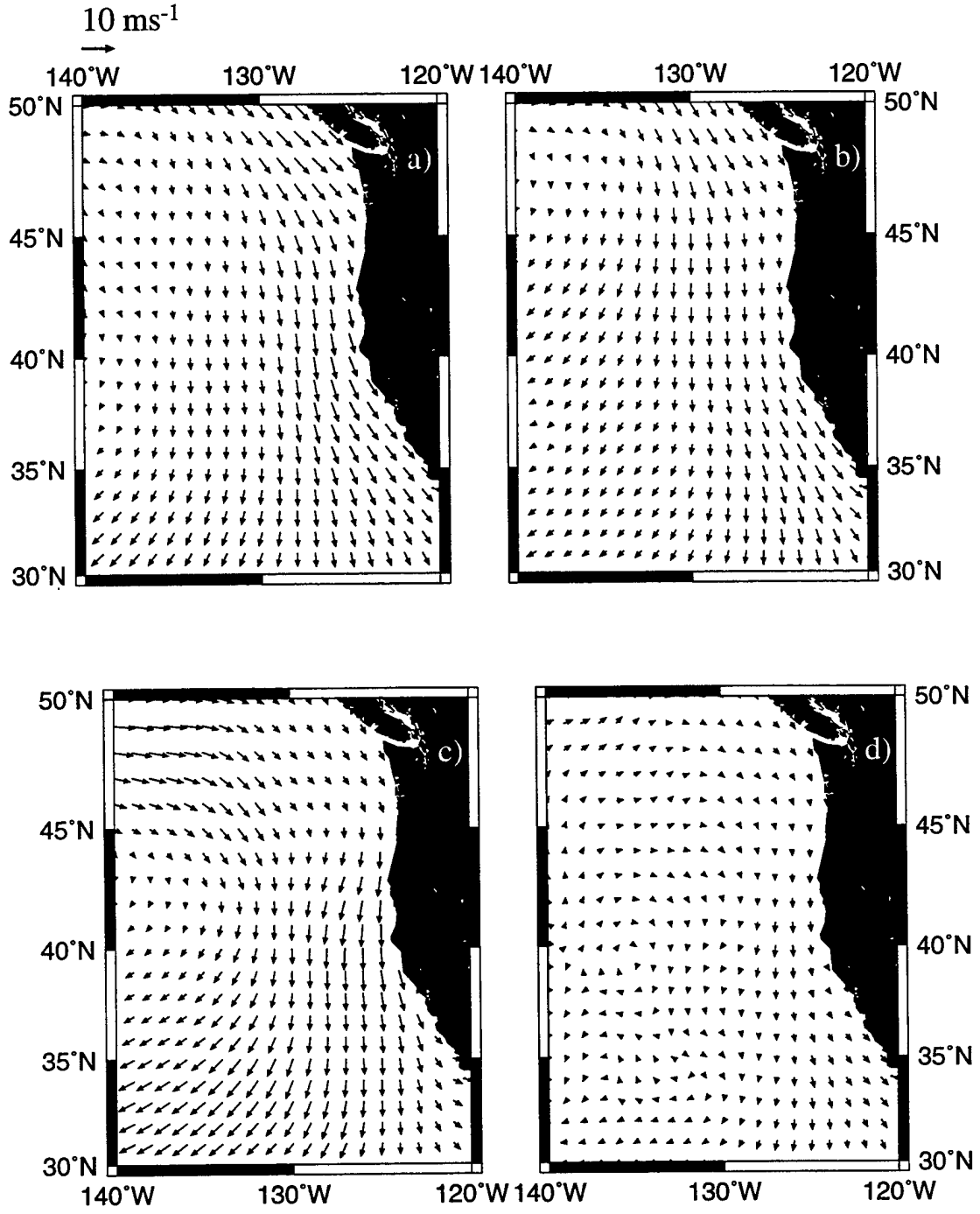

Figure 70: Wind vectors for a) August 11–September 7, 1993; b) September 8–October 5, 1993; c) October 6–November 2, 1993 and d) November 3–November 30, 1993.

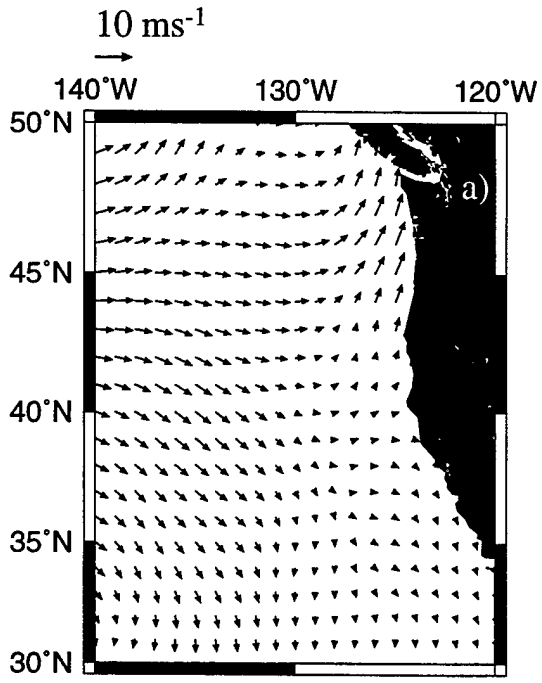

Figure 71: Wind vectors for a) December 2–December 28, 1993.

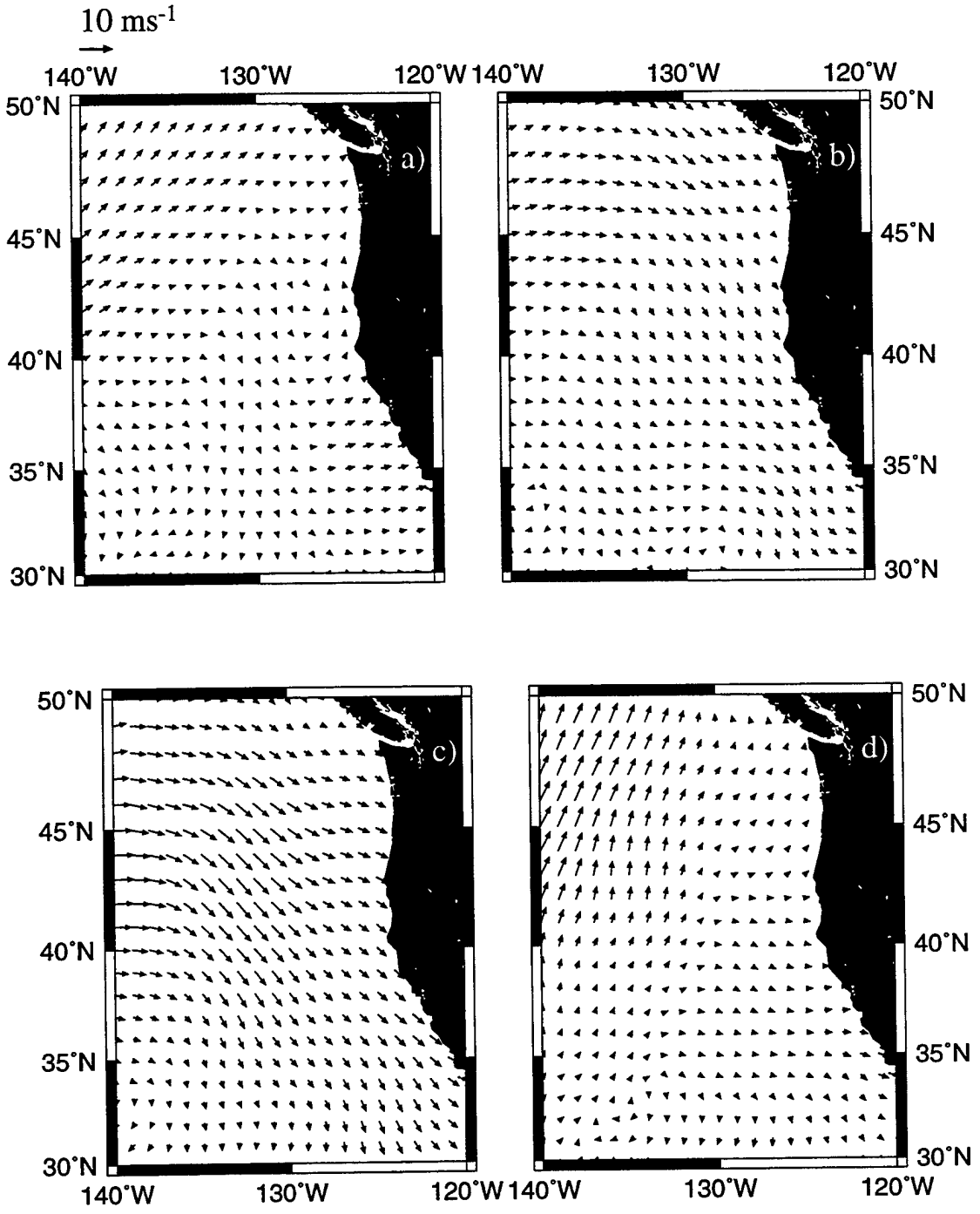

Figure 72: Wind vectors for a) December 29, 1993–January 25, 1994; b) January 26–February 22, 1994; c) February 23–March 22, 1994 and d) March 23–April 19, 1994.

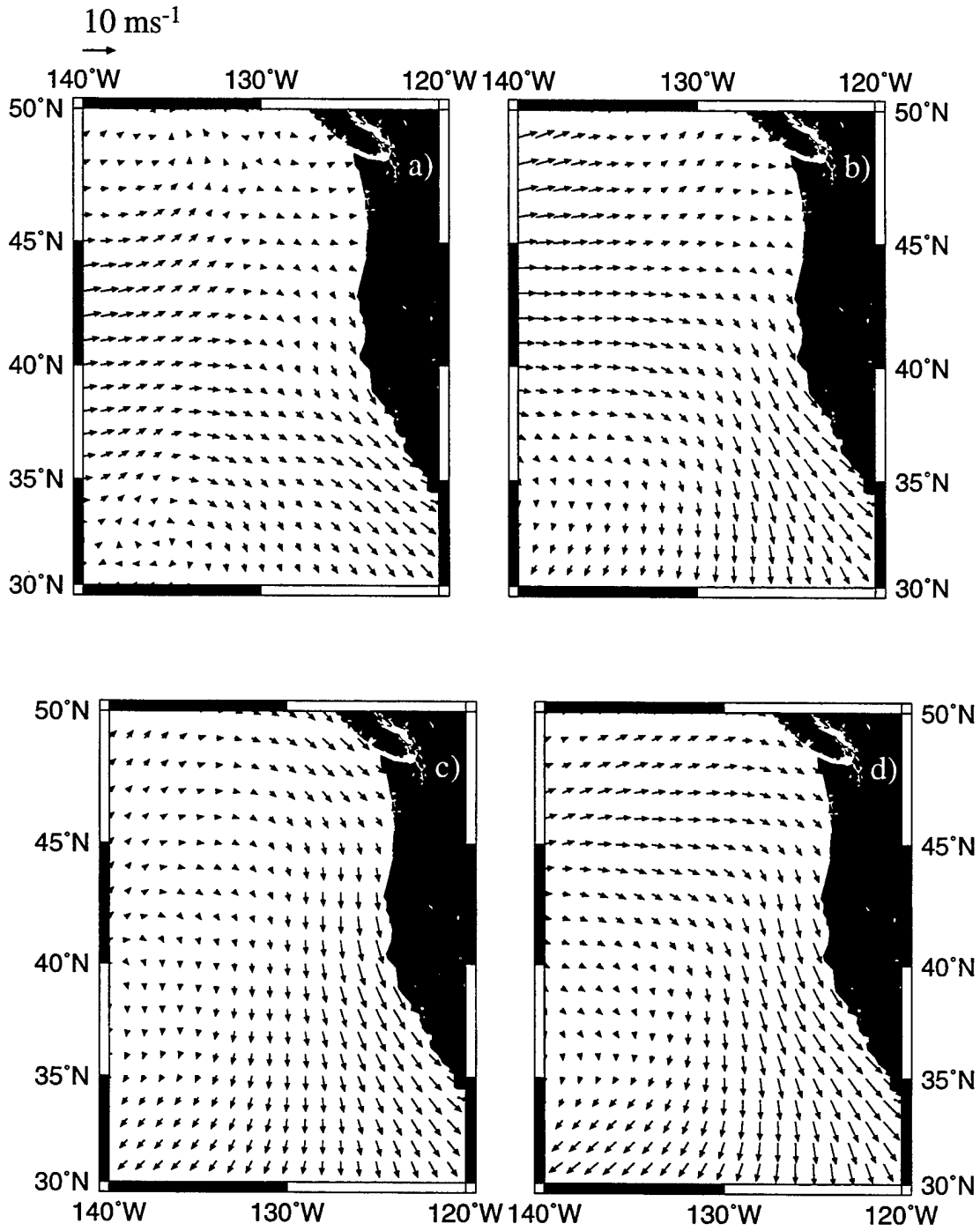

Figure 73: Wind vectors for a) April 20–May 17, 1994; b) May 18–June 14, 1994; c) June 15–July 12, 1994 and d) July 13–August 9, 1994.

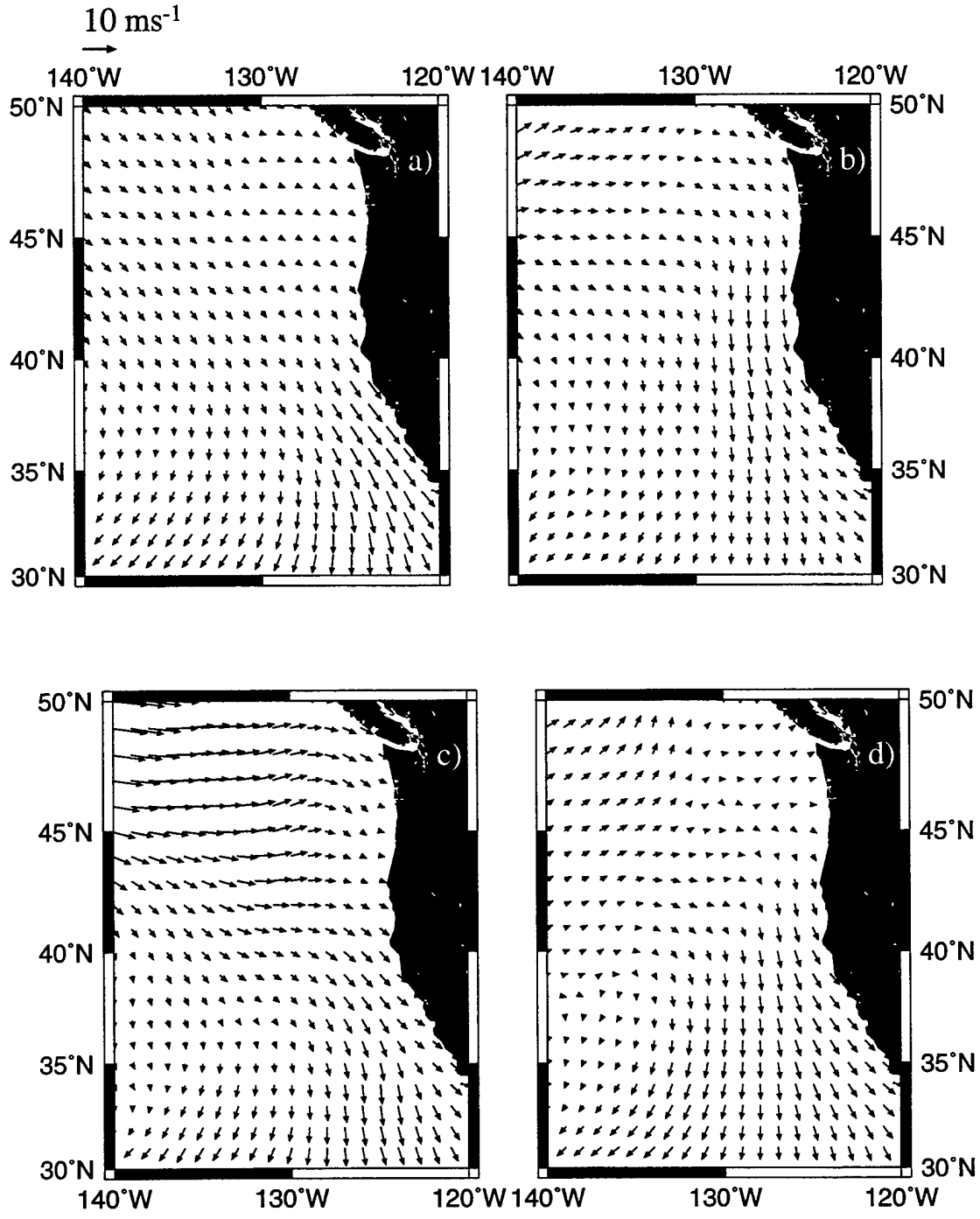

Figure 74: Wind vectors for a) August 10–September 6, 1994; b) September 7–October 4, 1994; c) October 5–November 1, 1994 and d) November 2–November 29, 1994.

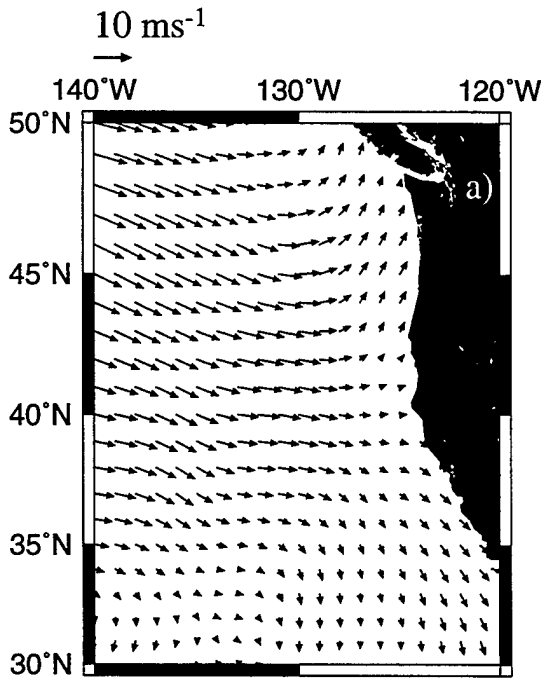

Figure 75: Wind vectors for a) November 30–December 27, 1994.

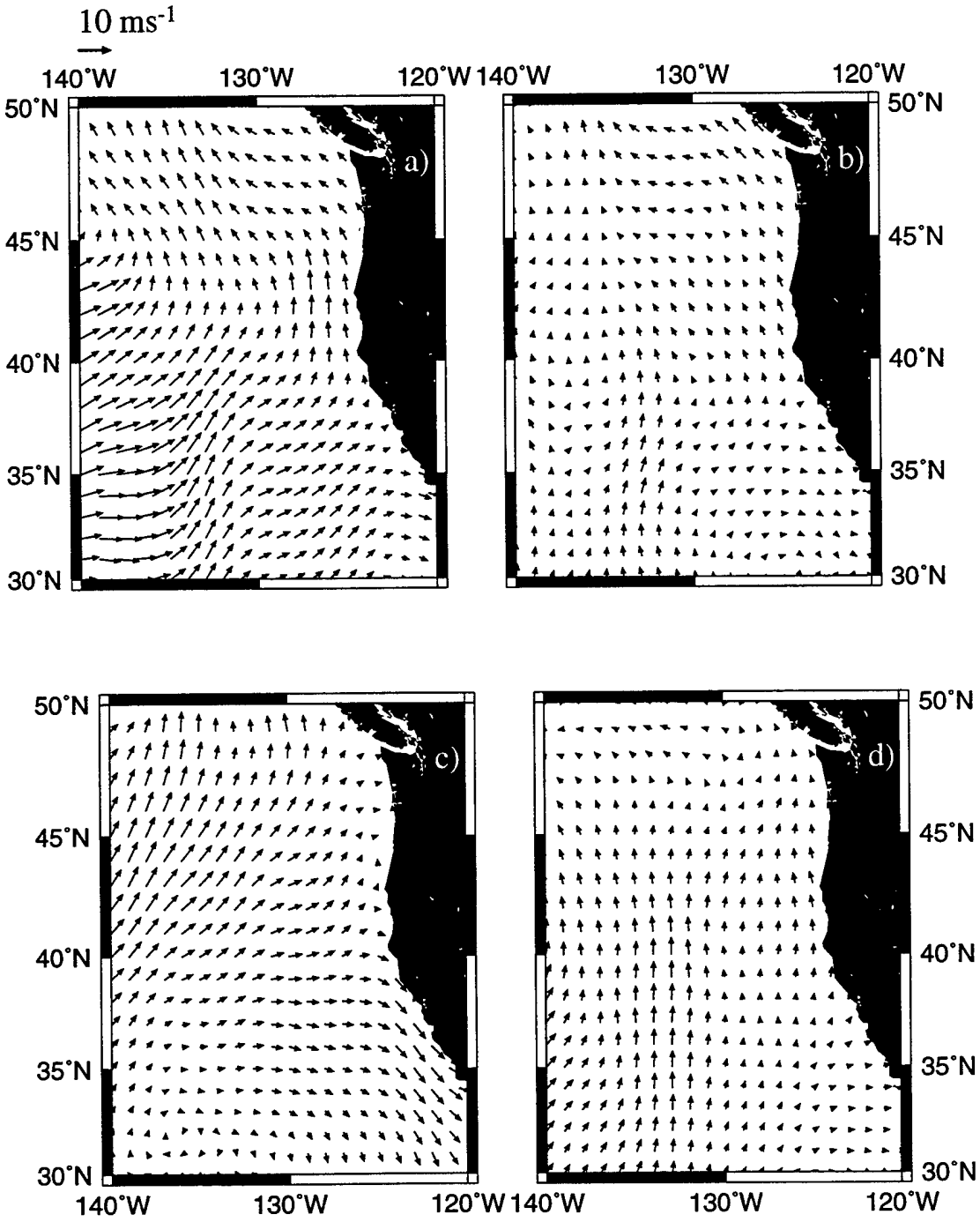

Figure 76: Wind vectors for a) December 28, 1994–January 24, 1995; b) January 25–February 21, 1995; c) February 22–March 21, 1995 and d) March 22–April 18, 1995.

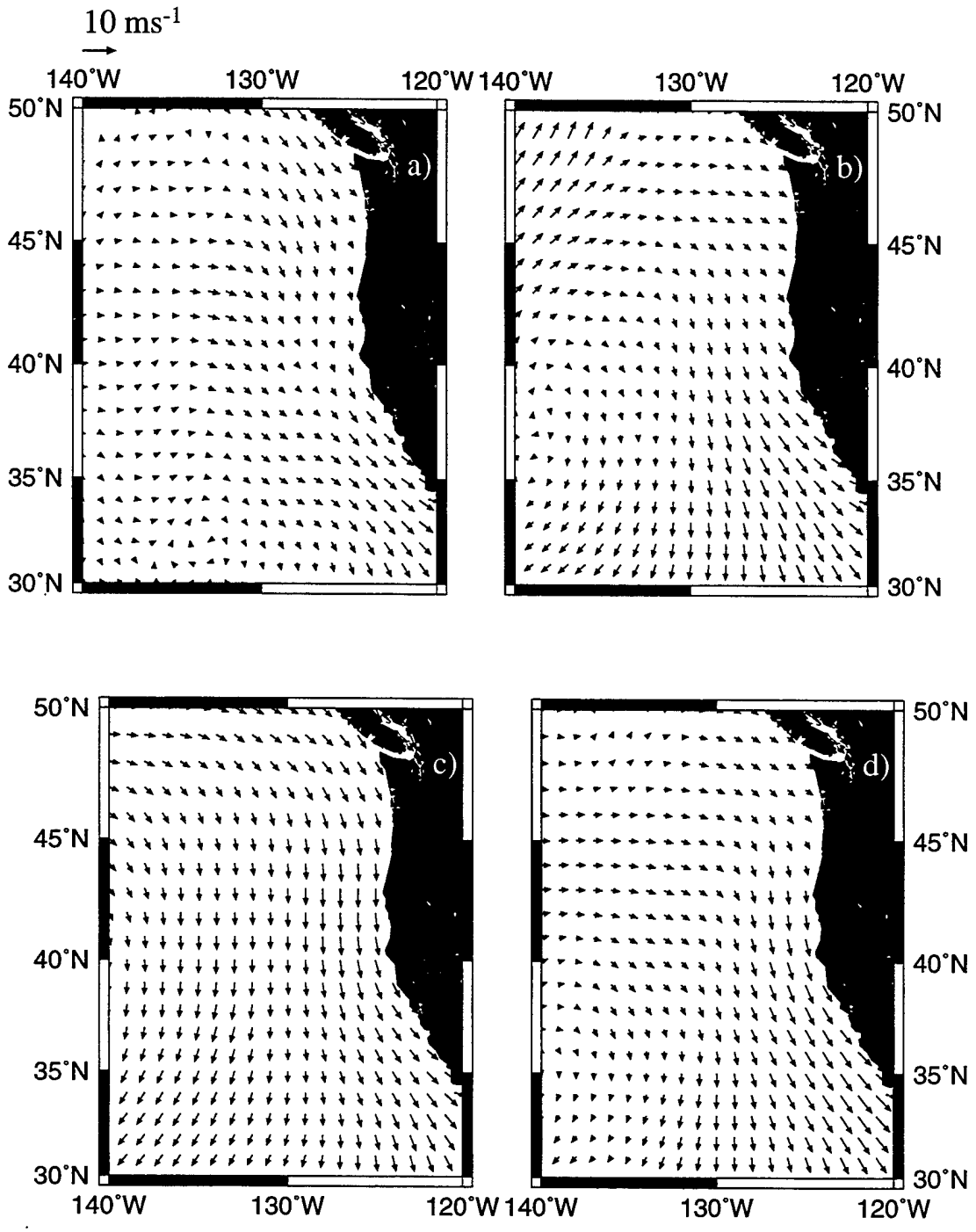

Figure 77: Wind vectors for a) April 19–May 16, 1995; b) May 17–June 13, 1995; c) June 14–July 11, 1995 and d) July 12–August 10, 1995.

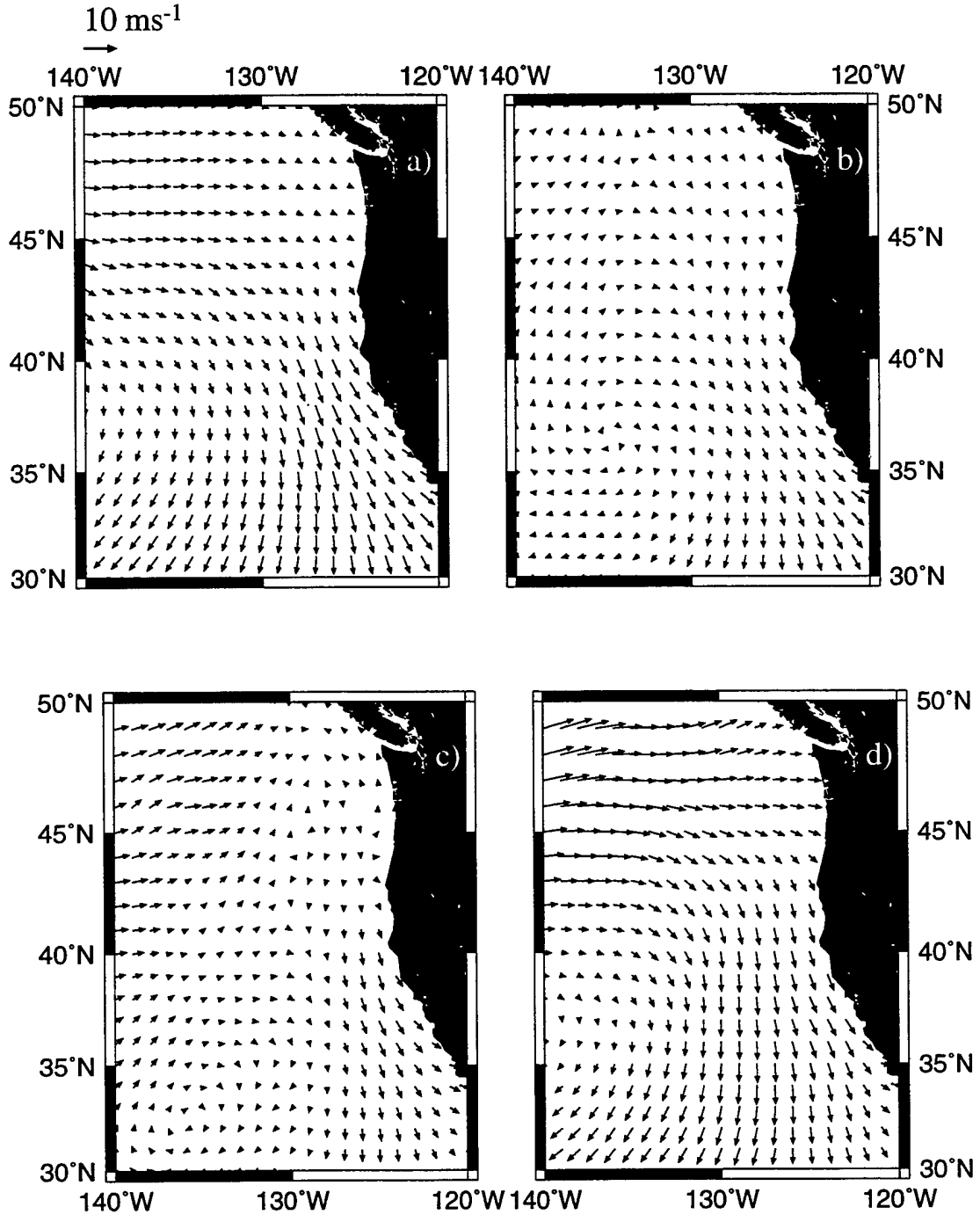

Figure 78: Wind vectors for a) August 11–September 7, 1995; b) September 8–October 5, 1995; c) October 6–November 2, 1995 and d) November 3–November 30, 1995.

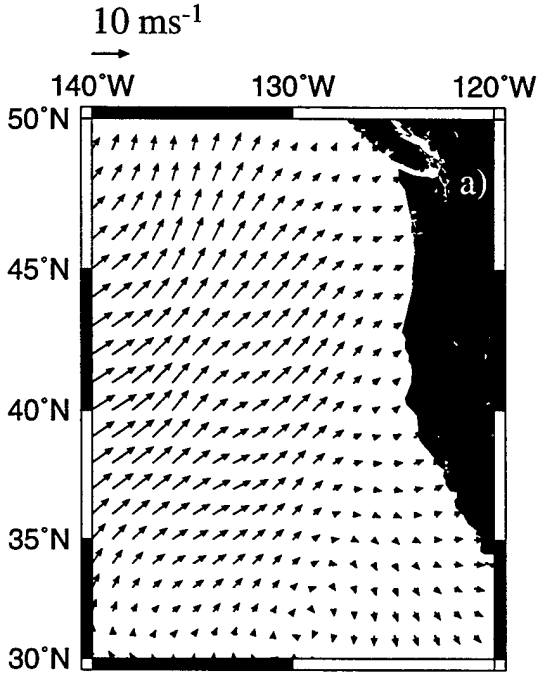

Figure 79: Wind vectors for a) December 1–Dec 28, 1995.

DOCUMENT LIBRARY

Distribution List for Technical Report Exchange – September 1997

University of California, San Diego
SIO Library 0175C
9500 Gilman Drive
La Jolla, CA 92093-0175

Hancock Library of Biology & Oceanography
Alan Hancock Laboratory
University of Southern California
University Park
Los Angeles, CA 90089-0371

Gifts & Exchanges
Library
Bedford Institute of Oceanography
P.O. Box 1006
Dartmouth, NS, B2Y 4A2, CANADA

NOAA/EDIS Miami Library Center
4301 Rickenbacker Causeway
Miami, FL 33149

Research Library
U.S. Army Corps of Engineers
Waterways Experiment Station
3909 Halls Ferry Road
Vicksburg, MS 39180-6199

Institute of Geophysics
University of Hawaii
Library Room 252
2525 Correa Road
Honolulu, HI 96822

Marine Resources Information Center
Building E38-320
MIT
Cambridge, MA 02139

Library
Lamont-Doherty Geological Observatory
Columbia University
Palisades, NY z10964

Library
Serials Department
Oregon State University
Corvallis, OR 97331

Pell Marine Science Library
University of Rhode Island
Narragansett Bay Campus
Narragansett, RI 02882

Working Collection
Texas A&M University
Dept. of Oceanography
College Station, TX 77843

Fisheries-Oceanography Library
151 Oceanography Teaching Bldg.
University of Washington
Seattle, WA 98195

Library
R.S.M.A.S.
University of Miami
4600 Rickenbacker Causeway
Miami, FL 33149

Maury Oceanographic Library
Naval Oceanographic Office
Building 1003 South
1002 Balch Blvd.
Stennis Space Center, MS, 39522-5001

Library
Institute of Ocean Sciences
P.O. Box 6000
Sidney, B.C. V8L 4B2
CANADA

National Oceanographic Library
Southampton Oceanography Centre
European Way
Southampton SO14 3ZH
UK

The Librarian
CSIRO Marine Laboratories
G.P.O. Box 1538
Hobart, Tasmania
AUSTRALIA 7001

Library
Proudman Oceanographic Laboratory
Bidston Observatory
Birkenhead
Merseyside L43 7 RA
UNITED KINGDOM

IFREMER
Centre de Brest
Service Documentation - Publications
BP 70 29280 PLOUZANE
FRANCE

50272-101

REPORT DOCUMENTATION PAGE	1. REPORT NO. WHOI-97-17	2.	3. Recipient's Accession No.

4. Title and Subtitle
Biweekly maps of wind stress for the North Pacific from the ERS-1 scatterometer, 1992 – 1995

5. Report Date
November 1997

6.

7. Author(s) Michael J. Caruso and Kathryn A. Kelly

8. Performing Organization Rept. No.
WHOI-97-17

9. Performing Organization Name and Address

Woods Hole Oceanographic Institution
Woods Hole, Massachusetts 02543

10. Project/Task/Work Unit No.

11. Contract(C) or Grant(G) No.
(C) N00014-92-J-1486
(G) N00014-92-J-1656
957652

12. Sponsoring Organization Name and Address

Office of Naval Research and the National Aeronautics and Space Administration

13. Type of Report & Period Covered
Technical Report

14.

15. Supplementary Notes
This report should be cited as: Woods Hole Oceanog. Inst. Tech. Rept., WHOI-97-17.

16. Abstract (Limit: 200 words)

The ERS–1 scatterometer is the first operational satellite scatterometer in more than a decade. This report describes a technique developed at the Woods Hole Oceanographic Institution to process and analyze the data.

Four years of data (January 1992–December 1995) was analyzed in the North Pacific ocean. Gridded 0.5° x 0.5° wind, wind stress and wind stress curl fields were generated for the North Pacific Ocean on times scale of one week to one month. This data set was compared with in-situ measurements from buoys and coastal weather stations and numerical models. The results show good agreement with models and in-situ measurements. Biweekly maps were chosen after examining error/temporal resolution tradeoff curve.

17. Document Analysis a. Descriptors
ERS-1 Scatterometer
Wind Maps
North Pacific

b. Identifiers/Open-Ended Terms

c. COSATI Field/Group

18. Availability Statement
Approved for public release; distribution unlimited.

19. Security Class (This Report)
UNCLASSIFIED

20. Security Class (This Page)

21. No. of Pages
104

22. Price